UNIVERSITY OF CALIFORNIA, SAN DIEGO

Climate Modulations of Air-Sea Oxygen, Carbon, and Heat Exchange

A dissertation submitted in partial satisfaction of the requirements for the degree
Doctor of Philosophy

in

Oceanography

by

Yassir Art Eddebbar

Committee in charge:

Ralph Keeling, Chair
Sarah Gille
Matthew Long
Jeff Severinghaus
David Victor
Shang-Ping Xie

2018

SIGNATURE PAGE

The Dissertation of Yassir Art Eddebbar is approved, and it is acceptable in quality and form for publication on microfilm and electronically:

Chair

University of California, San Diego

2018

The earth is full of wonders. We may not be able to imagine these until we see them, but by careful observation and clear-headed reasoning, it should be possible for us to understand them.

Roger Revelle

TABLE OF CONTENTS

LIST OF FIGURES

LIST OF TABLES

ACKNOWLEDGEMENTS

Scripps is a magical place and I am grateful for the opportunity to study oceanography at such a fine institution. Listed below is only a fraction of those who made this training a remarkable experience, filled with academic and personal growth.

First on that list is my thesis advisor, Ralph Keeling. Ralph's commitment to precise atmospheric measurements is rivaled only by his dedication to his students and family. His office door was always wide open to discuss any scientific question that came to mind. Throughout the years, Ralph provided me with the ideal balance between the academic independence I cherished and the thoughtful guidance I needed. I am most grateful to Ralph for teaching me the value of persistence, clarity, and simplicity when pursuing or presenting scientific work, and for highlighting the fundamental importance of observations for understanding the climate system.

My thesis work gained significant focus following a workshop in 2013 on climate-carbon cycle feedbacks, co-organized by Matt Long at the National Center for Atmospheric Research (NCAR). At this workshop, Matt introduced me to the boundless possibilities of using Earth system models to gain a deeper understanding of natural phenomena, and I have been hooked ever since. Matt's effective mentorship and unwavering support by hosting me at NCAR, facilitating the use of the NCAR model, and sharing his extensive knowledge of ocean biogeochemical dynamics, made this thesis work possible and inspire me to pursue science as a career.

I would also like to express deep gratitude to my thesis committee, Sarah Gille, Jeff Severinghaus, David Victor, and Shang-Ping Xie for many years of sage advice,

unique insights, and fruitful discussions. Aneesh Subramanian has been such a kind and dedicated mentor, regularly sharing his expertise on successful “grad schooling” and climate dynamics. My PhD training also benefited immensely from productive collaborations with Laure Resplandy and Keith Rodgers at Princeton.

Much of my thesis work was conducted under fellowship support from the National Science Foundation, and was made possible thanks to computational training and resources provided by NCAR. I am thankful for the hard work of staff at the “Keeling lab”, including Sara Ashfar, Bill Paplawski, Adam Cox, and many others, who over the years, have maintained the time series analyzed in this thesis. I am also grateful to student members of the lab, Mariela Brooks and Julia Dohner, for years of support and encouragement.

The Center for Marine Biodiversity and Conservation (CMBC) served as my second academic home. I sincerely thank Lisa Levin and Dick Norris for their leadership and guidance as I explored my interdisciplinary interests through numerous experiences, both across the globe and right here at UC San Diego. Many thanks to Penny Dockry, who facilitated these experiences. My CMBC experience was made especially memorable through interactions with Natasha Gallo and Lauren Linsmayer, with whom lively science discussions, networking with policymakers at UN climate meetings, getting lost in the mountains, and countless dinners with Farnaz, Cody, and Tara will remain as some of the highlights of my time at Scripps. I have also benefited immensely from the camaraderie of the Scripps graduate community, including Bryce Inman, Irina Köster, Eric Oreinstein, Andy Mullen, Travis Courtney, Jen McWhorter,

Ryan Scott, Chris and Anna McCall, and Sara Sanchez. Together, we discovered the healing powers of burritos after a long day of doing research.

Finally, I am grateful to my family for their unconditional love and support prior to and throughout my graduate experience. Mike and Jo Ellen Brunner, thank you for giving me the idea to pursue a PhD degree in the first place, and for inspiring me to be a student for life. The biggest thanks go to my wife, Jessie Brunner, for being there during the worst and the best. I am so grateful for your love and support over these challenging, albeit rewarding years. And finally, my most sincere and heartfelt thanks to my parents, Aicha Kasbaoui and Bouchaib Eddebbar, for letting me go to California as a 19-year old with nothing but a dream in mind. What a ride!

Chapter 2, in full, is a reprint of the material as it appears in Global Biogeochemical Cycles, 2017: Eddebbar, Y. A., M. C. Long, L. Resplandy, C. Rödenbeck, K. B. Rodgers, M. Manizza, and Keeling R.F. The dissertation author was the primary investigator and author of this paper.

Chapter 3, in part, is currently being prepared for submission for publication of the material. Eddebbar, Y. A., Rodgers, K., Long, M.C., Subramanian, A., Xie, S-P., Keeling R.F. The dissertation author was the primary investigator and author of this material.

Chapter 4, in part, is currently being prepared for submission for publication of the material. Eddebbar, Y. A., Keeling R.F., Resplandy, L., Xie, S-P., Rodgers, K., Long, M.C. The dissertation author was the primary investigator and author of this material.

VITA

2008	Bachelor of Science, California State University, Long Beach
2008 – 2011	Environmental Scientist, United Research Services, Santa Ana, CA
2011 – 2013	National Science Foundation Interdisciplinary Graduate Education and Research Training Fellow
2012	Master of Science, Scripps Institution of Oceanography, University of California, San Diego
2013 – 2017	National Science Foundation Graduate Research Fellow
2018	Doctor of Philosophy, Scripps Institution of Oceanography, University of California, San Diego

PUBLICATIONS

Eddebbar, Y. A., M. C. Long, L. Resplandy, C. Rödenbeck, K. B. Rodgers, M. Manizza, and Keeling R. F., 2017. Impacts of ENSO on air-sea oxygen exchange: Observations and mechanisms. *Global Biogeochemical Cycles*, 31, doi:10.1002/2017GB005630.

Delorme, B. and Eddebbar, Y. A., 2016. Ocean Circulation and Climate: An Overview. *Ocean and Climate, Scientific Notes, 2nd Edition*: 12-19.

Eddebbar, Y. A., Gallo, N. D., and Linsmayer, L. B., 2015. The Oceans and the UN Framework Convention on Climate Change. *Limnology and Oceanography Bulletin*, 24: 69–72. DOI:10.1002/lob.10059.

ABSTRACT OF THE DISSERTATION

Climate Modulations of Air-sea Oxygen, Carbon, and Heat Exchange

by

Yassir Art Eddebbar

Doctor of Philosophy in Oceanography

University of California, San Diego 2018

Ralph Keeling, Chair

The exchanges of oxygen (O_2), carbon dioxide (CO_2), and heat across the air-sea interface have broad and profound implications for climate and marine ecosystems. In this thesis, I use observations and models to improve our process understanding of how natural climate variability modulates these exchanges. In chapter 2, I investigate the impacts of El Niño Southern Oscillation (ENSO) on air-sea O_2 exchange. I use atmospheric inversions of global, continuous timeseries of atmospheric O_2 and CO_2

and ocean models to evaluate links between ENSO and air-sea O_2 exchange and explore driving mechanisms using ocean and atmospheric models. I find that El Niño events lead to anomalous outgassing of oceanic O_2, a response that is driven primarily by changes in the source and intensity of upwelling in the equatorial Pacific. In Chapter 3, I examine the impacts of tropical volcanic eruptions on air-sea exchanges of O_2, CO_2 and heat using coupled model simulations and observations. Here, I find that volcanic events lead to substantial oceanic heat loss that is accompanied by large oceanic uptakes of oxygen and carbon. An El Niño-like pattern emerges following tropical eruptions and plays a major role in modulating the oceanic response to volcanic forcing. In Chapter 4, I explore the use of global continuous atmospheric measurements of O_2 and CO_2 to evaluate claims that enhanced ocean heat uptake caused the recent global surface warming hiatus, based on a potential negative relationship between air-sea heat and gas exchange. Here, I find that the relationship between air-sea oxygen, carbon and heat fluxes due to natural variability is complex; air-sea heat and O_2 exchange are positively coupled in the tropical Pacific, but are negatively coupled at higher latitudes. This spatially distinct relationship complicates the attribution of observed decadal trends in atmospheric O_2 and CO_2 to changes in ocean heat uptake, but may present an opporunitity to develop regional constraints. Collectively, the results of this thesis contribute to a quantitative and mechanistic framework enabling interpretation of O_2 and CO_2 trends in the context of ongoing ocean warming and deoxygenation.

CHAPTER 1: INTRODUCTION

The ocean's biogeochemistry is tightly intertwined with its physics. In this thesis, I explore several aspects of the coupling between climate and ocean biogeochemical dynamics, focusing on how forced (e.g., volcanic eruptions) and unforced climate perturbations (e.g., ENSO) influence the exchanges of O_2, CO_2, and heat across the air-sea interface. Understanding the underlying mechanisms of how climate modulates the cycling of oxygen and carbon is critical to the attribution of anthropogenic climate change in the oceans (Gruber, 2011) and the prediction of geoengineering effects on marine ecosystems. In turn, changes in biogeochemical ocean properties present unique insights for ocean physical processes such as changes in ocean circulation (e.g., upwelling and ventilation) and its heat content.

A major consequence of the coupling between climate and ocean biogeochemistry is the oceanic loss of dissolved oxygen ($[O_2]$) due to anthropogenic warming. This phenomenon, known as ocean "deoxygenation" (Keeling et al., 2010), is driven by the temperature-sensitivity of O_2 solubility and the stratification effects of warming on ventilation rates (Sarmiento et al., 1998; Keeling and Garcia, 2002). This long-term oceanic $[O_2]$ decline, however, is superimposed on substantial interannual-to-decadal variability associated with natural climate variability, challenging the detection and attribution of anthropogenic trends in recent observations (Long et al., 2016).

The oceanic carbon cycle is also sensitive to climate pertubations on a variety of timescales. Past studies argued that the oceanic sink of anthropogenic carbon is weakening due to ocean warming (Le Quéré et al., 2007). A more recent synthesis of ocean observations, however, suggest a decadal strengthening of the oceanic carbon sink in recent decades (Landshützer et al., 2015). Natural variability of the climate system on interannual to decadal timescales may play a major role in modulating the intensity of the oceanic carbon sink. The attribution of past and present changes in the oceanic carbon sink thus require improved understanding of the coupling between climate variability and air-sea carbon exchange.

Specifically, natural modes of internal variability (e.g., ENSO) and externally forced climate perturbations (e.g., volcanic eruptions) have been shown to have major impacts on ocean biogeochemical cycles (Feely et al., 2002; McKinley et al., 2004; Frölicher et al., 2009; Deutsch et al., 2011). The magnitude and mechanisms of their influence on $[O_2]$ variability and air-sea exchange of O_2 and CO_2, however, remain poorly understood due to substantial gaps in global ocean observations.

Chapters 2 and 3 of this thesis explore the coupling between climate and the oceanic oxygen and carbon cycles due to ENSO and volcanic eruptions, respectively, from an atmospheric perspective. Due to the scarcity of global ocean observations that can resolve the complex spatial and temporal trends associated with natural modes of variabilty and volcanic eruptions, I rely here instead on longterm global measurements of atmospheric O_2 and CO_2, maintained at various stations within the Scripps Atmospheric O_2 Network (Keeling and Manning, 2014). Due to their tight coupling in

terrestrial processes, atmospheric O_2 and CO_2 can be used jointly to infer changes in ocean fluxes using a tracer known as Atmospheric Potential Oxyen (APO). This tracer is calculated as $APO \simeq O_2 + 1.1 * CO_2$ (Stephens et al., 1998), where the sum of O_2 and CO_2 through the 1.1 terrestrial oxidative ratio makes APO insensitive to biospheric influence (Severinghaus, 1995). Due to buffering of CO_2 fluxes by carbonate chemistry, APO is expected to be dominated by O_2 variability on short timescales (Keeling and Severinghaus, 2000), making it a potentially ideal tracer for the oceanic response to climate variability on the timescales associated with ENSO and volcanic eruptions.

To outline mechanisms driving the ENSO and volcanic modulations of air-sea O_2 and CO_2 exchange and interior distributions, I rely on models of atmospheric and ocean circulation and biogeochemistry. I primarily focus on the Community Earth System Model (CESM), which couples atmospheric and ocean general circulation models and includes a representation of ocean biogeochemistry. Specifically, I make use of "hindcast" and "control" simulations of CESM and other models to evaluate the ocean biogeochemical response to known modes of variability such as ENSO. To isolate the ocean biogoechemical response to external forcing such as volcanic cooling, I analyze Large Ensemble (LE) integrations conducted with CESM (Deser et al., 2012; Kay et al., 2014) and the Geophysical Fluid Dynamics Laboratory (GFDL) model (Rodgers et al., 2015). The combined use of observations and models throughout this thesis not only helps improve our process understanding of observed phenomena, but

also presents, in turn, a unique opportunity to test model representations of the coupling between climate and ocean biogeochemistry.

As new policy developments continue to impede global efforts to curb greenhouse gas emissions, interest in geoengineering has been recently reignited as a possible viable "solution" to climate change. Most discussions of geoengineering impacts, however, have focused on risks related to atmospheric chemistry and the hydrological cycle, with little to no attention given to ocean impacts. The impacts of volcanic radiative perturbations, the closest analogs to radiative management (RM) proposals, on ocean physical and biogeochemical dynamics presented in Chapter 3, provide valuable insights on potential unintended consequences of geoengineering for marine ecosystems.

The sensitivity of oxygen and carbon fluxes to ocean temperature and circulation might also allow APO to be used as an integrated tracer of physical ocean processes. Ocean warming is expected to lead to a net flux of oceanic O_2 to the atmosphere, due to warming effects on gas solubility and ventilation. Informed by this negative relationship between ocean heat uptake and O_2 outgassing, and by the tightly negative coupling of O_2 and CO_2 in ocean biological processes (i.e. photosynthesis and respiration), I explore the use of APO on interannual to decadal timescales as a tracer for ocean heat uptake in Chapter 4. This is motivated by recent claims that enhanced ocean heat uptake may have led to the hiatus in global mean surface warming (Meehl et al., 2011; 2013). Evaluating the role of ocean heat uptake in observed global mean surface temperature trends is critical to predicting future

trajectories of global warming, and is especially relevant given the reliance of climate agreements on surface warming targets (e.g., Paris Accord's 2ºC target).

References

Cabré, A., I. Marinov, R. Bernardello. and D. Bianchi (2015), Oxygen minimum zones in the tropical Pacific across CMIP5 models: mean state differences and climate change trends, Biogeosciences, 12, 5429–5454, doi:10.5194/bg-12-5429-2015.

Deser, C., A. Phillips, V. Bourdette, and H. Teng, (2012), Uncertainty in climate change projections: the role of internal variability. Clim. Dyn., 38, 527–546, doi:10.1007/s00382-010-0977-x.

Deutsch, C., H. Brix, T. Ito, H. Frenzel, and L. Thompson (2011), Climate-forced variability of ocean hypoxia, Science, 333, 336–339, doi:10.1126/science.1202422.

Frölicher T. L., F. Joos, G. K. Plattner, M. Steinacher, S. C. Doney (2009), Natural variability and anthropogenic trends in oceanic oxygen in a coupled carbon cycle-climate model ensemble, Glob. Biogeochem. Cycles, 23, GB1003, doi:10.1029/2008GB003316

Gruber, N. (2011), Warming up, turning sour, losing breath: Ocean biogeochemistry under global change, Philos. Trans. R. Soc. A, 369(1943), 1980 – 1996

Kay, J. E., C. Deser, A. Phillips, A. Mai, C. Hannay, G. Strand, J. M. Arblaster, S. C. Bates, G. Danabasoglu, J. Edwards, and M. Holland (2014), The Community Earth System Model (CESM) Large Ensemble Project: A Community Resource for Studying Climate Change in the Presence of Internal Climate Variability. Bull. Amer. Meteor. Soc., doi:10.1175/BAMS-D-13-00255.1.

Keeling, R. F. and H. Garcia (2002), The change in oceanic O_2 inventory associated with recent global warming, Proc. Natl. Acad. Sci. USA, 99, 7848–7853, doi:10.1073/pnas.122154899.

Keeling, R. F. and J. P. Severinghaus (2000), Atmospheric oxygen and the carbon cycle, The Carbon Cycle, Edited by T. M. L. Wigley, and D. S. Schimel, pp. 134–140, Cambridge Univ. Press, Boston, Mass, USA.

Keeling, R., and A. Manning (2014), Studies of Recent Changes in Atmospheric O2 Content, Treatise on Geochemistry, 2nd ed., H. D. Holland and K. K. Turekian, Ed., Elsevier, 385–404, doi:10.1016/B978-0-08-095975-7.00420-4.

Landschützer, P., N. Gruber, F.A. Haumann, C. Rödenbeck, D.C. Bakker, S. Van Heuven, M. Hoppema, N. Metzl, C. Sweeney, T. Takahashi, and B. Tilbrook (2015), The reinvigoration of the southern ocean carbon sink. Science, 349 (6253), 1221–1224.

Le Quéré, C., C. Rödenbeck, E. T. Buitenhuis, T. J. Conway, R. Langenfelds, A. Gomez, C. Labuschagne, M. Ramonet, T. Nakazawa, N. Metzl, N. Gillett and M. Heimann (2007), Saturation of the Southern Ocean CO2 sink due to recent climate change. Science, 316, 1735–1738, doi:10.1126/science.1136188

Long, M. C., C. A. Deutsch, and T. Ito (2016), Finding forced trends in oceanic oxygen, Global Biogeochem. Cycles, 30, 10.1002/2015GB005310.

McKinley, G. A., M. J. Follows, and J. Marshall (2004), Mechanisms of air-sea CO2 flux variability in the equatorial Pacific and the North Atlantic, Global Biogeochem. Cycles, 18, GB2011, doi:10.1029/ 2003GB002179.

McKinley, G. A., M. J. Follows, J. Marshall, and S. M. Fan (2003), Interannual variability of air-sea O_2 fluxes and the determination of CO2 sinks using atmospheric O_2/N_2, Geophys. Res. Lett., 30(3), 1101, doi:10.1029/ 2002GL016044.

Meehl, G. A., A. Hu, J. M. Arblaster, J. Fasullo, and K. E. Trenberth (2013), Externally forced and internally generated decadal climate variability associated with the interdecadal pacific oscillation. Journal of Climate, 26 (18), 7298–7310.

Meehl, G. A., J. M. Arblaster, J. T. Fasullo, A. Hu, and K. E. Trenberth (2011), Model-based evidence of deep-ocean heat uptake during surface temperature hiatus periods, Nat. Clim. Change, 1(7), 360–364, doi:10.1038/nclimate1229.

Rodgers, K., J. Lin, and T. Frölicher, (2015), Emergence of multiple ocean ecosystem drivers in a large ensemble suite with an earth system model. Biogeosciences, 12 (11), 3301.

Sarmiento J.L., T.C. Hughes, R.J. Stouffer, and S. Manabe (1998), Simulated response of the ocean carbon cycle to anthropogenic climate warming, Nature, 393, 245–249, doi:10.1038/30455.

Severinghaus, J. P. (1995), Studies of the Terrestrial O_2 and Carbon Cycles in Sand Dune Gases and in Biosphere 2, Ph.D. thesis, Columbia University, New York, U.S.A.

Stephens, B. B., R. F. Keeling, M. Heimann, K. D. Six, R. Murnane, and K. Caldeira (1998), Testing global ocean carbon cycle models using measurements of atmospheric O_2 and CO_2 concentration. Glob. Biogeochem. Cycles, 12, 213–230, doi:10.1029/97GB03500.

CHAPTER 2: ENSO IMPACTS ON AIR-SEA OXYGEN EXCHANGE: OBSERVATIONS AND MECHANISMS

Abstract

Models and observations of Atmospheric Potential Oxygen ($APO \simeq O_2 + 1.1 * CO_2$) are used to investigate the influence of El Niño Southern Oscillation (ENSO) on air-sea O_2 exchange. An atmospheric transport inversion of APO data from the Scripps flask network shows significant interannual variability in tropical APO fluxes that is positively correlated with the Niño3.4 index, indicating anomalous ocean outgassing of APO during El Niño. Hindcast simulations of the Community Earth System Model (CESM) and the Institut Pierre-Simon Laplace (IPSL) model show similar APO sensitivity to ENSO, differing from the Geophysical Fluid Dynamic Laboratory (GFDL) model, which shows an opposite APO response. In all models, O_2 accounts for most APO flux variations. Detailed analysis in CESM shows the O_2 response is driven primarily by ENSO-modulation of the source and rate of equatorial upwelling, which moderate the intensity of O_2 uptake due to vertical transport of low-O_2 waters. These upwelling changes dominate over counteracting effects of biological productivity and thermally-driven O_2 exchange. During El Niño, shallower and weaker upwelling leads to anomalous O_2 outgassing, whereas deeper and intensified upwelling during La Niña drives enhanced O_2 uptake. This response is strongly localized along the central and eastern equatorial Pacific, leading to an equatorial zonal dipole in atmospheric anomalies of APO. This dipole is further intensified by ENSO-related changes in winds, reconciling apparently conflicting

APO observations in the tropical Pacific. These findings suggest a substantial and complex response of the oceanic O_2 cycle to climate variability that is significantly (>50%) underestimated in magnitude by ocean models.

1. Introduction

Dissolved oxygen (O_2) is essential to life in the ocean. As anthropogenic warming reduces O_2 solubility and weakens the ventilation of the ocean's interior, oceanic O_2 content is expected to decline (Sarmiento et al., 1998; Bopp et al., 2002; Keeling and Garcia, 2002), with potentially serious and widespread implications for marine ecosystems, global fisheries, and biogeochemical cycles of carbon, nutrients, and nitrous oxide (Keeling et al., 2010). Several studies suggest this decline, i.e. "deoxygenation", is already underway (Stramma et al., 2008; Helm et al., 2011; Andrews et al., 2013). Regionally, however, the attribution of O_2 changes remains challenging due to natural climate variability, which drives substantial O_2 variations on interannual to multi-decadal timescales, obscuring the detection of forced trends (Emerson et al., 2004; Frölicher et al., 2009; Deutsch et al., 2011; Rodgers et al., 2015; Long et al., 2016). Interannual variability in physical and biogeochemical processes and their interactions are especially important as their integrated effects can lead to pronounced decadal [O_2] variability (Ito and Deutsch, 2010, 2013). Another challenge is that models show poor skill in simulating [O_2] distributions and change, particularly in the tropical Pacific, where models and observations disagree on both magnitude and sign of subsurface [O_2] change (Stramma et al., 2012; Bopp et al., 2013; Cocco et al., 2013). These discrepancies arise from deficiencies in model representation of the

competing effects of biology, transport, and thermodynamic processes on [O_2] variability (Cabré et al., 2015).

The natural variability of the oceanic oxygen cycle also has important implications for understanding the global carbon cycle. Atmospheric O_2 and CO_2 measurements have long been used to resolve global land and ocean carbon sinks (Keeling et al., 1996). This method is based on key differences in terrestrial versus oceanic O_2 and CO_2 exchanges with the atmosphere: Land uptake of anthropogenic CO_2 is driven by photosynthesis which produces O_2, whereas ocean CO_2 uptake involves carbonate chemistry and no associated O_2 exchange (Keeling et al., 1993). A complication with this method is that air-sea O_2 flux can also vary due to natural variability-related processes that are not directly tied to the uptake of anthropogenic CO_2 (Keeling et al., 1993; Keeling and Garcia, 2002; McKinley et al., 2003; Resplandy et al., 2014). These additional fluxes must thus be accounted for to properly resolve the land and ocean carbon sinks (Manning and Keeling, 2006). The magnitude and processes driving the natural variability of air-sea O_2 exchange, however, remain poorly understood, involving complex interactions between climate and ocean biogeochemical cycles.

In this study, we investigate the influence of El Niño Southern Oscillation (ENSO), the leading mode of interannual climate variability, on the air-sea exchange of O_2. ENSO phenomena provide an ideal framework to i) understand mechanisms driving the upper ocean O_2 cycle response to climate forcing on interannual to decadal timescales, ii) constrain the role of natural variability in observed atmospheric and

oceanic O_2 trends; and iii) test models' representation of coupled climate-biogeochemical dynamics.

Figure 2.1 illustrates the major physical and biogeochemical processes driving air-sea fluxes of O_2 and CO_2 in the tropical Pacific. The prevailing easterlies drive Ekman upwelling of dissolved inorganic carbon (DIC) rich and O_2-depleted waters in the eastern tropical Pacific and along the Equator, causing strong outgassing of CO_2 and uptake of O_2 (Wanninkhof et al., 1995; Takahashi et al., 1997). This upwelling of low-O_2 thermocline waters maintains an extensive equatorial band of O_2-undersaturated waters at the surface that extends through the central equatorial Pacific (Figure 2.2). These upwelled waters are also rich in nutrients, which fertilize the photosynthetic production of O_2 in the euphotic zone, thereby counteracting the O_2 deficit caused by upwelling, driving O_2 outgassing as these waters spread away from the equator (Wanninkhof et al., 1995; Najjar and Keeling, 2000). Concurrently, warming of these cold upwelled waters due to surface heating drives the outgassing of both CO_2 and O_2 due to the dependence of gas solubility on temperature (Keeling et al., 1993). The net balance of these dynamic, biological, and thermal processes in the tropical Pacific results in an intense natural source of both O_2 and CO_2 to the atmosphere (Takahashi et al., 1997; Gruber et al., 2001). This large O_2 outgassing in the tropical Pacific is balanced globally by uptake at higher latitudes, where poleward transport of warm waters and seasonal vertical mixing induce substantial heat loss and ventilation of low-O_2 waters (Najjar and Keeling, 2000).

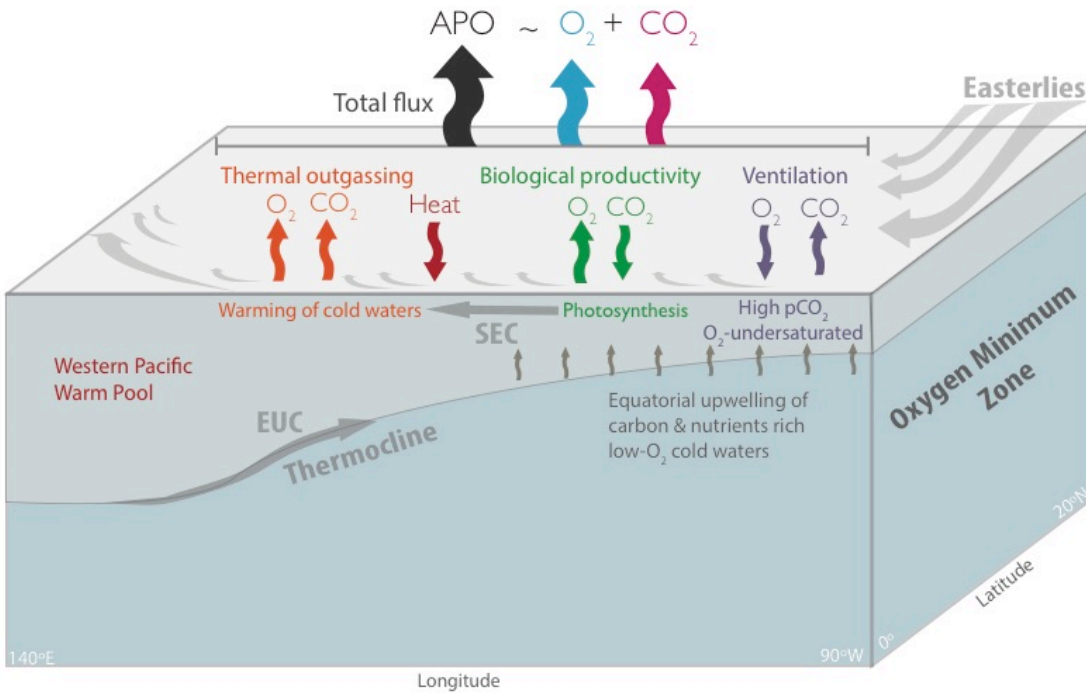

Figure 2.1. Schematic of major physical and biogeochemical processes driving the mean fluxes of O_2, CO_2, and Atmospheric Potential Oxygen (APO) in the tropical Pacific. The Equatorial Undercurrent (EUC) and the South Equatorial Current (SEC) are also shown in dark grey arrows.

ENSO strongly modulates upper ocean dynamics and biogeochemistry in the tropical Pacific. At the onset of El Niño, westerly wind anomalies excite the eastward propagation of downwelling equatorial Kelvin waves that deepen the thermocline in the eastern equatorial Pacific (McPhaden et al., 1998). Ocean-atmosphere feedbacks reinforce the full development of El Niño (Bjerknes, 1969), as sea surface temperatures (SST) warm, the easterlies slacken, and upwelling weakens, driving significant biogeochemical changes. During the well-observed El Niño event of 1997-1998, for instance, upwelling of nutrients and DIC in the central equatorial Pacific appears to have ceased for several months, biological productivity was nearly halved,

and surface pCO_2 reached values near equilibrium with the atmosphere, significantly weakening the typically strong natural outgassing of CO_2 in the tropical Pacific (Chavez et al., 1999). In the transition to La Niña conditions in mid-1998, strong upwelling resumed, biological productivity was enhanced, and CO_2 outgassing intensified (Feely et al., 2002). Whereas the influence of ENSO on the air-sea flux of CO_2 has been extensively studied for decades (Bacastow, 1976; Keeling and Revelle, 1985; Winguth et al., 1994; Chavez et al., 1999; Feely et al., 1999, 2002; McKinley et al., 2004; Long et al., 2013), little is known about corresponding impacts on O_2 (McKinley et al., 2003). Detecting the net balance and contributions of the dynamic, biological, and thermal processes driving the air-sea O_2 flux response is difficult due to their competing effects, and is further challenged by the lack of ocean biogeochemical observations that resolve the spatial and temporal extent of ENSO.

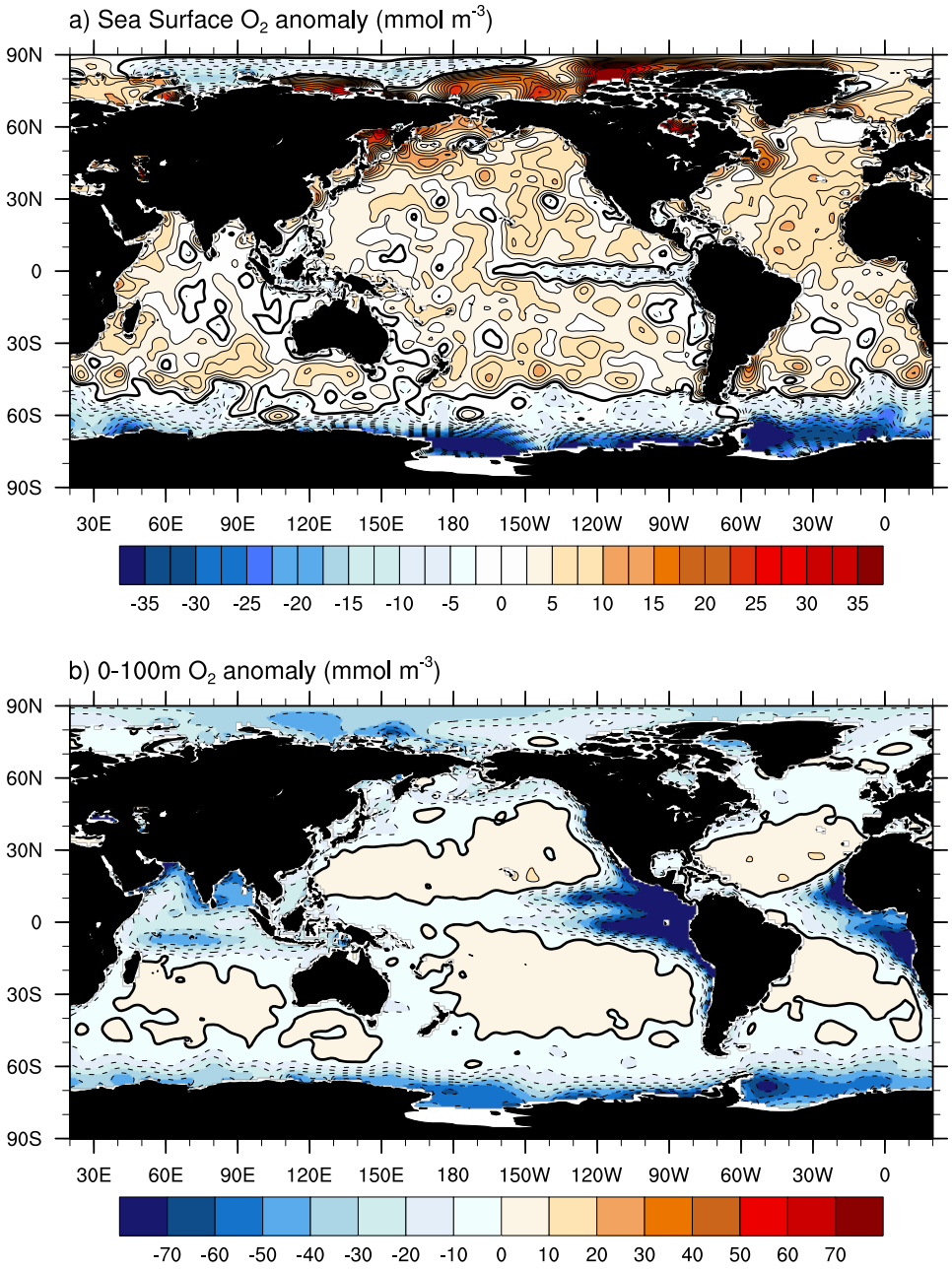

Figure 2.2. Annual mean climatology of O_2 anomaly ($\Delta O_2=[O_2]-[O_2]_{sat}$) in mmol m^{-3} at a) sea surface and b) averaged over the upper 100 m of the ocean, calculated based on O_2, temperature and salinity data from the World Ocean Atlas, 2013 (*Garcia et al.*, 2014) and the O_2 solubility equations of *Garcia and Gordon* (1992).

The imprints of ENSO on the air-sea exchange of O_2, however, are potentially detectable in time series of atmospheric O_2, measured as the $\delta(O_2/N_2)$ ratio and sampled by the Scripps Atmospheric Oxygen Program at stations throughout the Pacific basin (Figure 2.3). For instance, an increase of ocean O_2 uptake driven by cooling or ventilation of low-O_2 waters is reflected as a decrease in the atmospheric O_2 content. Terrestrial processes, however, also influence atmospheric O_2. To isolate variability due to air-sea fluxes, we use Atmospheric Potential Oxygen (APO), a tracer of ocean biogeochemistry (Stephens et al., 1998; Gruber et al., 2001). APO is calculated as follows:

$$\delta APO = \delta(O_2 / N_2) + 1.1 \cdot \frac{[CO_2]}{X_{O_2}} \quad , (1)$$

where the sum of $\delta(O_2/N_2)$ and CO_2 using the 1.1 biospheric -O_2:CO_2 molar exchange ratio cancels out the coupled influence of terrestrial photosynthesis and respiration (Severinghaus, 1995), and X_{O2} (0.2095), the atmospheric mixing ratio of O_2, converts [CO_2] from parts per million to the per meg unit used in $\delta(O_2/N_2)$ measurements. While fossil fuel combustion and oceanic uptake of anthropogenic carbon drive the observed long-term downward trend in APO (Manning and Keeling, 2006), their effects on the variability of APO on interannual timescales are negligible (Hamme and Keeling, 2008). Interannual variability in APO, thus, represents mainly changes in response to the air-sea fluxes of O_2 and CO_2. Due to buffering by carbonate chemistry, the timescale for CO_2 equilibration is about one order of magnitude slower than for O_2

(Williams and Follows, 2011); consequently, O_2 fluxes are likely to dominate APO variability on interannual timescales (Keeling and Severinghaus, 2000). APO observations thus provide an integrated constraint on the interannual variability of the air-sea O_2 flux and its coupling to climate variability.

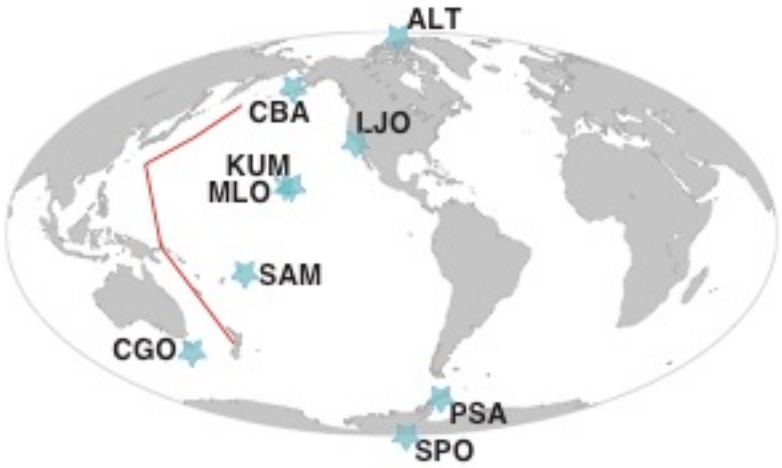

Figure 2.3. Location of Scripps APO sampling stations (blue stars) and shipboard measurement cruise lines (red line) used in Tohjima et al. (2015). Stations are abbreviated and located as follows: Alert, Canada (ALT), Cold Bay, Alaska (CBA), La Jolla, CA (LJO), Mauna Loa Observatory, HI (MLO), Kumakahi, HI (KUM), Samoa Island, USA (SAM), Cape Grim, Australia (CGO), Palmer Station, Antarctica (PSA), and South Pole Observatory, Antarctica, (SPO).

The APO response to ENSO, however, is not well understood. Using APO data from Scripps stations over the 1994-2007 period and a global atmospheric transport inversion (referred to herein as "atmospheric inversion"), Rödenbeck et al. (2008) found a moderate positive correlation between the Multivariate ENSO Index and tropical APO fluxes, suggesting that El Niño conditions drive anomalous outgassing of APO, likely associated with variations in the ventilation of the tropical

Pacific Oxygen Minimum Zone (OMZ). Recently, however, using shipboard measurements of APO along the western Pacific (red lines in Figure 2.3) over the 2002-2012 period, Tohjima et al. (2015) showed a reduction of APO in the tropical Pacific during El Niño, and an increase during La Niña. Tohjima and colleagues attribute these anomalies mainly to the effects of ENSO-related variations in atmospheric transport on surface APO distributions, reinforced by small variations in air-sea fluxes of CO_2. While the findings of Tohjima et al. (2015) seem to contradict the inferred relation between the Scripps APO record and ENSO, they may simply reflect complex phenomena that are not resolved by the sparse tropical observations network or these studies' short analysis periods.

In this study, we focus on the following questions:

i) How do ocean models simulate the APO flux response to ENSO compared to observations-based estimates?
ii) What drives the APO response to ENSO in ocean models? Specifically, what mechanisms govern the O_2 flux response to ENSO in the tropical Pacific?
iii) What is the role of atmospheric transport in driving surface variability of APO due to ENSO?

We address these questions using a combination of observations and models. First, we examine the fingerprints of ENSO on APO fluxes estimated using the atmospheric inversion method extended thru December 2015, and compare this response to APO flux simulations from 3 ocean models. To explore mechanisms driving the O_2 response to ENSO, we focus on a hindcast simulation of the Community Earth System

Model (CESM). Next, using an atmospheric transport model and APO fluxes from the CESM simulation, we evaluate the role of atmospheric transport and air-sea fluxes on surface APO anomalies due to ENSO. We conclude with a summary and a brief discussion on the oceanic O_2 cycle coupling to climate variability.

2. Methods

2.1 APO Observations and Atmospheric Inversion

We present inverse estimates of air-sea flux of APO based on data from flask samples collected by the Scripps O_2 Research Program (http://scrippso2.ucsd.edu/data) at a network of surface stations (Figure 2.3) over the January 1994 thru December 2015 period. At each station, free tropospheric air is sampled in glass flasks twice a month, and analyzed for O_2 via the $\delta(O_2/N_2)$ ratio using interferometry and for CO_2 using an infrared analyzer at the Scripps Atmospheric Oxygen Program laboratory (Keeling and Manning, 2014). APO time series from Cold Bay, Alaska and Palmer Station, Antarctica are excluded due to their shorter observational periods, noting their inclusion had no significant impact on the interannual trends in APO fluxes. We also exclude the Mauna Loa and the South Pole stations because their APO records prior to 1998 were somewhat compromised during flask sampling of $\delta(O_2/N_2)$ due to fractionation (Manning, 2001). APO fluxes are estimated based on data from 5 Scripps stations (ALT, LJO, KUM, SAM, and CGO, shown in Figure 2.3) and a global atmospheric transport inversion using TM3, an atmospheric tracer transport model, as detailed in Rödenbeck et al. (2008).

To account for autocorrelation when calculating correlations between the APO flux from the atmospheric inversion and the Niño3.4 index, statistical significance is calculated using a nonparametric method based on creating a large number of synthetic timeseries (>100,000) with similar power spectra to the original APO timeseries but with randomized phases (Ebisuzaki, 1997). Statistical significance and confidence intervals are expressed as *p*, the fraction of synthetic timeseries that show a larger magnitude of correlation with the Niño3.4 index than the original APO flux timeseries (i.e. p=0.05 refers to the 95% confidence interval).

2.2 Ocean Model Simulations

To evaluate processes driving APO flux variability, and more specifically the response of O_2 to ENSO, we focus on a hindcast simulation of the ocean and sea-ice components of CESM version 1.0 (Gent et al., 2011). CESM simulates reasonably well ENSO dynamics (Deser et al., 2012), the seasonal cycle of APO (Nevison et al., 2015), and the oceanic carbon cycle response to climate variability (Long et al., 2013). Similarly to other coarse resolution models, CESM contains significant [O_2] biases. The volume and spatial extent of OMZs in CESM, for instance, are overestimated, including the Indian and tropical Pacific OMZs (Moore et al., 2013). Nevertheless, CESM captures well the large-scale spatial pattern distribution of [O_2] (Long et al., 2016) and shows the closest match to observations in the tropical Pacific across models (Cabré et al., 2015), providing a useful tool to assess mechanisms driving O_2 variability in the upper ocean.

The CESM ocean component is the Parallel Ocean Program 2 (POP2), a z-level hydrostatic primitive equation model with spherical coordinates, a uniform zonal resolution of 1.11º, and a meridional resolution that increases from 0.27º at the Equator to 0.54º poleward of 33º (Smith et al., 2010; Danabasoglu et al., 2012). The vertical grid has 60 levels with 10 m resolution in the upper 160 m, increasing to 250 m until 3500 m depth, then remaining constant at 250 m until bottom. The model uses the Gent and McWilliams (1990) parameterization for mesoscale eddy transport, and an eddy-induced advection coefficient that varies in time and space (Danabasoglu and Marshall, 2007). The K-profile parameterization of Large et al. (1994) is used to model boundary layer dynamics with a latitude-dependent background internal wave diffusivity (Danabasoglu et al., 2012). Sea ice is simulated using the Community Ice Code version 4 (CICE4), which operates on the same grid as POP2 (Hunke and Lipscomb, 2008). Ocean biogeochemistry is represented using the Biogeochemical Elemental Cycle (BEC) model (Moore et al., 2004, 2013). BEC simulates lower-trophic-level marine ecosystem dynamics using the Nutrient-Phytoplankton-Zooplankton-Detritus paradigm, including three phytoplankton functional groups controlled by light, temperature, and nutrients (N, P, Si, and Fe), one zooplankton type, and the CO_2 and O_2 cycles (Moore et al., 2013; Long et al., 2013).

In the CESM hindcast simulation, the ocean and sea ice components of CESM are forced under the Coordinated Ocean–Ice Reference Experiments (CORE2; Griffies et al., 2009, 2012) protocol, which includes interannually-varying radiative and freshwater fluxes, as well as atmospheric state variables used to compute fluxes via

bulk formulae (Large and Yeager, 2009). Observed climatologies were used to initialize the biogeochemical fields, whereas initial conditions for ocean physics were based on outputs from a previous physics-only ocean-ice hindcast simulation (Long et al., 2013). Four 60-year cycles were run to spin up the model. During the spin up, biogeochemistry is simulated continuously whereas physical fields are set back to their initial conditions at the start of every cycle to reduce model drift. After the 4^{th} cycle, a transient simulation was run corresponding to the 1948–2008 "observed" period. To avoid the influence of discontinuities induced at the beginning of the 60-year transient simulation, we exclude the initial 12 years and thus limit our analysis to model outputs from January 1960 to December 2008.

In addition to CESM, APO fluxes from the atmospheric inversion and Scripps data are also compared to hindcast simulations of ocean components of the Institut Pierre-Simon Laplace (IPSL) model, and the Geophysical Fluid Dynamic Laboratory (GFDL) model. The IPSL simulation employs the Nucleus for European Modeling of the Ocean (NEMO) model (Madec, 2008) coupled to the Pelagic Interactions Scheme for Carbon and Ecosystem Studies (PISCES) biogeochemical model (Aumont et al., 2015). The model has 46 vertical levels, a horizontal resolution that ranges between 0.2° and 0.5° and is forced by the atmospheric fields from the DRAKKAR Forcing Set based on the ERA40 and ERA-Interim reanalysis over the 1920-2012 period (Brodeau et al., 2009; Bourgeois et al., 2016). The GFDL simulation is based on the GFDL Modular Ocean Model version 5 (MOM5) model (Griffies, 2012) coupled to the Tracers of Ocean Phytoplankton and Allometric Zooplankton (TOPAZ)

biogeochemical model version 2 (Dunne et al., 2010). GFDL-TOPAZ is forced similarly to CESM using the CORE-2 protocol (Griffies et al., 2009, 2012) over the 1948-2007 period, following Rodgers et al. (2009). The hindcast simulations of CESM, IPSL, and GFDL differ in their representation of atmospheric forcing, ocean circulation, and ocean biogeochemistry, and thus provide a first order estimate of the influence of model choice and atmospheric forcing on the simulated APO flux response to ENSO.

2.3 Air-Sea Flux Analysis

In all ocean models, the simulated air-sea fluxes of O_2 (F_{O2}), and CO_2 (F_{CO2}) are computed based on the air-sea gas exchange parameterization of Wanninkhof (1992), as:

$$F_g = K_g(1 - f_{ice})([g] - [g]_{sat}) \quad (2)$$

where f_{ice} is the surface sea ice fraction, $[g]$ is the modeled surface gas concentration, and $[g]_{sat}$ is the saturation gas concentration calculated based on surface temperature and salinity following Garcia and Gordon (1992) for O_2 and Weiss (1974) for CO_2. K_g represents the gas transfer coefficient, a function of wind speed and the temperature-dependent Schmidt numbers of O_2 and CO_2 (Keeling et al., 1998; Wanninkhof, 1992). Positive flux denotes sea-to-air flux or "outgassing", whereas negative flux describes air-to-sea flux or ocean "uptake".

We evaluate the contributions of F_{O2} and F_{CO2} to APO variability, by computing the air-sea flux of APO (F_{APO}), following Rödenbeck et al. (2008), as:

$$F_{APO} = F_{O_2} + 1.1 \cdot F_{CO_2} - \frac{X_{O_2}}{X_{N_2}} F_{N_2} \quad (3)$$

where X_{O2} (0.2095) and X_{N2} (0.7815) represent the atmospheric mixing ratios of O_2 and N_2 respectively. $F_{N2,}$ the air-sea flux of Nitrogen (N_2), is driven mainly by temperature-induced changes in gas solubility, and is computed offline at each ice-free surface grid point based on the heat flux scaling formula of Keeling et al. (1993):

$$F_{N_2} = \frac{\partial N_2^{sol}}{\partial T} \cdot \frac{Q}{\rho \cdot C_p} \quad , (4)$$

where $\partial N_2^{sol}/\partial T$ is the derivative of N_2 solubility with respect to temperature, computed based on Hamme and Emerson (2004). Q is the model net air-sea heat flux computed as the sum of short-wave, long-wave, latent and sensible heat fluxes, ρ is the density of surface water, and C_P (3993 J kg^{-1} K^{-1}) is the specific heat capacity of seawater.

Air-sea O_2 exchange is driven by processes affecting the surface mixed layer O_2 inventory and saturation state. These include thermally-driven O_2 fluxes, net community production of O_2, and the vertical transport of subsurface low-O_2 waters into the mixed layer, referred to here as "ventilation". Assuming instantaneous air-sea gas exchange, we estimate the contribution of these processes by decomposing F_{O2} into thermal (F_{THERM}), net community production (F_{NCP}), and ventilation (F_{VENT}) fluxes, following Nevison et al. (2015), as:

$$F_{O_2} = F_{THERM} + F_{NCP} + F_{VENT} \quad , (5)$$

Similarly to F_{N2}, the thermal flux of O_2, F_{THERM}, is calculated as:

$$F_{THERM} = \frac{\partial O_2^{sol}}{\partial T} \cdot \frac{Q}{\rho \cdot C_p}, \quad (6)$$

where $\partial O_2^{sol}/\partial T$ is the derivative of O_2 solubility with respect to temperature at sea surface, calculated following Garcia and Gordon (1992). F_{NCP} represents the O_2 flux due to the net community production of O_2 in the mixed layer, which we approximate as:

$$F_{NCP} = \int_{0m}^{100m} [prod(O_2) - cons(O_2)]dz, \quad (7)$$

where $prod(O_2)$ and $cons(O_2)$ represent the model source and sink terms of O_2 due to photosynthesis and respiration, integrated over the upper 100 m of the ocean. This depth is close to the annual mean mixed layer depth over most of the ocean, as well as the depth of net biological carbon uptake in CESM (Jin et al., 2007; Doney et al., 2009). This estimate is also adequate for an upwelling zone, such as the equatorial Pacific, where waters down to 100 m are upwelled relatively quickly into the mixed layer. F_{VENT}, the air-sea flux of O_2 driven by ventilation, is calculated as a residual in Eq. (5) and represents mainly the component of the air-sea flux driven by upwelling or vertical mixing of O_2-depleted subsurface waters into the mixed layer. Note that upwelling of cold waters also leads to a thermal influx of O_2; changes in the temperature-dependent solubility of O_2 due to upwelling are thus implicitly accounted for in F_{THERM} as heat fluxes involve ocean dynamics.

As noted above, this decomposition method assumes that air-sea equilibration occurs instantly. Thus, the F_{VENT} residual term likely includes contributions from changes in gas exchange efficiency due to the dependence of the gas transfer velocity K_g on wind intensity, which is sensitive to ENSO. Analysis of model results indicates that the contribution of this effect to F_{O2} variability is an order of magnitude smaller than the contributions of O_2 saturation anomalies ($\Delta O_2=[O_2]-[O_2]_{sat}$). F_{VENT} also likely includes small residuals that arise from the approximate nature of Eqs. (6) and (7), which assume that the mixed layer equilibrates instantly in response to heat fluxes and biological production, and neglect the effects of mixing and penetration of shortwave irradiance below the mixed layer on biological production and gas supersaturation (Dietz and Oschlies, 2005). While disequilibrium in air-sea gas exchange was suggested to damp the magnitude (by ~20%) and induce a short lag (2 weeks) in the annual cycle of air-sea O_2 exchange (Dietz and Oschlies, 2005; Jin et al., 2007), its contribution on interannual timescales has not been evaluated yet, and a detailed analysis of these effects is outside the scope of this study.

To emphasize interannual variability, air-sea flux anomalies from the atmospheric inversion and the hindcast simulations for all models are calculated by removing the monthly mean seasonal cycle and a linear trend from all time-series, and smoothed using a Lanczos 18-months low-pass filter (Duchon, 1979). The impacts of ENSO are quantified using a linear least squares regression of flux anomalies onto the standardized Niño3.4 index, calculated following Trenberth (1997) for each hindcast simulation. Statistical significance is calculated using a t-test, taking autocorrelation

into account by adjusting the degree of freedom using the lag-one autocorrelation of the series (Zwiers and von Storch et al., 1995).

2.4 Atmospheric Transport Simulations

To evaluate the effects of changes in atmospheric transport on surface APO anomalies, we use the TM3 atmospheric transport model (Heimann and Körner, 2003). Forward atmospheric simulations are performed using two different fluxes from the CESM hindcast simulation:

1) CLM_FLX transports the climatological annual cycle of F_{APO}, calculated as the long-term mean of linearly detrended F_{APO} at each month in CESM. This simulation isolates the effects of atmospheric transport variability on surface APO anomalies since the air-sea fluxes do not vary from year to year.
2) VAR_FLX transports the APO fluxes, as simulated by the CESM hindcast simulation where they vary from year to year. This atmospheric simulation thus includes the effects of variability in atmospheric transport as well as in air-sea fluxes.

These atmospheric transport simulations are carried out over the January 1970 to December 2008 period using 6-hourly wind fields from the updated NCEP reanalysis (Kalnay et al., 1996). The seasonal cycle and long-term trends are removed from all transport simulations similarly to the air-sea flux analysis, and smoothed using a 6-months low-pass filter to reduce noise associated with atmospheric synoptic events.

3. Results and Discussion

a. Comparison of Inversion vs. Ocean Simulations of F_{APO} Variability

Figure 2.4 shows the global and tropical air-sea flux of APO inferred from the atmospheric inversion and Scripps observations (F_{APO_INV}), compared to the CESM, IPSL, and GFDL "ocean" simulations (F_{APO_CESM}, F_{APO_IPSL}, F_{APO_GFDL}). Note that F_{APO_INV} is scaled down by 50% in Figure 2.4a-c and 4e-g to allow for phase comparison with the ocean simulations. F_{APO_INV} shows significant variability globally (1σ=±84 Tmol yr^{-1}) as well as in the tropics (1σ=±66 Tmol yr^{-1}). The ocean simulations capture key features of this variability, including the peaks of 1997-1998, 2002-2003, and, for the extended IPSL simulation, the peak of 2009-2010. There are, however, notable disagreements between the atmospheric inversion and ocean simulations. These disagreements include a large negative anomaly during 2000-2001 and a positive anomaly during 2005 found in F_{APO_INV} but not in the ocean simulations. Across all ocean simulations, the magnitude of interannual variability in F_{APO} is significantly underestimated (>50%) globally and regionally when compared to F_{APO_INV} (Table 1). The underestimate of F_{APO} variability shown in these models is likely related to systemic model biases that we discuss in Section 4.

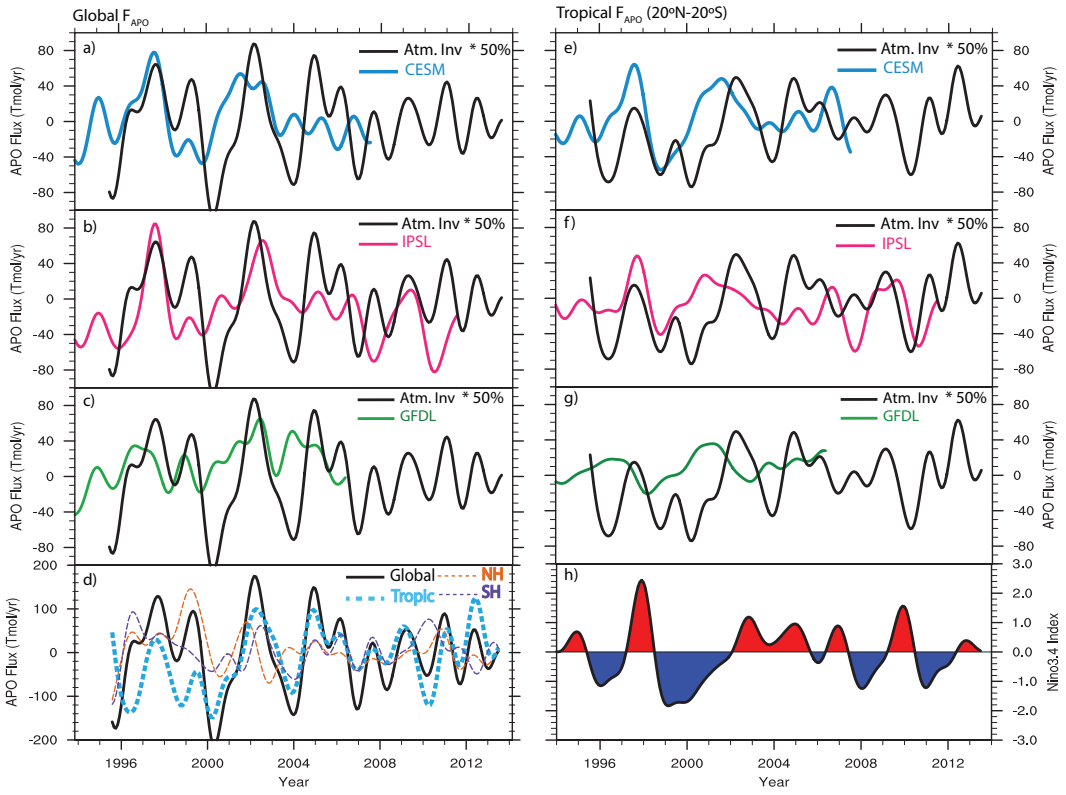

Figure 2.4. Comparison of global F_{APO} from the atmospheric inversion (black; scaled by 50%) vs. a) CESM, b) IPSL, and c) GFDL. d) Regional contributions to F_{APO} inversion integrated over the tropics (blue, 20ºN-20ºS), northern extratropics (NH; orange, 20ºN-90ºN), and southern extratropics (SH, purple 20ºS-90ºS). Right panel e)-g) shows a similar comparison of F_{APO} as a)-c) but for the tropical region (20ºN-20ºS). Similarly to the global integral, the tropical F_{APO} estimate from the atmospheric inversion is scaled by 50% to allow for phase comparison to the ocean model simulations of F_{APO}. h) Niño3.4 index over the comparison period, (data obtained from NOAA website: http://www.cpc.ncep.noaa.gov). All time series are smoothed using an 18-months lanczos low-pass filter. First and last 18 months of time series are omitted due to edge effects. Positive flux denotes sea-to-air flux or "outgassing".

The tropical region (20ºN-20ºS) plays a major role in driving anomalies in the global F_{APO_INV} (Figure 2.4d). We find a positive correlation between anomalies in tropical F_{APO} and the Niño3.4 index in the atmospheric inversion (R_{APO_inv}=0.46, 5-months F_{APO} lead, $p<0.01$) as well as in the CESM and IPSL simulations (R_{CESM}=0.60

at 5-months F_{APO} lead; R_{IPSL}=0.59 at 4-months F_{APO} lead). This relation suggests that, in both inversion and these ocean simulations, anomalous outgassing of APO in the tropics leads El Niño events, and conversely, anomalous drawdown of APO leads La Niña.

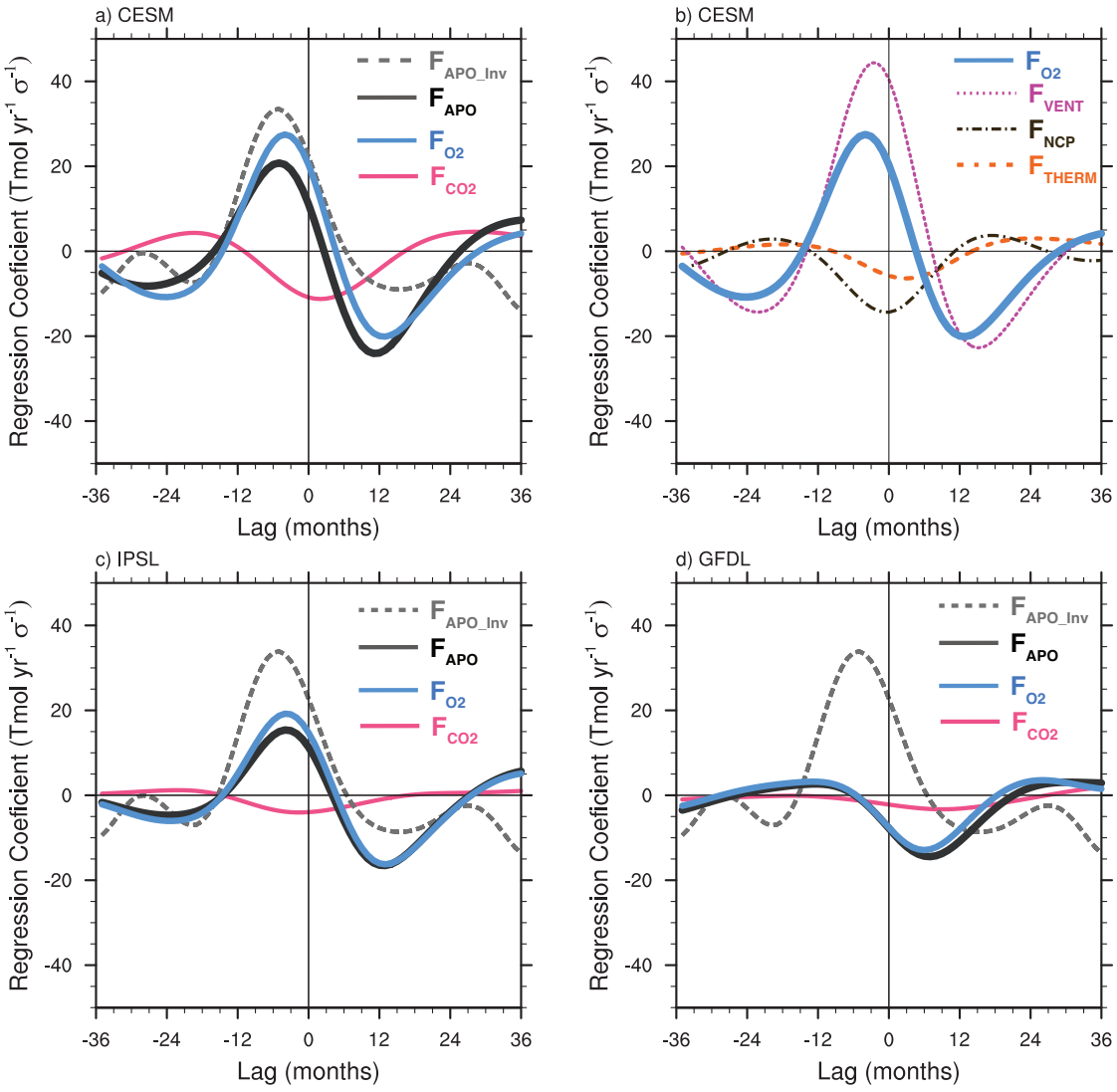

Figure 2.5. Lag regression of Niño3.4 index vs. a) tropical (20ºN-20ºS) F_{APO}, F_{O2} and F_{CO2} in CESM, and b) tropical F_{O2} including flux components in CESM. c) and d) same as a) but for IPSL and GFDL. The atmospheric inverse F_{APO} is also shown (dashed grey) for comparison. All time series are smoothed using an 18-months low-pass filter prior to lag regression. Positive flux denotes sea-to-air flux or "outgassing".

The atmospheric inversion shows an estimated APO flux response to ENSO of about 34 Tmol yr^{-1} σ^{-1} (σ here refers to one standard of deviation of the Niño3.4 index). Table 1 and Figure 2.5a and 5c show that both CESM and IPSL capture the sign and phase of this response to ENSO, but underestimate its magnitude. GFDL, on the other hand, is in general disagreement in sign, magnitude and phase with both the inversion and other ocean simulations (Figure 2.4e-g and Figure 2.5d), showing a negative lagged F_{APO} response to the Niño3.4 index (R_{GFDL}=-0.67, 7 months F_{APO} lag). While this negative response also exists in CESM and IPSL with different lags, these models show a positive APO anomaly leading the Niño3.4 index that is not simulated by GFDL (Figure 2.5d). The similar results shown in CESM and IPSL, which are forced differently (NCEP vs. ERA-I), contrasted with GFDL, which is forced similarly to CESM, suggest that differences in model representation of ocean circulation and/or biogeochemistry, rather than atmospheric forcing, drive model divergence in the F_{APO} response to ENSO.

Table 2.1. Comparison of global and tropical F_{APO} variability from the atmospheric inversion and hindcast model simulations of CESM, IPSL, and GFDL.

APO Flux Product	1σ of Global F_{APO} (Tmol yr^{-1})	1σ of Tropical F_{APO} (Tmol yr^{-1})	Maximum Lag Correlation of Tropical F_{APO} vs. Niño3.4	Tropical F_{APO} Response to Niño3.4 Index (Tmol yr^{-1} σ^{-1})
Atmospheric Inversion	± 84.24	±66.23	0.46 (5 mon F_{APO} lead)	33.88
CESM	±35.77	±29.87	0.62 (5 mon F_{APO} lead)	20.79
IPSL	±40.40	±23.21	0.59 (4 mon F_{APO} lead)	15.38
GFDL	±35.83	±19.28	-0.67 (7 mon F_{APO} lag)	-14.44

b. Drivers of Tropical F_{APO} Variability

In all models, the tropical F_{APO} response to ENSO is driven primarily by F_{O2} (Figure 2.5). In CESM, for instance, the simulated F_{APO} response to ENSO of 21 Tmol

APO yr^{-1} σ^{-1} is driven by anomalous outgassing of O_2 (28 Tmol yr^{-1} σ^{-1}), and is counteracted by a lagged anomalous uptake of CO_2 (-11 Tmol yr^{-1} σ^{-1}) damping the APO response (Figure 2.5a). F_{N2} also serves to damp F_{APO} variability, though its contribution to the total F_{APO} variability is very small compared to F_{O2} (Figure 2.6a). The dominance of F_{O2} on the interannual variability of F_{APO} is expected. Unlike CO_2, O_2 is not buffered by the ocean's inorganic carbonate chemistry, which allows O_2 a faster equilibration response timescale and a larger air-sea flux amplitude than CO_2, lending further confidence in using APO as a proxy for air-sea O_2 exchange on interannual timescales.

Due to its central role in driving F_{APO} variability, we focus on the tropical F_{O2} response, which shows an even stronger positive correlation to the Niño3.4 index in CESM (R_{FO2}=0.78, 4-months F_{O2} lead) compared to F_{APO} (R_{FAPO} = 0.62, 5 months lead; Table 1). The 4-months lead of the F_{O2} response likely reflects the sensitivity of surface ΔO_2 to changes in ocean dynamics, which lead the full development of El Niño events, typically defined by the mean SST anomaly of the Niño3.4 region (Trenberth, 1997). This tight ENSO modulation of tropical F_{O2} variability reflects significant changes in the upper equatorial Pacific O_2 budget (upper 500m of Pacific 5ºN-5ºS), whereby the upper ocean anomalously loses O_2 to the atmosphere during El Niño, and, conversely, gains more O_2 during La Niña (Figure 2.6b-c).

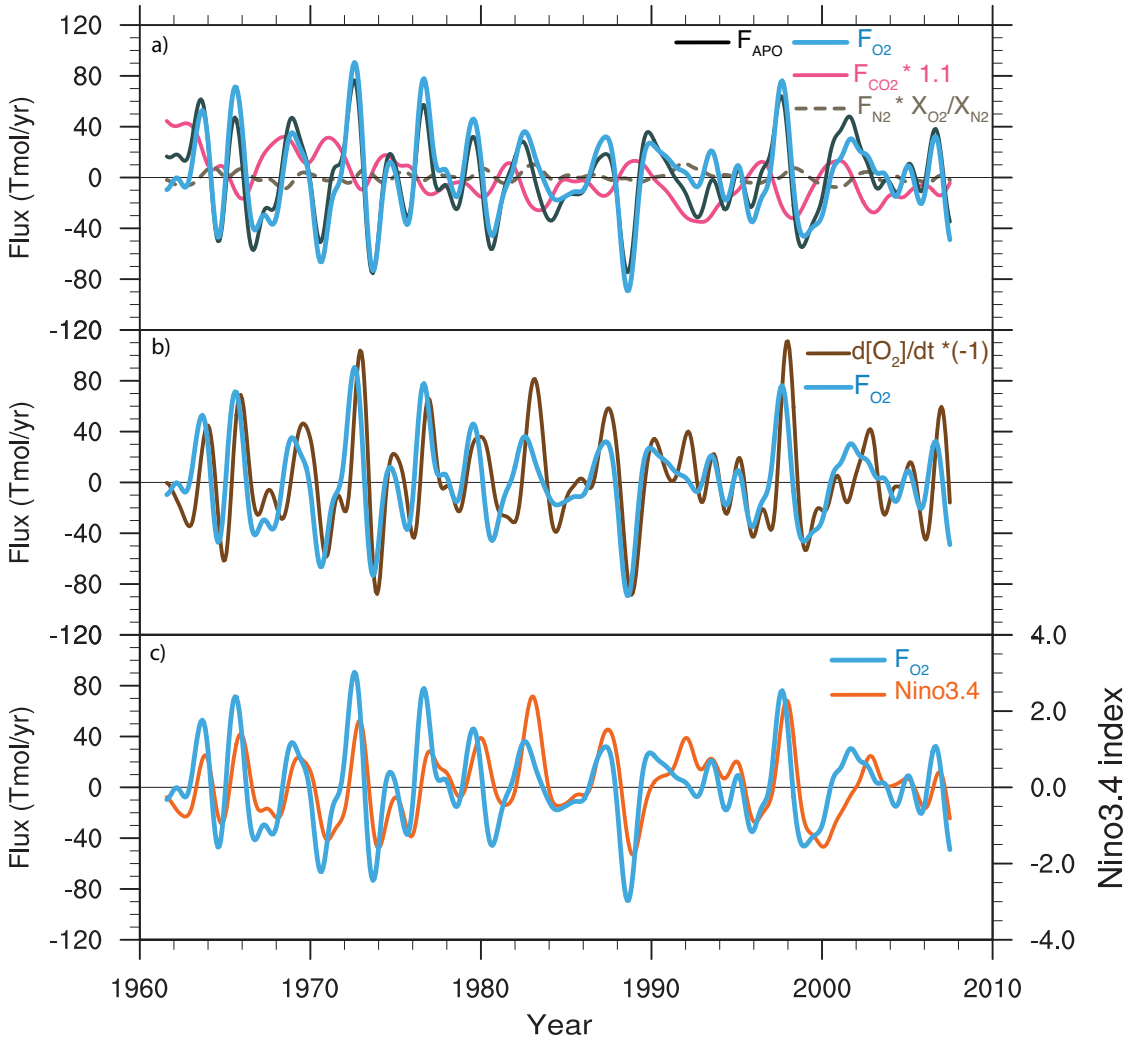

Figure 2.6. Time series from the CESM hindcast simulation of anomalies in a) tropical F_{APO} (black), F_{O2} (blue), F_{CO2} (magenta), and F_{N2} (dashed grey), scaled by their contributions to F_{APO} following Eq. 3; b) tropical F_{O2} (blue) vs. volume integrated d[O_2]/dt*(-1) over the upper 500 m of the upper equatorial Pacific (5ºN-5ºS; brown); and c) tropical O_2 fluxes (blue) vs. Niño 3.4 index (orange). All time series are smoothed using an 18-months low-pass filter. First and last 18 months of time series are omitted due to edge effects. Positive flux denotes sea-to-air flux or "outgassing".

The spatial pattern of the O_2 flux response to ENSO, as simulated in CESM, is illustrated in Figure 2.7a-b, which shows a regression of SST and F_{O2} anomalies onto the Niño3.4 index. The O_2 flux response to El Niño is marked by i) significantly reduced O_2 uptake (i.e., strong anomalous outgassing) along the equatorial Pacific

cold tongue and the upwelling regions of the eastern tropical Pacific, and ii) anomalous weak uptake west of 180º and poleward of the Equator. Outside the tropics, weaker O_2 flux anomalies are also evident, with uptake in the North Pacific and outgassing in the Southern Ocean during El Niño. These anomalies are associated with changes in sea level pressure (SLP) and SST (Figure 2.7a) driven by ENSO teleconnections (Trenberth et al., 2002; Alexander et al., 2002). Similar F_{O2} response patterns are simulated by IPSL and GFDL (Figure 2.7c-d), though regional contributions differ between models. IPSL, for instance, shows a less pronounced zonal gradient in the equatorial F_{O2} response than CESM, and a weaker tropical F_{O2} response overall. GFDL, on the other hand, shows more confined outgassing along the eastern equatorial Pacific, counteracted by a significant opposing response outside the cold tongue, likely explaining its negative and weak integrated F_{APO} response to ENSO (Figure 2.5d).

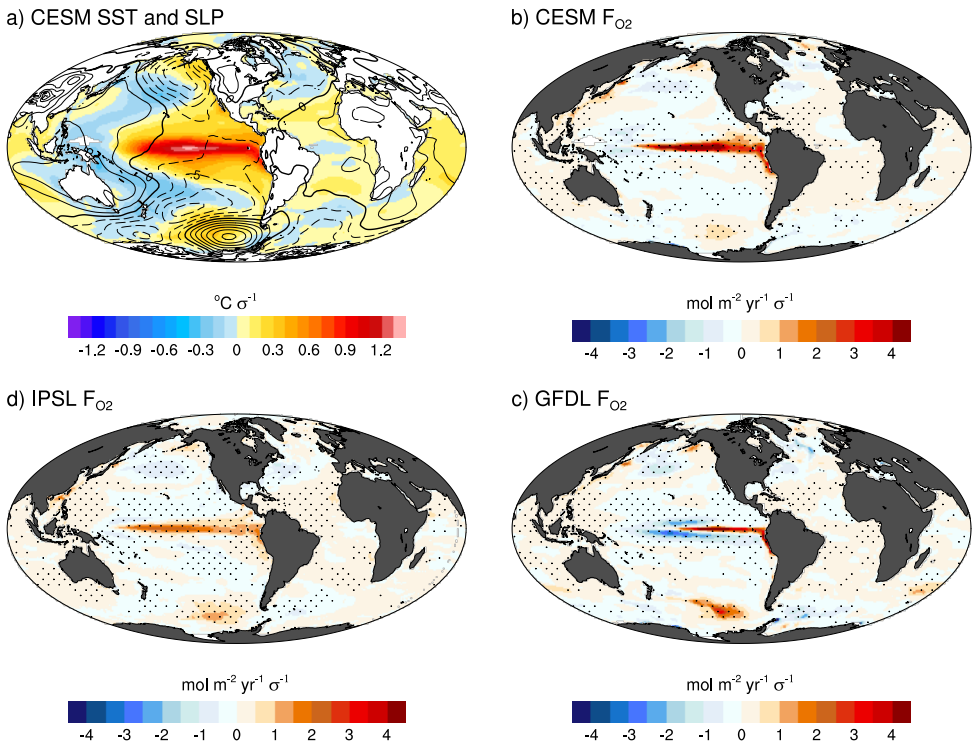

Figure 2.7. Zero-lag regression of Niño 3.4 index vs. anomalies in a) sea surface temperature (SST; shading) and sea level pressure (SLP; contours), and O_2 fluxes from b) CESM, c) IPSL, d) GFDL**.** Dashed contours indicate negative SLP anomalies, contoured every 0.25 hPa. No smoothing was performed on time series prior to regression here to highlight spatial character of anomalies at the peak of ENSO. Stippling indicates 95% significance. Positive flux denotes sea-to-air flux or "outgassing".

c. Mechanisms of ENSO-related Variability in Tropical F_{O2}

We now examine mechanisms driving the O_2 response to ENSO in CESM, focusing on the tropical Pacific region. ENSO-driven variability in tropical F_{O2} involves components that partly counteract each other (Figure 2.5b). F_{VENT}, the ventilation component of the O_2 flux, contributes an estimated ±44 Tmol yr^{-1} σ^{-1} (3-months F_{VENT} lead) to the net F_{O2} response, which is partly offset by F_{THERM}, the thermal component of O_2, and F_{NCP}, the net community production of O_2. Figure 2.8a-d illustrate the spatial extent of these responses in the tropical Pacific, showing a

significant reduction of the ventilation-driven uptake of O_2 along the equatorial cold tongue, that yields a larger flux impact than the concurrent weak reductions in biological production and thermal outgassing of O_2 during El Niño. Conversely, during La Niña, F_{VENT} is intensified significantly more than the counteracting increase in F_{NCP} and F_{THERM}. In the following, we elaborate on mechanisms driving the F_{O2} response during El Niño, noting that the reverse describe La Niña conditions.

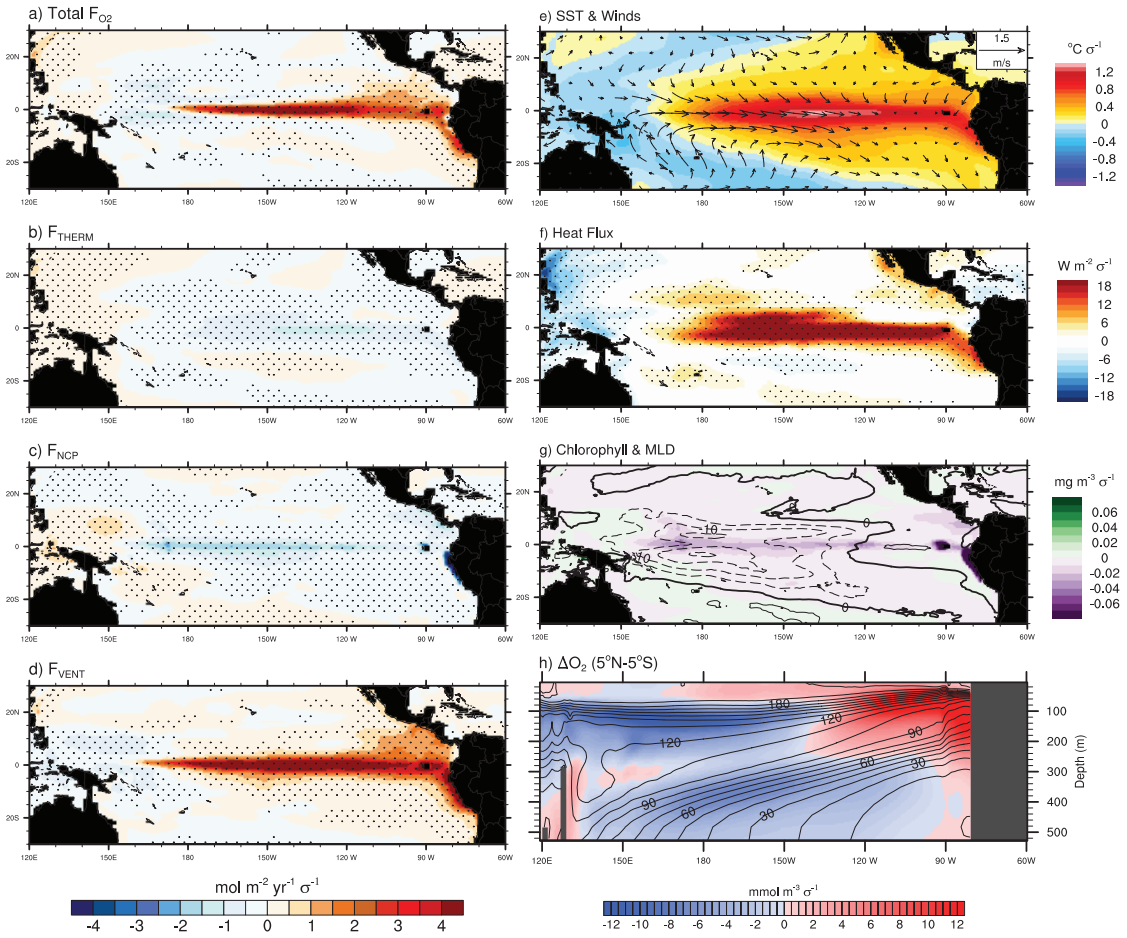

Figure 2.8. Zero-lag regression of standardized Niño3.4 index vs. anomalies in a) O_2 flux and its components: b) thermal flux F_{THERM}, c) net biological production flux F_{NCP}, and d) ventilation flux term F_{VENT}, alongside e) SST (shading) and winds (arrows), f) heat flux, g) surface chlorophyll concentration (shading) and mixed layer depth (MLD) in contours, and h) O_2 supersaturation calculated as $\Delta O_2=[O_2]-[O_2]_{sat}$, superimposed on contours of climatological mean $[O_2]$ (mmol m^{-3}), shown in depth vs. longitude, averaged over the 5ºN-5ºS band. Dashed

(Figure 2.8 continued) contours indicate negative MLD anomalies, contoured every 5 m. No smoothing was performed on time series prior to regression here to highlight spatial character of anomalies at the peak of ENSO. Positive flux denotes anomalous sea-to-air flux or "outgassing". Stippling indicates 95% significance.

Figure 2.8d shows the F_{VENT} response to El Niño as intense anomalous outgassing that extends broadly along the Equator from the Peruvian upwelling system in the east to 160ºE across the basin to the west. Figure 2.8h shows this F_{VENT} anomaly is associated with significant changes in subsurface ΔO_2 changes (>10 mmol m^{-3} σ^{-1}) down to 400 m in depth. These equatorial ΔO_2 anomalies show a strong zonal dipole and maxima along the climatological equatorial oxycline (50-150 m in depth), driven by the vertical displacement of isopycnals as the thermocline deepens in the east and shoals in the west during El Niño. The lack of wind anomalies in the eastern tropical Pacific despite large anomalies in F_{VENT} (Figure 2.8d-e) and the 3-month lead of the F_{VENT} response suggest that the main physical driver affecting ΔO_2 and F_{VENT} in this region is remote forcing by the eastward propagation of equatorial Kelvin waves. Kelvin waves act to deepen the eastern equatorial Pacific thermocline (McPhaden et al., 1998; Feely et al., 2002), leading to shallower upwelling, reduced supply of O_2-depleted waters to the surface, and weakened O_2 ingassing. On the other hand, the central equatorial Pacific (130ºW-180ºW) exhibits significant weakening of the easterlies during El Niño (Figure 2.8e), and is thus sensitive to the localized effects of winds on upwelling rates. The central equatorial Pacific anomaly also likely contains small contributions from the eastward propagation of warm pool waters (Radenac et al., 2005), since these waters were not exposed to intense upwelling and are well

equilibrated with the atmosphere. The simulated surface ΔO_2 response is in general agreement with the observed surface O_2 supersaturation reported by Stephens (1999) along 120ºW-140ºW during the El Niño of 1997-98, suggesting the elimination during this event of the typically high O_2 undersaturation observed along the equator (Wanninkhof et al., 1995).

F_{NCP} acts to offset the total F_{O2} response to ENSO by -14 Tmol yr^{-1} σ^{-1} (0-lag) over the tropical Pacific region (Figure 2.5b). ENSO-related variability in F_{NCP} in CESM is localized along the eastern tropical Pacific coast and along the equator thru 160ºE (Figure 2.8c). The spatial pattern in the F_{NCP} anomalies is accompanied by simulated changes in surface chlorophyll concentration (Figure 2.8g), consistent with the fact that variability in photosynthesis rather than respiration drives changes in the net biological production of O_2 in the euphotic zone. Observations show similar impacts of ENSO on primary productivity (Chavez et al., 1999; Behrenfeld et al., 2006), driven by region-specific changes in nutrients supply and light availability. In the eastern equatorial Pacific, changes in net primary productivity are especially sensitive to the effects of Kelvin waves on the depth of the nutricline (Chavez et al., 1999). In the central Pacific, reduced solar radiation due to enhanced atmospheric convection and the eastward migration of the nutrient-deficient warm pool may also weaken biological productivity in this region (Park et al., 2011; Feely et al., 2002).

F_{THERM} contributes only weakly to the F_{O2} response over the tropical Pacific in CESM, damping the total F_{O2} magnitude by -6 Tmol yr^{-1} σ^{-1} (3-months F_{THERM} lag). The sign of its response is nevertheless intriguing. Given the surface warming of the

tropical Pacific during El Niño, reduced surface O_2 solubility might be expected to drive thermal outgassing of O_2 (Rödenbeck et al., 2008, Tohjima et al., 2015). F_{THERM}, however, exhibits a broad anomalous uptake of O_2 during El Niño (Figure 2.8b). This counterintuitive response arises from the fact that during El Niño, even though tropical Pacific SSTs are warmer, positive heat flux anomalies act to cool the upper ocean (Figure 2.8f; Wang and McPhaden, 2001; Roemmich and Gilson, 2011). Since thermally-driven gas exchange scales with heat fluxes rather than SSTs (Keeling et al., 1993), reduced equatorial heat uptake leads to thermal O_2 flux into the ocean during El Niño.

In the western equatorial Pacific, the response of F_{O2} to ENSO is weaker and of opposite sign to that of the eastern and central Pacific (Figure 2.8a). The shoaling of the western equatorial Pacific thermocline by the westward propagation of Rossby waves and the eastward migration of the warm pool erodes the fresh "barrier" layer maintained by enhanced precipitation that typically caps upwelling (Feely et al., 2002). As a result, O_2-poor waters are entrained to the surface, strengthening the ventilation component of the O_2 flux during El Niño, illustrated in Figure 2.8d and 8g by a negative horseshoe-like F_{VENT} feature and shoaling of mixed layer depth in the western tropical Pacific. Though weak, the opposite response of F_{O2} in this region creates a significant zonal gradient along the Equator that is relevant to long-term atmospheric and ocean observations of the western Pacific (e.g., Tohjima et al., 2015).

d. APO Modulation by Atmospheric Transport

The influence of ENSO on atmospheric distributions of APO includes contributions from variations in air-sea fluxes as well as changes in atmospheric circulation (e.g., weakening of easterly winds). We isolate the contribution of atmospheric transport by comparing two forward atmospheric transport simulations forced by simulated APO fluxes from CESM and NCEP winds as described in section 2.4: 1) CLM_FLX is an atmospheric transport simulation driven by climatological APO fluxes and interannually varying winds, isolating the effects of atmospheric transport on surface APO anomalies; and 2) VAR_FLX is an atmospheric transport simulation driven by both interannually varying fluxes and winds, containing the effects of both atmospheric transport and air-sea flux variability. The CLM_FLX simulation shows significant APO variability in the North Pacific and North Atlantic, but much weaker variance in the mid and low latitudes (Figure 2.9a). In contrast, VAR_FLX shows widespread APO variability globally, with pronounced variations over regions of high air-sea flux variability such as the eastern and central equatorial Pacific and the Southern Ocean (σ>4 per meg, Figure 2.9b). These atmospheric transport simulations suggest that while atmospheric transport alone can generate APO variability at northern high latitudes, the variability in surface APO at low latitudes and in the Southern Ocean is driven primarily by anomalies in air-sea fluxes.

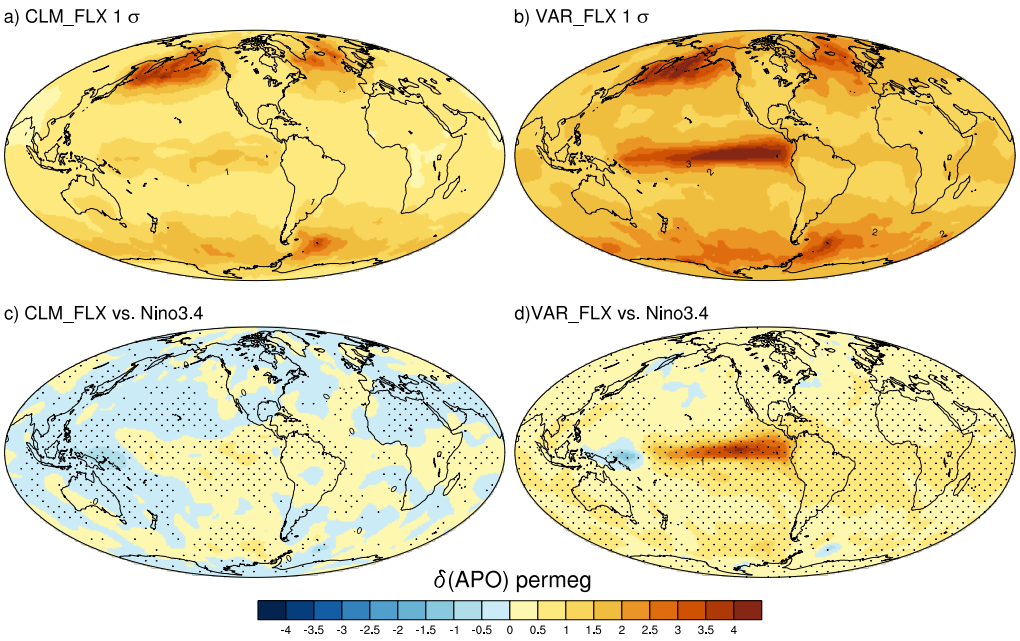

Figure 2.9. Effects of atmospheric transport on APO variability, shown here as the standard deviation of surface **δ**APO (per meg) simulated using a) climatological CESM APO fluxes (CLM_FLX) and b) variable CESM APO fluxes (VAR_FLX), both transported in TM3. The signature of ENSO is shown as regression of Niño 3.4 index vs. anomalies in surface atmospheric **δ**APO from c) climatological and d) variable APO fluxes in per meg σ^{-1}. Stippling indicates 95% significance.

The imprints of ENSO on atmospheric transport of APO are illustrated in Figure 2.9c, which shows a regression of APO anomalies from CLM_FLX in the lowest layer of the model against the Niño3.4 index. Figure 2.9c shows reduced APO in the western equatorial Pacific countered by a small increase in the eastern equatorial Pacific during El Niño. This effect is likely driven by weakened easterly winds and westerly wind bursts (Figure 2.8e), causing an eastward shift in the climatological equatorial APO maximum during El Niño. In the VAR_FLX case, however, substantially larger APO increases occur in the eastern and central equatorial Pacific (Figure 2.9d), driven by ENSO-related anomalies in the air-sea flux of O_2. Figure 2.9c

and 9d suggest that the atmospheric transport effects tend to reinforce the zonal asymmetry driven primarily by the air-sea APO flux response to ENSO, yielding a significant zonal dipole in surface APO distribution during ENSO events.

We illustrate the regional contributions of atmospheric transport and air-sea fluxes in Figure 2.10, which shows the simulated annual mean surface APO meridional profile along the eastern (120ºW) and western (160ºE) Pacific during the strong El Niño of 1997-98 and La Niña of 1998-99. In both the CLM_FLX and VAR_FLX atmospheric transport simulations (Figure 2.10a and 10c), the western equatorial Pacific shows a similar increase in APO of about 5 per meg from El Niño to La Niña, suggesting changes in atmospheric transport drive most of the surface APO variability in this region. In the eastern equatorial Pacific, however, there is a substantial decrease of 16 per meg in VAR_FLX from El Niño to La Niña, a value that is not replicated by CLM_FLX, which only shows a 5 per meg decrease. Figure 2.10 suggests that while ENSO-related changes in atmospheric transport drive most of the surface APO variability in the western tropical Pacific, air-sea flux anomalies dominate the larger surface atmospheric variability of APO found in the eastern and central equatorial Pacific. For reference, the VAR_FLX annual mean APO distribution for both years are shown in Figure 2.10e and 10f, emphasizing both the zonal shift in the equatorial APO maximum, as well as a significant change in the global atmospheric APO content due to variability in the equatorial O_2 flux.

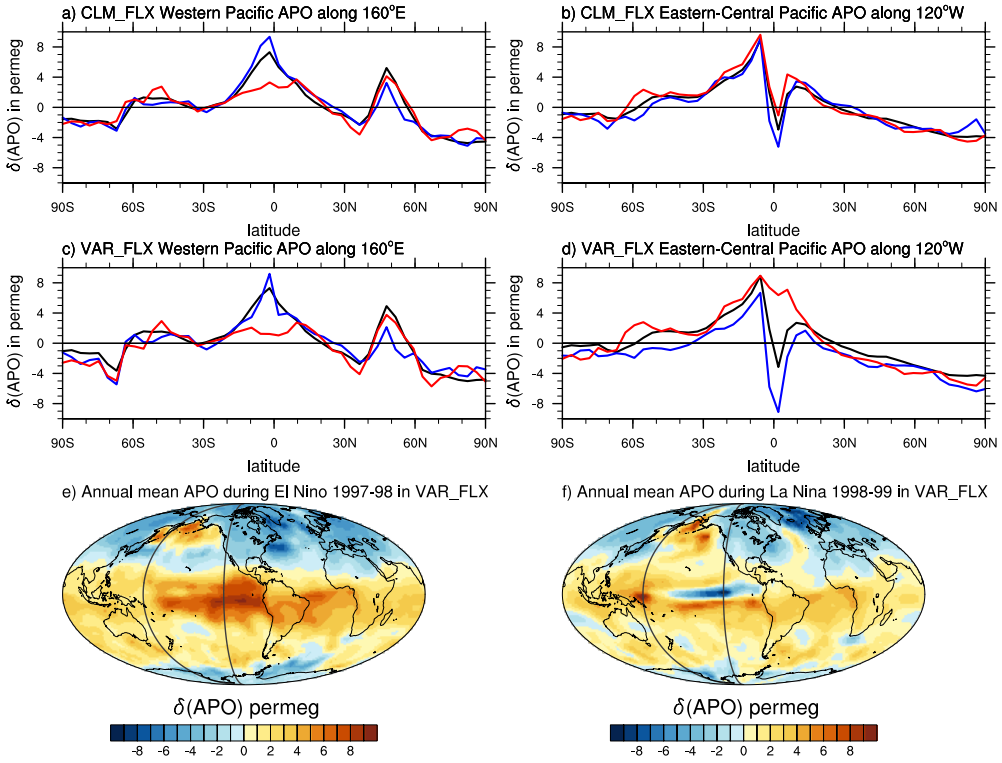

Figure 2.10. Meridional profile of the annual mean surface APO during the 1997-1998 El Niño (red), the 1998-1999 La Niña (blue), and the long-term mean (black) along 160ºE (left) and 120ºW (right) for CLM_FLX (top) and VAR_FLX (center) simulations. Bottom panel show annual mean APO from the VAR_FLX simulation for (e) the 97-98 El Niño year, and (f) 98-99 La Niña year, calculated from July thru June. Black lines in maps indicate 160ºE and 120ºW.

4. Summary and Implications

The impacts of ENSO on air-sea O_2 exchange are significant and complex, involving interactions between biogeochemical and physical processes, as illustrated in Figure 2.11. The atmospheric inversion and ocean model simulations presented here indicate that, in an anomalous sense, the upper ocean loses O_2 to the atmosphere during El Niño, and gains O_2 during La Niña. In CESM, these anomalies are driven by significant modulation of the O_2 content in the upper equatorial Pacific by coupled

ocean-atmosphere dynamics. During El Niño, the deepening of thermocline waters in the eastern equatorial Pacific and the weakening of upwelling lead to significant reductions in the ventilation of O_2-deficient waters, driving anomalous O_2 outgassing. El Niño is also associated with diminished biological productivity and net ocean heat loss, which drives anomalous uptake of O_2. Conversely, during La Niña, intensified upwelling of shoaling thermocline waters strongly reinvigorates the ventilation of low-O_2 waters while weakly enhancing the biological production and thermal outgassing of O_2. The net balance of these effects on the O_2 flux response is dominated by the ventilation effect, so that shallower and weaker upwelling during El Niño leads to anomalous O_2 outgassing, whereas deeper and intensified upwelling during La Niña drives anomalous O_2 uptake. Accounting for most of the APO flux variability, these O_2 flux anomalies are strongly localized along the eastern and central equatorial Pacific and are accompanied by a weaker response of the opposite sign in the western tropical Pacific, driving a zonal gradient in the air-sea O_2 flux response to ENSO.

In the atmosphere, the zonal dipole in surface APO anomalies driven by tropical Pacific F_{O2} is further reinforced by changes in atmospheric wind patterns, reconciling the apparently conflicting APO observations of Tohjima et al. (2015) in the western tropical Pacific with the APO inversion of Rödenbeck et al. (2008). In agreement with Tohjima et al. (2015), our simulations show that APO variability in the western equatorial Pacific is indeed driven primarily by ENSO-related changes in atmospheric transport. We find, however, that the dominance of this atmospheric transport effect is confined to the western equatorial Pacific, and that variations in air-

sea fluxes drive the larger surface APO anomalies found in the eastern and central equatorial Pacific.

The magnitude of the APO response in the eastern and central equatorial Pacific is likely model-dependent and is currently poorly sampled. Shipboard measurements of APO in this region (Battle et al., 2006) continued over the past decade may provide improved constraints on the integrated response of the upper ocean O_2 cycle to tropical climate variability. Atmospheric synoptic events, however, can induce substantial variations in this region (Stephens et al., 2003), necessitating long-term observations to filter out short-term variability. Kiritimati Island, Kiribati (2°N, 157°W), located downwind of the epicenter of air-sea O_2 flux variability, is ideally situated for constraining the magnitude of APO variability in the tropical Pacific and its zonal gradient. A new atmospheric O_2 measurement station at Kiritimati Island could thus substantially improve the tropical Pacific sampling capabilities of the Scripps network shown in Figure 2.3.

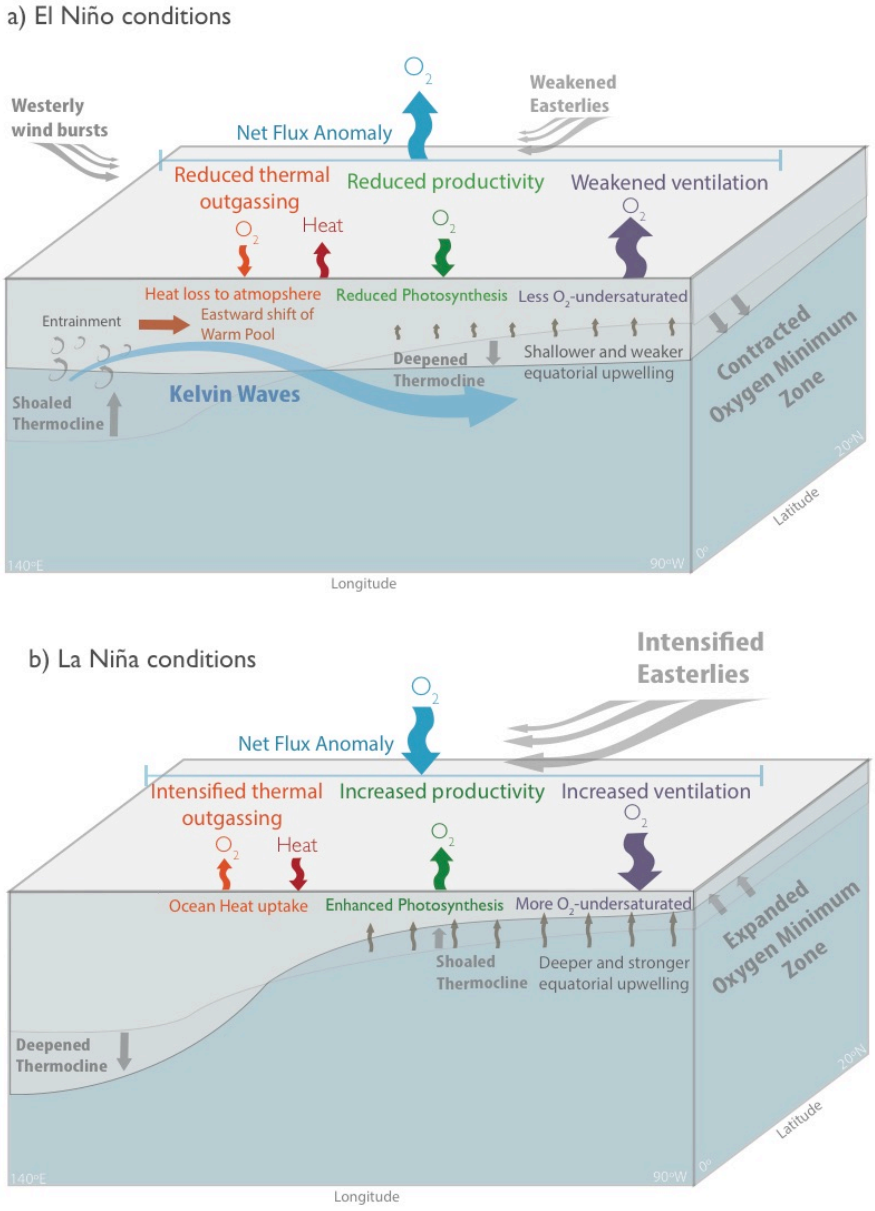

Figure 2.11. Schematic of anomalies in O_2 fluxes and main driving processes in the tropical Pacific during a) El Niño and b) La Niña conditions.

Multiple lines of evidence point to significant imprints of ENSO on the spatial distribution of APO and the global APO budget, driven by anomalies in tropical Pacific air-sea O_2 exchange. Our finding are in agreement with results from a hindcast

simulation of the MITgcm that shows global impacts of ENSO-related variability in tropical air-sea O_2 fluxes (McKinley et al., 2003). Based on the extended APO inversion results, variability in APO fluxes of approximately ±34 Tmol yr^{-1} σ^{-1} due to ENSO modulation of air-sea O_2 fluxes should be taken into account in calculating global carbon sink budgets on interannual timescales. This estimate, however, does not take into account the diversity of ENSO phenomena, which may project on the F_{O2} response in the tropical Pacific. The eastern equatorial Pacific region, for instance, is likely to continue taking up O_2 during central Pacific or “Modoki" El Niño events (Ashok et al., 2007). We also did not address the potential impact of asymmetry between El Niño and La Niña phenomena (Rodgers et al., 2004) on the air-sea O_2 flux response. These potential sensitivities of APO responses to ENSO diversity might be best examined in an extended APO inversion and ocean model simulations that include recent ENSO events, such as the large 2015-2016 El Niño.

The fidelity of ocean model predictions of future O_2 changes depends on their ability to represent basic aspects of the oceanic O_2 cycle and its natural variability. Both CESM and IPSL show good agreement with the phase and sign of the APO response to ENSO estimated by the atmospheric inversion, whereas the GFDL response showed significant inconsistencies. The magnitude of the APO flux variability, however, is underestimated in all models globally and regionally by more than 50%. This underestimate is in agreement with a previous comparison of the atmospheric inversion APO results to an earlier generation ocean model (Rödenbeck et al., 2008). A recent study by Long et al. (2016) also shows significantly lower

interannual variability (>50%) in interior [O_2] in a coupled simulation of CESM when compared to available time series from ocean stations in the Subarctic and Subtropical North Pacific. These underestimates likely result from systemic model deficiencies in representing physical and biogeochemical processes and their interactions. For instance, inadequate representation of Equatorial Intermediate Currents in coarse resolution models (Dietze and Loeptien, 2013) or weak vertical mixing in the Subpolar North Pacific (e.g., in CESM; Moore et al., 2013) lead to weak ventilation of eastern tropical Pacific thermocline waters, driving significant low-O_2 biases. Deficiencies in representing organic matter remineralization profiles may also drive biases in the vertical gradient of [O_2] in the upper tropical Pacific (Moore et al., 2013), contributing to the large model underestimate in air-sea APO flux variability.

The weak sensitivity of the oceanic O_2 cycle to ENSO in these ocean simulations suggests climate models may also be underestimating the magnitude of oceanic O_2 loss due to anthropogenic warming. In fact, our reported underestimate of interannual variability is proportionally similar to an underestimate reported by a recent observational analysis of long-term O_2 trends, which shows global oceanic O_2 losses of about 1 Pmol (10^{15} mol) per decade since 1960, exceeding models estimates of 0-600 Tmol per decade (Schmidtko et al., 2017). Analysis of hydrographic measurements (Keeling and Garcia, 2002) also show a global O_2 outgassing to heating ratio of about 5 nmol (10^{-9}) per Joule (nmol J^{-1}), which are larger than our model estimates of about 3 nmol J^{-1}. These underestimates highlight the need for improved

process understanding of subsurface O_2 cycling and circulation on various spatial and time scales.

Still, the simulated O_2 flux response to ENSO provides useful information on the coupling of the oceanic O_2 cycle to climate perturbations in the tropical Pacific. Recent studies suggest the Walker Circulation may weaken due to anthropogenic warming (Vecchi et al., 2006). This may potentially shift the mean state of the tropical Pacific towards El Niño conditions (Yeh et al., 2009), though major uncertainties remain (Stevenson et al., 2012). Our results indicate a significant and regionally complex response of the upper ocean O_2 budget to El Niño conditions, whereby weakened ventilation leads to oceanic O_2 loss to the atmosphere. The relation between O_2 flux anomalies and changes in interior O_2 distribution and budgets, however, is not clear, and merits further investigation. Recent model studies invoke changes in O_2 consumption rates (Ito and Deutsch, 2013), as well as reduced ventilation of the OMZ by the shallow overturning cells and zonal jets (Duteil et al., 2014), to explain subsurface [O_2] changes associated with tropical climate variability. The dominance of these processes on subsurface [O_2] variability is likely to be localized and region-specific, given the zonally complex responses of F_{O2} and ΔO_2 shown herein. This regional complexity motivates a closer examination of the basin-wide impacts of tropical climate variability on interior ocean O_2 and their integrated effects on decadal timescales.

Acknowledgements

Chapter 2, in full, is a reprint of the material as it appears in Global Biogeochemical Cycle, 2017: Eddebbar, Y. A., M. C. Long, L. Resplandy, C. Rödenbeck, K. B. Rodgers, M. Manizza, and Keeling R.F. The dissertation author was the primary investigator and author of this paper.

References

Alexander, M., I. Blade, M. Newman, J. Lanzante, N. Lau, and J. Scott (2002), The atmospheric bridge: The influence of ENSO teleconnections on air-sea interaction over the global oceans, J. Clim., 15(16), 2205–2231, doi:10.1175/1520-0442(2002)0152.0.CO;2.

Andrews, O. D., N. L. Bindoff, P. R. Halloran, T. Ilyina, and C. Le Quéré (2013), Detecting an external influence on recent changes in oceanic oxygen using an optimal fingerprinting method, *Biogeosciences*, 10, 1799–1813, doi:10.5194/bg-10-1799-2013.

Ashok, K., S. K. Behera, S. A. Rao, H. Weng, and T. Yamagata (2007), El Niño Modoki and its possible teleconnection. *J. Geophys. Res.*, 112, C11007, doi:10.1029/2006JC003798.

Aumont, O., C. Ethé, A. Tagliabue, L. Bopp, and M. Gehlen (2015), PISCES-v2: an ocean biogeochemical model for carbon and ecosystem studies, *Geoscientific Model Development,* 8, 2465–2513, doi:10.5194/gmd-8-2465-2015.

Bacastow, R. B. (1976), Modulation of atmospheric carbon dioxide by the southern oscillation, *Nature*, 261, 116–118, doi:10.1038/261116a0.

Battle, M., S. M. Fletcher, M. L. Bender, R. F. Keeling, A. C. Manning, N. Gruber, P. P. Tans, M. B. Hendricks, D. T. Ho, C. Simonds, and R. Mika (2006), Atmospheric potential oxygen: new observations and their implications for some atmospheric and oceanic models, *Glob. Biogeochem. Cycles.*, 20, GB1010. doi: 10.1029/2005GB002534.

Behrenfeld, M. J., R. T. O'Malley, D. A. Siegel, C. R. McClain, J. L. Sarmiento, G. C. Feldman, A. J. Milligan, P. G. Falkowski, R. M. Letelier, and E. S. Boss (2006), Climate-driven trends in contemporary ocean productivity, *Nature*, 444, 752–755, doi:10.1038/nature05317.

Bjerknes, J. (1969), Atmospheric teleconnections from the equatorial Pacific, *Mon. Wea. Rev.,* 97, 163-172, doi:10.1175/1520-0493(1969)097.

Bopp, L., C. Le Quéré, M. Heimann, A. C. Manning, and P. Monfray (2002), Climate-induced oceanic oxygen fluxes: implications for the contemporary carbon budget, *Global Biogeochem. Cycles*, 16, 1022, doi:10.1029/2001GB001445.

Bopp, L., L. Resplandy, J. C. Orr, S. C. Doney, J. P. Dunne, M. Gehlen, P. Halloran, C. Heinze, T. Ilyina, R. Seferian, and J. Tjiputra (2013), Multiple stressors of ocean ecosystems in the 21st century: projections with CMIP5 models, *Biogeosciences*, 10, 6225–6245, doi:10.5194/bg-10-6225-2013.

Bourgeois, T., J. C. Orr, L. Resplandy, C. Ethé, M. Gehlen, L. Bopp (2016), Coastal-ocean uptake of anthropogenic carbon, *Biogeosciences,* 13, 4167–4185, doi:10.5194/bg-13-4167-2016.

Brodeau, L., B. Barnier, T. Penduff, A. M. Treguier, and S. Gulev (2009), An ERA40 based atmospheric forcing for global ocean circulation models, *Ocean Model.*, 31, 88–104, doi:10.1016/j.ocemod.2009.10.005.

Cabré, A., I. Marinov, R. Bernardello. and D. Bianchi (2015), Oxygen minimum zones in the tropical Pacific across CMIP5 models: mean state differences and climate change trends, *Biogeosciences,* 12, 5429–5454, doi:10.5194/bg-12-5429-2015.

Chavez, F. P., P. G. Strutton, G. E. Friederich, R. A. Feely, G. C. Feldman, D. G. Foley, and M. J. McPhaden (1999), Biological and chemical response of the equatorial Pacific Ocean to the 1997–98 El Niño, *Science*, 286, 2126–2131, doi:10.1126/ science.286.5447.2126.

Cocco, V., F. Joos, M. Steinacher, T. L. Frölicher, L. Bopp, J. Dunne, M. Gehlen, C. Heinze, J. Orr, A. Oschlies, and B. Schneider (2013), Oxygen and indicators of stress for marine life in multi-model global warming projections, *Biogeosciences,* 10, 1849-1868, doi:10.5194/bg-10-1849-2013.

Danabasoglu, G., and J. Marshall (2007), Effects of vertical variations of thickness diffusivity in an ocean general circulation model, *Ocean Modell.*, 18, 122–141, doi:10.1016/ j.ocemod.2007.03.006.

Danabasoglu, G, S. Bates, B. P. Briegleb, S. R. Jayne, M. Jochum, W. G. Large, S. Peacock, and S. G. Yeager (2012), The CCSM4 ocean component, *J. Climate*, 25, 1361–1389, doi:10.1175/JCLI-D-11-00091.1.

Deser, C., A. S. Phillips, R. A. Tomas, Y. Okumura, M. A. Alexander, A. Capotondi, J. D. Scott, Y.-O. Kwon, and M. Ohba (2012), ENSO and Pacific decadal

variability in Community Climate System Model Version 4, *J. Climate,* 25, 2622-2651, doi:10.1175/JCLI-D-11-00301.1.

Deutsch, C., H. Brix, T. Ito, H. Frenzel, and L. Thompson (2011), Climate-forced variability of ocean hypoxia, *Science,* 333, 336–339, doi:10.1126/science.1202422.

Dietze, H., and A. Oschlies (2005), On the correlation between air-sea heat flux and abiotically induced oxygen gas exchange in a circulation model of the North Atlantic, *J. Geophys. Res.*, 110, C09016, doi:10.1029/ 2004JC002453.

Dietze, H., and U. Loeptien (2013), Revisiting ‘‘nutrient trapping’’ in global coupled biogeochemical circulation models, *Global Biogeochem. Cycles*, 27, 265–284, doi:10.1002/ gbc.20029.

Doney, S. C., I. Lima, R. Feely, D. Glover, K. Lindsay, N. Mahowald, J. Moore, and R. Wanninkhof (2009), Mechanisms governing interannual variability in upper-ocean inorganic carbon system and air–sea CO2 fluxes: Physical climate and atmospheric dust, *Deep-Sea Res. II*, 56, 640–655, doi:10.1016/j.dsr2.2008.12.006.

Duchon, C. E. (1979), Lanczos filtering in one and two dimensions, *J. Appl. Meteorol.*, 18, 1016–1022, doi: 10.1175/1520-0450(1979)018.

Dunne, J. P., A. Gnanadesikan, J. L. Sarmiento, and R. D. Slater (2010), Technical description of the prototype version (v0) of Tracers of Phytoplankton with Allometric Zooplankton (TOPAZ) ocean biogeochemical model as used in the Princeton IFMIP model, *Biogeosciences,* 7, 1–22, doi:10.4195/bg-7-3593-2010.

Duteil, O., C. W. Böning, and A. Oschlies (2014), Variability in subtropical-tropical cells drives oxygen levels in the tropical Pacific Ocean, *Geophys. Res. Lett.,* 41, 8926–8934, doi:10.1002/2014GL061774.

Ebisuzaki, W. (1997), A method to estimate the statistical significance of a correlation when the data are serially correlated, *J. Climate*, 10, 2147–2153, doi:10.1175/1520-0442(1997)010.

Emerson S., Y. W. Watanabe, T. Ono, S. Mecking (2004), Temporal trends in apparent oxygen utilization in the upper pycnocline of the North Pacific: 1980–2000, *J. Oceanogr,* 60, 139–47, doi:10.1023/B:JOCE.0000038323.62130.a0.

Feely, R. A., R. Wanninkhof, T. Takahashi, and P. Tans (1999), Influence of El Niño on the equatorial Pacific contribution to atmospheric CO2 accumulation, *Nature,* 398, 597–601, doi:10.1038/ 19273.

Feely, R. A., J. Boutin, C. E. Cosca, Y. Dandonneau, J. Etcheto, H. Y. Inoue, M. Ishii, C. Le Quéré, D. J. Mackey, M. McPhaden, and N. Metzl (2002), Seasonal and interannual variability of CO_2 in the equatorial Pacific, *Deep Sea Res., Part II,* 49, 2443–2469, doi:10.1016/S0967-0645(02)00044-9.

Frölicher T. L., F. Joos, G. K. Plattner, M. Steinacher, S. C. Doney (2009), Natural variability and anthropogenic trends in oceanic oxygen in a coupled carbon cycle-climate model ensemble, *Glob. Biogeochem. Cycles,* 23, GB1003, doi:10.1029/2008GB003316

Garcia H. E., and L. I. Gordon (1992), Oxygen solubility in seawater: better fitting equations, *Limnol. Oceanogr.,* 37,1307–1312, doi:10.4319/lo.1992.37.6.1307.

Garcia, H. E., R. A. Locarnini, T. P. Boyer, J. I. Antonov, A. V. Mishonov, O. K. Baranova, M. M. Zweng, J. R. Reagan, and D. R. Johnson (2014), World Ocean Atlas 2013, in *Volume 3: Dissolved Oxygen, Apparent Oxygen Utilization, and Oxygen Saturation*, edited by S. Levitus and A. Mishonov, 27 pp., NOAA Atlas NESDIS 75, Silver Spring, Md.

Gent, P. R., and J. McWilliams (1990), Isopycnal mixing in ocean circulation models, *J. Phys. Oceanogr.*, 20, 150–155, doi:10.1175/1520-0485(1990)020.

Gent, P. R., G. Danabasoglu, L. J. Donner, M. M. Holland, E. C. Hunke, E.C., Jayne, D. M. Lawrence, R. B. Neale, P. J. Rasch, M. Vertenstein, and P. H. Worley (2011), The Community Climate System Model version 4, *J. Climate*, 24, 4973–4991, doi:10.1175/2011JCLI4083.1.

Griffies, S., A. Biastoch, C. Böning, F. Bryan, G. Danabasoglu, E. P. Chassignet, M. H. England, R. Gerdes, H. Haak, R. W. Hallberg, and W. Hazeleger (2009), Coordinated Ocean-Ice Reference Experiments (COREs), *Ocean Modell.,* 26, 1–46, doi:10.1016/j.ocemod.2008.08.007.

Griffies, S.M., M. Winton, B. Samuels, G. Danabasoglu, S. Yeager, S. Marsland, H. Drange, M. Bentsen (2012), Datasets and protocol for the CLIVAR WGOMD Coordinated Ocean sea-ice Reference Experiments (COREs). WCRP, Report No. 21/2012, USA.

Gruber, N., E. Gloor, S. M. Fan, and J. L. Sarmiento (2001), Air-sea flux of oxygen estimated from bulk data: Implications for the marine and atmospheric oxygen cycles, *Global Biogeochem. Cycles,* 15, 783–803, doi:10.1029/2000GB001302.

Hamme, R. C., and S. R. Emerson (2004), The solubility of neon, nitrogen and argon in distilled water and seawater, *Deep Sea Res. Part I,* 51, 1517–1528, doi:10.1016/j.dsr.2004.06.009.

Hamme, R. and R.F. Keeling (2008), Ocean ventilation as a driver of interannual variability in atmospheric potential oxygen, *Tellus,* 60B, doi:10.1111/j.1600-0889.2008.00376.x.

Heimann, M. and S. Korner (2003), The global atmospheric tracer model TM3, Technical Report 5. Max Planck Institute for Biogeochemistry, Jena, Germany.

Helm, K. P., N. L. Bindoff, and J. A. Church (2011), Observed decreases in oxygen content of the global ocean, *Geophys. Res. Lett.*, 38, L23602, doi:10.1029/2011GL049513.

Hunke, E., and W. Lipscomb (2008), CICE: The Los Alamos sea ice model documentation and software user's manual, version 4.0. Los Alamos National Laboratory Tech. Rep. LA-CC-06-012, 76 pp.

Ito, T., and C. Deutsch (2010), A conceptual model for the temporal spectrum of oceanic oxygen variability, *Geophy. Res. Lett.*, 37, L03601, doi:10.1029/2009GL041595.

Ito, T., and C. Deutsch (2013), Variability of the oxygen minimum zone in the tropical North Pacific during the late twentieth century, *Global Biogeochem. Cycles*, 27, 1119–1128, doi:10.1002/2013GB004567.

Jin, X., R. G. Najjar, F. Louanchi, and S. C. Doney (2007), A modeling study of the seasonal oxygen budget of the global ocean, *J. Geophys. Res.,* 112, C05017, doi:10.1029/2006JC003731.

Kalnay, E., M. Kanamitsu, R. Kistler, W. Collins, D. Deaven, L. Gandin, M. Iredell, S. Saha, G. White, J. Woollen, and Y. Zhu (1996), The NCEP/NCAR 40-Year Re-analysis Project, *Bull. Amer. Meteor. Soc.*, 77, 437–471, doi:10.1175/1520-0477(1996)077.

Keeling, C. D. and R. Revelle (1985), Effects of El-Niño Southern Oscillation on the atmospheric content of carbon-dioxide, *Meteoritics,* 20, 437–450.

Keeling, R. F., R. P. Najjar, M. L. Bender, and P. P. Tans (1993): What atmospheric oxygen measurements can tell us about the global carbon cycle, *Global Biogeochem. Cycles*, 7, 37–67, doi:10.1029/92GB02733.

Keeling, R. F., S.C. Piper, and M. Heimann (1996), Global and hemispheric CO_2 sinks deduced from changes in atmospheric O_2 concentration, *Nature*, 381, 218–221, doi:10.1038/381218a0.

Keeling, R.F., B. B. Stephens, R. G. Najjar, S. C. Doney, D. Archer, and M. Heimann (1998), Seasonal variations in the atmospheric O2/N2 ratio in relation to the kinetics of air-sea gas exchange, *Global Biogeochem. Cycles,* 12(1), 141–163, doi:10.1029/97GB02339.

Keeling, R. F. and J. P. Severinghaus (2000), Atmospheric oxygen and the carbon cycle, *The Carbon Cycle*, Edited by T. M. L. Wigley, and D. S. Schimel, pp. 134–140, Cambridge Univ. Press, Boston, Mass, USA.

Keeling, R. F. and H. Garcia (2002), The change in oceanic O2 inventory associated with recent global warming, *Proc. Natl. Acad. Sci. USA,* 99, 7848–7853, doi:10.1073/pnas.122154899.

Keeling, R. F., A. Körtzinger, and N. Gruber (2010), Ocean deoxygenation in a warming world, *Annu. Rev. Marin. Sci.*, 2, 199–229, doi:10.1146/annurev.marine.010908.163855.

Keeling, R., and A. Manning (2014), Studies of Recent Changes in Atmospheric O_2 Content, *Treatise on Geochemistry*, 2nd ed., H. D. Holland and K. K. Turekian, Ed., Elsevier, 385–404, doi:10.1016/B978-0-08-095975-7.00420-4.

Large, W. G., and S. Yeager (2009), The global climatology of an interannually varying air–sea flux data set, *Climate Dyn.*, 33, 341–364, doi:10.1007/s00382-008-0441-3.

Large, W. G., J. C. McWilliams, and S. C. Doney (1994), Oceanic vertical mixing: A review and a model with a nonlocal boundary layer parameterization, *Rev. Geophys.*, 32, 363–403, doi:10.1029/ 94RG01872.

Long, M. C., K. Lindsay, S. Peacock, J. K. Moore, and S. C. Doney (2013), Twentieth-century oceanic carbon uptake and storage in CESM1 (BGC), *J. Climate*, 26, 6775–6800, doi:10.1175/JCLI-D-12-00184.1.

Long, M. C., C. A. Deutsch, and T. Ito (2016), Finding forced trends in oceanic oxygen, *Global Biogeochem. Cycles*, 30, 10.1002/2015GB005310.

Madec, G. (2008), NEMO Ocean Engine. Note du Pole de modélisation de l'Institut Pierre-Simon Laplace, vol. 27, pp. 1–217, Institut Pierre-Simon Laplace (IPSL), France.

Manning, A. C. (2001), Temporal Variability of Atmospheric Oxygen from Both Continuous Measurements and a Flask Sampling Network: Tools for Studying the Global Carbon Cycle, Ph.D. thesis, University of California, San Diego, La Jolla, California, U.S.A.

Manning, A. C., and R. F. Keeling (2006), Global oceanic and land biotic carbon sinks from the Scripps atmospheric oxygen flask sampling network, *Tellus, Ser. B,* 58, 95–116, doi:10.1111/j.1600-0889.2006.00175.x.

McKinley, G. A., M. J. Follows, J. Marshall, and S. M. Fan (2003), Interannual variability of air-sea O_2 fluxes and the determination of CO_2 sinks using atmospheric O_2/N_2, Geophys. Res. Lett., 30(3), 1101, doi:10.1029/ 2002GL016044.

McKinley, G. A., M. J. Follows, and J. Marshall (2004), Mechanisms of air-sea CO_2 flux variability in the equatorial Pacific and the North Atlantic, *Global Biogeochem. Cycles,* 18, GB2011, doi:10.1029/ 2003GB002179.

McPhaden, M. J., A. J. Busalacchi, R. Cheney, J. R. Donguy, K. S. Gage, D. Halpern, M. Ji, P. Julian, G. Meyers, G. T. Mitchum, and P. P. Niiler (1998), The Tropical ocean-global atmosphere observing system: A decade of progress, J. Geophys. Res., 103, 14169–14240, doi:10.1029/97JC02906.

Moore, J. K., S. C. Doney, and K. Lindsay (2004), Upper ocean ecosystem dynamics and iron cycling in a global three-dimensional model, *Global Biogeochem. Cycles*, 18, GB4028, doi:10.1029/2004GB002220.

Moore, J. K., K. Lindsay, S. C. Doney, M. C. Long, and K. Misumi (2013), Marine ecosystem dynamics and biogeochemical cycling in the Community Earth System Model [CESM1(BGC)]: Comparison of the 1990s with the 2090s under the RCP 4.5 and RCP 8.5 scenarios, *J. Climate*, 26, 9291–9312, doi:10.1175/jcli-d-12-00566.1.

Najjar, R. G. and R. F. Keeling (2000), Mean annual cycle of the air-sea oxygen flux: a global view, Global Biogeochem. Cycles, 14, 573–584, doi:10.1029/1999GB900086.

Nevison C., M. Manizza, R. F. Keeling, M. Kahru, L. Bopp, J. Dunne, J. Tiputra, T. Ilyina, and B. G. Mitchell (2015), Evaluating the ocean biogeochemical components of Earth system models using atmospheric potential oxygen and ocean color data, *Biogeosciences,* 12, 193-208. doi:10.5194/bg-12-193-2015.

Park, J. Y., J. S. Kug, J. Park, S. W. Yeh, and C. J. Jang (2011), Variability of chlorophyll associated with El Niño-Southern Oscillation and its possible biological feedback in the Equatorial Pacific, *J. Geophys. Res.*, 116, C10001, doi:10.1029/2011JC007056.

Radenac, H., Y. Dandonneau, and B. Blanke (2005), Displacements and transformations of nitrate-rich and nitrate-poor water masses in the tropical

Pacific during the 1997 El Niño, *Ocean Dynamics*, 55, 34–46, doi:10.1007/s10236-005-0111-5.

Resplandy, L., R. Séférian, and L. Bopp (2014), Natural variability of CO2 and O2 fluxes: what can we learn from centuries-long climate models simulations?, *J. Geophys. Res.-Oceans*, 120, 384– 404, doi:10.1002/2014JC010463.

Rödenbeck, C., C. LeQuéré, M. Heimann, and R.F. Keeling (2008), Interannual variability in oceanic biogeochemical processes inferred by inversion of atmospheric O2/N2 and CO2 data, *Tellus B,* 60, 685–705, doi:10.1111/j.1600-0889.2008.00375.x.

Rodgers, K. B., P. Friederichs, and M. Latif (2004), Tropical Pacific decadal variability and its relation to decadal modulations of ENSO, *Journal of Climate*, 17, 3761–3774, doi:10.1175/1520-0442(2004)017.

Rodgers, K. B., R. M. Key, A. Gnanadesikan, J. L. Sarmiento, O. Aumont, L. Bopp, S. C. Doney, J. P. Dunne, D. M. Glover, A. Ishida, and M. Ishii (2009), Using altimetry to help explain patchy changes in hydrographic carbon measurements, *J. Geophys. Res.*, 114, C09013, doi:10.1029/2008JC005183.

Rodgers, K. B., J. Lin, and T. L. Frölicher (2015), Emergence of multiple ocean ecosystem drivers in a large ensemble suite with an earthsystem model, *Biogeosciences,* 12(11), 3301–3320, doi:10.5194/bg-12-3301-2015.

Roemmich, D. and J. Gilson (2011), The global ocean imprint of ENSO, *Geophys. Res. Lett,,* 38, L13606, doi:10.1029/2011GL047992.

Sarmiento J.L., T.C. Hughes, R.J. Stouffer, and S. Manabe (1998), Simulated response of the ocean carbon cycle to anthropogenic climate warming, *Nature,* 393, 245–249, doi:10.1038/30455.

Schmidtko, S., L. Stramma, and M. Visbeck (2017), Decline in global oceanic oxygen content during the past five decades, *Nature*, 542, 335-339, doi:10.1038/nature21399.

Severinghaus, J. P. (1995), Studies of the Terrestrial O2 and Carbon Cycles in Sand Dune Gases and in Biosphere 2, Ph.D. thesis, Columbia University, New York, U.S.A.

Smith, R. D., P. Jones, B. Briegleb, F. Bryan, G. Danabasoglu, J. Dennis, J. Dukowicz, C. Eden, B. Fox-Kemper, P. Gent, and M. Hecht (2010), The Parallel Ocean Program (POP) reference manual, Los Alamos National Laboratory Tech. Rep. LAUR-10-01853, 140 pp.

Stephens, B. B., R. F. Keeling, M. Heimann, K. D. Six, R. Murnane, and K. Caldeira (1998), Testing global ocean carbon cycle models using measurements of atmospheric O2 and CO2 concentration. *Glob. Biogeochem. Cycles*, 12, 213–230, doi:10.1029/97GB03500.

Stephens, B. B. (1999), Field-based atmospheric oxygen measurements and the ocean carbon cycle, Ph.D. Thesis, University of California, San Diego, California, U.S.A.

Stephens, B. B., R. F. Keeling, and W. Paplawsky (2003), Shipboard measurements of atmospheric oxygen using a vacuum-ultraviolet absorption technique, *Tellus,* 55B, 857–878, doi:10.3402/tellusb.v55i4.16386.

Stevenson, S., B. Fox-Kemper, M. Jochum, R. Neale, C. Deser, and G. Meehl (2012), Will there be a significant change to El Niño in the twenty-first century?, *J. Climate*, 25, 2129–2145, doi:10.1175/JCLI-D-11-00252.1.

Stramma L., G.C. Johnson, J. Sprintall, V. Mohrholz (2008), Expanding oxygen-minimum zones in the tropical oceans, *Science*, 320, 655–658, doi:10.1126/science.1153847.

Stramma, L., A. Oschlies, and S. Schmidtko (2012), Mismatch between observed and modeled trends in dissolved upper-ocean oxygen over the last 50 yr, *Biogeosciences*, 9, 4045–4057, doi:10.5194/bg-9-4045-2012.

Takahashi, T., R. Feely, R. Weiss, R. Wanninkhof, D. Chipman, S. Sutherland, and T. Takahashi (1997), Global air–sea flux of CO2: An estimate based on measurements of sea–air pCO2 difference, *Proc. Natl. Acad. Sci. USA*, 94, 8292–8299.

Tohjima, Y., Y. Terao, H. Mukai, T. Machida, Y. Nojiri, and S. Maksyutov (2015), ENSO-related variability in latitudinal distribution of annual mean atmospheric potential oxygen (APO) in the equatorial Western Pacific, *Tellus B.*, 67, 25869, doi:10.3402/tellusb.v67.25869.

Trenberth, K. E. (1997), The definition of El Niño, *Bull. Amer. Meteor. Soc.*, 78, 2771–2777, doi:10.1175/1520-0477(1997)078.

Trenberth, K. E., J.M. Caron, D. P. Stepaniak, and S. Worley (2002), The evolution of ENSO and global atmospheric surface temperatures, J. Geophys. Res., 107, D8, AAC 5-1-AAC 5-17, doi:10.1029/2000JD000298.

Vecchi, G. A., and B. J. Soden (2007), Global warming and the weakening of the tropical circulation, *J. Climate*, 20, 4316–4340, doi: 10.1175/JCLI4258.1.JCLI3631.1.

Wang, W. and M. J. McPhaden (2001), Surface layer heat balance in the equatorial Pacific Ocean during the 1997-98 El Niño and the 1998-99 La Niña, *J. Climate,* 14, 3393–3407*,* doi:10.1175/1520-0442(2001)014.

Wanninkhof, R. (1992), Relationship between wind speed and gas exchange over the ocean, *J. Geophys. Res.*, 97 (C5), 7373– 7382, doi: 10.1029/92JC00188.

Wanninkhof, R., R.A. Feely, D.K. Atwood, G.A. Berberian, W.D. Wilson, P.P. Murphy, and M.F. Lamb (1995), Seasonal and lateral variations in carbon chemistry of surface water in the eastern equatorial Pacific during 1992, *Deep-Sea Research II,* 42 (2–3), 387–410, doi:10.1016/0967-0645(95)00016-J.

Weiss, R. F. (1974), Carbon dioxide in seawater: The solubility of an ideal gas, *Mar. Chem.*, 2, 203–215, doi:10.1016/ 0304-4203(74)90015-2.

Williams, R.G. and M.J. Follows (2011), *Ocean Dynamics and the Carbon Cycle,* Cambridge University Press, Pp:150-151.

Winguth, A. M. E., M. Heimann, K. D. Kurz, E. Maier-Reimer, U. Milolajewicz, and J. Segschneider (1994), El Niño Southern Oscillation related fluctuations in the marine carbon cycle, *Global Biogeochem. Cycles*, 8(1), 39–93, doi: 10.1029/93GB03134.

Yeh, S. W., J. S. Kug, B. Dewitte, M. H. Kwon, B. P. Kirtman, and F. F. Jin (2009), El Niño in a changing climate, *Nature*, 461, 511–514, doi:10.1038/nature08316.

Zwiers, F. W., and H. von Storch (1995), Taking serial correlation into account in tests of the mean, *J. Climate*, 8, 336–351, doi:10.1175/1520-0442(1995)008.

CHAPTER 3: AN EL NIÑO-LIKE PHYSICAL AND BIOGEOCHEMICAL OCEAN RESPONSE TO TROPICAL VOLCANIC ERUPTIONS

Abstract

Volcanic eruptions are expected to have a major influence on ocean physics and biogeochemistry. The magnitude, spatial patterns, and mechanisms of volcanic impacts on the oceans, however, remain poorly understood due to the confounding effects of internal variability and limited observations. Here, the oceanic response to recent major tropical eruptions is evaluated in the Large Ensemble experiments of the fully coupled Earth system models of CESM and GFDL. Substantial and spatially complex ocean heat loss and oxygen and carbon uptake immediately follow the Agung, El Chichon and Pinatubo eruptions. These volcanic signals are relatively consistent across eruptions and models, and are in general agreement with available observations. The oceanic response to tropical eruptions is characterized by intense surface cooling over the subtropics and northern high latitudes, but is also accompanied by El Niño-like surface warming in the eastern and central tropical Pacific initiated by climatological upwelling of warm subsurface anomalies in the east. This subsurface warming is driven by the thermocline deepening effects of equatorial downwelling Kelvin waves that are remotely forced by persistent westerly wind anomalies over the western Pacific. These wind anomalies, in turn, are associated with intense cooling and suppressed convection over the Maritime Continent, and suggest a more prominent role for atmospheric circulation rather than an ocean thermostat effect in initiating the

ENSO response. This El Niño response drives ocean heat loss that persists beyond the atmospheric lifetime of stratospheric aerosols through enhanced cloud albedo, and causes most of the global carbon uptake through reduction of vertical transport of dissolved inorganic carbon (DIC) to the surface in the tropical Pacific. These El Niño-like changes in the source and intensity of equatorial upwelling lead to anomalous outgassing of O_2, but are largely counteracted by intensified ventilation at higher latitudes that drive the global oceanic uptake of O_2. Volcanic eruptions thus induce a complex ocean response that is highly relevant to the attribution of recently observed trends in the ocean, and may serve as a powerful analog for the unintended consequences of geoengineering in the ocean.

1. Introduction

In the absence of global scale geoengineering experiments, explosive volcanic eruptions represent the closest analogs to radiative management proposals. Following an eruption, the ejection of sulfates into the stratosphere and their consequent aerosol scattering of shortwave radiation increase planetary albedo, driving significant cooling of the troposphere (Pollack et al., 1976; Dutton and Christy 1992; Robock 2000). Concurrently, sulfates also absorb near-infrared solar and outgoing long-wave radiation, which warms the lower stratosphere (Stenchikov et al., 1998). These radiative perturbations have profound and long-lasting impacts on the climate system, particularly in the ocean where volcanic signals are expected to persist well beyond the e-folding lifetime of aerosols (Gleckler et al., 2006; Stenchikov et al., 2009). Examining the oceanic imprints of recent eruptions may thus hold valuable insights

for the prediction of geoengineering impacts on the oceans and the interpretation of recently observed trends in the climate system.

The ocean is expected to respond to volcanic eruptions in two fundamental ways. First, an immediate thermodynamic response to aerosol scattering of solar radiation is expected to lead to sea surface temperature (SST) cooling (Rampino and Self 1982), reduced ocean heat content (Delworth et al., 2005; Stenchikov et al., 2009), and decreased thermosteric sea level (Gleckler et al., 2006). It remains unclear, however, where heat loss occurs regionally and how feedbacks in the coupled ocean-atmosphere system amplify or dampen the net change in air-sea heat flux.

Second, a dynamical ocean response is expected due to volcanic perturbations of temperature gradients, influencing ocean circulation and projecting onto modes of natural climate variability (Zanchettin et al., 2012). Paleoproxies, for instance, indicate El Niño conditions follow major eruptions (Adams et al., 2003). To explain this link, Mann et al. (2005) evoke the "ocean dynamical thermostat" mechanism (Clement et al., 1996): volcanic radiative cooling at the sea surface is buffered by the climatological upwelling of unperturbed thermocline waters and divergence in the eastern equatorial Pacific while the western Pacific cools uninhibitedly; the subsequent reduction in zonal SST gradient initiates Bjerknes feedbacks wherein weakened easterlies yield decreased upwelling and the full development of El Niño (Emile-Geay et al., 2008). Ding et al. (2014), however, find no links between volcanoes and ENSO across CMIP5 models, while some find La Niña conditions emerge in certain models (McGregor and Timmermann 2011; Zanchettin et al., 2012),

exposing key differences across models and observations. Recent progress has illuminated a complex volcanic modulation of tropical climate that depends on the initial state of ENSO prior to eruption (Ohba et al., 2013; Predybaylo et al., 2017; Khodri et al., 2017) as well as on the season and location of the eruption (Stevenson et al., 2017; Liu et al., 2017). A clear temporal evolution or mechanistic understanding of how volcanic eruptions affect the coupled ocean-atmosphere system, however, remain obscured by the freely evolving nature of ENSO regardless of external forcing.

These volcanoes-induced thermodynamic and dynamical changes, in turn, impact ocean biogeochemical cycles, as changes in temperature-dependent gas solubility and circulation alter the air-sea fluxes and subsurface distribution of oxygen (O_2) and carbon. Atmospheric CO_2 increase, for instance, "stalled" in the years following the June 1991 eruption of Pinatubo (Sarmiento 1993), with ambiguous roles for terrestrial vs. ocean carbon uptake (Frölicher et al., 2011, 2013; Segschneider et al., 2013). Oceanic O_2 loss due to anthropogenic warming is superimposed on significant interannual to decadal variability (Schmidtko et al., 2017; Ito et al., 2017) challenging the attribution and detection of anthropogenic forced trends (Long et al., 2016). The role of volcanic eruptions in driving changes in air-sea O_2 exchange and interior [O_2] variability remain largely unexplored (Frölicher et al., 2009). Isolating these volcanic effects is thus critical to the detection and attribution of anthropogenic impacts in the ocean, e.g., warming, deoxygenation, and acidification (Bopp et al., 2013), and is highly relevant to discussions of decadal variability in the oceanic heat and carbon sinks in recent decades (Balmaseda et al., 2013; Landschützer et al., 2015).

The magnitude and mechanisms driving the physical and biogeochemical ocean response to volcanoes, however, remain muddied by the confounding effects of internal variability and the lack of global continuous ocean observations spanning major eruptions. In models, discerning the volcanically-forced ocean response in the presence of intrinsic climate variability has been hindered by the limited number of ensemble members in past studies (Frölicher et al., 2009, 2013; Ding et al., 2014). Multi-model ensemble studies (e.g., CMIP5 archive), despite their large number of ensemble members, combine uncertainty due to model structure with internal variability, thereby limiting inferences regarding "forced" signals (Kay et al., 2014; McKinley et al., 2016; Long et al., 2016).

In this study, we focus on a Large Ensemble (LE) suite from a single climate model, the Community Earth System Model LE (CESM LE), to effectively isolate the volcanic forced component, as described in Section 2. We evaluate model differences by comparing results from a similar LE experiment using the Geophysical Fluid Dynamics Laboratory model (GFDL LE). Specifically, we examine the recent major tropical eruptions of Agung, El Chichon, and Pinatubo (table 1), given their relatively similar region (tropics) and time of year (spring-summer) of eruption, and their relevance to observed ocean trends in recent decades. In section 3, we evaluate the global mean and spatial patterns of SST, heat, O_2, and CO_2 air-sea exchanges and budgets as indicators of the ocean's physical and biogeochemical state following tropical eruptions. Due to microbial respiration at depth, dissolved oxygen [O_2] and dissolved inorganic carbon (DIC) show pronounced vertical gradients and their

variability tends to be negatively correlated. Assessing biogeochemical and physical variables in concert thus offers a comprehensive and unique view on governing ocean processes that may not be evident from temperature alone (e.g., changes in ventilation rates). In Section 4, we evaluate similarities and differences across models and observations, and examine driving mechanisms in Section 5, focusing on Pinatubo, the largest and most well observed eruption of the last 100 years. We conclude with a summary and discussion of our results.

Table 3.1. Description of recent major volcanic eruptions examined in the CESM and GFDL LE experiment. Volcanic intensities are based on the Ice-Core Volcanic Intensity Index of Gao et al. (2008). We also show the Volcanic Explosivity Index (VEI) of Simkin and Siebert (1994), and the Dust Veil Index (DVI) of Lamb (1983), as updated by Robock and Free (1995).

Volcanic Eruption	**Date**	**Location**	**Intensity (Pg)**	**VEI**	**DVI**
Agung, Indonesia	March 1963	8°S 115°E	17	4	800
El Chichon, Mexico	April 1982	17°N 93°W	14	5	800
Pinatubo, Philippines	June 1991	15°N 120°E	30	6	1000

2. Methods

a. The Large Ensemble Experiment

The LE framework brought significant and novel advances in the area of attribution and detection of anthropogenic forced trends in the presence of natural variability (Kay et al., 2014; McKinley et al., 2016; Long et al., 2016). Here, we use the LE framework as a modeling platform to examine the climate response to the

external forcing induced by volcanic eruptions. In the LE experiment, a large number of ensemble members from the same Earth system model were forced with identical external forcing from historical anthropogenic and volcanic emissions, but were initialized with unique small perturbations to the initial conditions. Modes of internal variability are thus effectively randomized across the ensemble within about a decade and averaging across a sufficiently large number of ensemble members isolates the externally forced response due to eruptions and anthropogenic greenhouse gas emissions (Kay et al., 2014).

The CESM LE configuration is run at the 1ºx1º nominal horizontal resolution of CESM version 1, which couples the Community Atmosphere Model version 5 (Hurrell et al., 2013) to the Parallel Ocean Program version 2 (Danabasoglu et al., 2012) and the Los Alamos Sea Ice Model version 4 (Hunke et al., 2008). Ocean biogeochemistry is also coupled in the ocean model and simulated using the Biogeochemical Elemental Cycling model (Moore et al., 2013). We evaluate 41 ensemble runs for physical variables, and 30 runs for biogeochemical fields for the period of 1950-2005. Ensemble runs were initialized from a 600-year spin-up model solution and were forced with identical prescribed CO_2 mixing ratio based on observations. Initial conditions for each ensemble member were perturbed with a round-off level perturbation (10^{-14} K) to atmospheric surface temperatures, which randomizes modes of variability within a decade across ensembles. The LE mean is then evaluated for volcanic and anthropogenic forcing components. Volcanic radiative forcing is incorporated in the CESM LE using the forcing dataset of Ammann et al.,

(2003). Here, stratospheric sulfate aerosol loading, characterized herein using aerosol optical depth (AOD) at 0.5 micron (500 nm), is based on total sulfates ejected from each eruption and the resulting sulfate aerosol temporal evolution and latitudinal distribution due to the seasonally dependent stratospheric transport. A more detailed description of the CESM LE experiment and model configuration and validation may be found in Kay et al. (2014) and Long et al. (2016).

For the GFDL model, we analyze 30 ensemble members for the period of 1950-2005 for both physical and biogeochemical fields. Here, ensemble runs 2-30 are initialized with slightly different initial conditions by using snapshots from days 1-29 from ensemble run 1. The GFDL-LE configuration was based on the GFDL-ESM2M (Dunne et al., 2012, 2013) in its 1ºx1º nominal resolution, where the atmospheric model AM2 (Anderson et al., 2004) is coupled to the ocean component MOM4p1 (Griffies et al., 2009) and a model of ocean biogeochemistry, Tracers of Ocean Phytoplankton and Allometric Zooplankton version 2 (Dunne et al., 2010). The revised aerosol loading product of Sato et al. (1993) is used in the GFDL LE, which results in a lower AOD than obtained from Ammann et al. (2003). Further description of the GFDL LE configuration can be found in Rodgers et al. (2015). The different model components and volcanic forcing used in GFDL vs. CESM LE allow us to evaluate the impacts of model structure and choice of volcanic forcing on our results.

To isolate the effects of volcanic eruptions on the carbon cycle, we use a "natural" or "preindustrial" CO_2 tracer, which is exposed to a constant 284.7 ppm atmospheric concentration. We also briefly evaluate volcanic effects on contemporary

carbon (which is the sum of natural and anthropogenic components) in our comparison of CESM and GFDL, but focus our mechanistic and spatial analysis on the natural carbon cycle for clarity. Monthly anomalies are derived for all series by removing the long-term monthly mean. To characterize spatial anomalies following eruptions, we show annual mean anomalies in the years following eruption, referring to the 12 months following the eruption date as year 0 (months 1-12), and subsequent years as year 1 (months 13-24), and year 2 (months 25-36). Similarly, the seasonal evolution of atmospheric and oceanic conditions are presented as seasonally averaged anomalies following eruption, with SON(0), for instance, referring to the September-October-November directly following the eruption, and SON(1) referring to the subsequent year (year 1). To highlight the volcanic signal in the spatial analysis and mechanism section, the long-term linear trend due to anthropogenic warming computed from the LE mean is removed and anomalies are computed relative to the 5 years prior to eruption. Statistical significance of volcanic anomalies in the LE mean is evaluated across the ensemble members at the 95% confidence level using a two-tailed Student's t-test. Throughout the paper, a positive anomaly in the air-sea flux of heat, O_2 or CO_2 indicate anomalous flux out of the ocean, while a negative flux denotes ocean uptake.

b. Observations

Due to limited global continuous ocean observations prior to the 1990's, we focus our model-to-observations comparison to the Pinatubo eruption. Specifically, we evaluate SST anomalies from the NOAA Reynolds product (Reynolds et al., 2002), and mixed layer depths from the Global Ocean Data Assimilation System (GODAS)

reanalysis product (Behringer and Xue 2004). We compare the simulated net air-sea heat flux to the Liu et al. (2015) product, which employs a mass-adjusted energy divergence method, satellite measurements of top-of-atmosphere energy fluxes, and energy transport and atmospheric energy tendencies from an atmospheric reanalysis product (Allan et al., 2014).

We compare O_2 fluxes to estimates of air-sea O_2 exchange based on time series of Atmospheric Potential Oxygen ($APO = O_2 + 1.1*CO_2$), an atmospheric tracer based on measurements of atmospheric O_2 and CO_2 (Stephens et al., 1998), where 1.1 is the biospheric $-O_2$:CO_2 molar exchange ratio (Severinghaus 1995). Due to tight coupling of terrestrial O_2 and CO_2 exchange, APO is insensitive to terrestrial perturbations. On interannual timescales, APO is dominated by variability in air-sea O_2 fluxes, and thus constrains the oceanic O_2 response to volcanic eruptions. The globally integrated air-sea flux of APO (F_{APO}) can be inferred from the observed global mean APO as: $F_{\mathrm{APO}} = M_{ATM}\, X_{\mathrm{O}_2} \frac{d\mathrm{APO}_{\mathrm{GLB}}}{dt}$, where M_{ATM} is the number of moles in the atmosphere (1.8×10^{20} mol) and X_{O2} is the atmospheric mixing ratio of O_2 (0.2095), and APO_{GLB} is the mean APO anomaly calculated from La Jolla and Cape Grim stations where observations have been maintained prior to the Pinatubo eruption (Keeling and Manning 2014). Owing to fast atmospheric mixing on interannual timescales, we find these two stations to be adequate to resolve global air-sea APO flux changes. We compare the simulated carbon flux response to an observational product based on the Surface Ocean Carbon Atlas (SOCAT) dataset and a mixed layer scheme (Rödenbeck et al., 2014). To put the observed APO and CO_2 fluxes within the context of observed

natural variability, we also evaluate fluxes from a hindcast simulation of CESM (Long et al., 2013), which simulates the expected ocean biogeochemical response to observed atmospheric conditions.

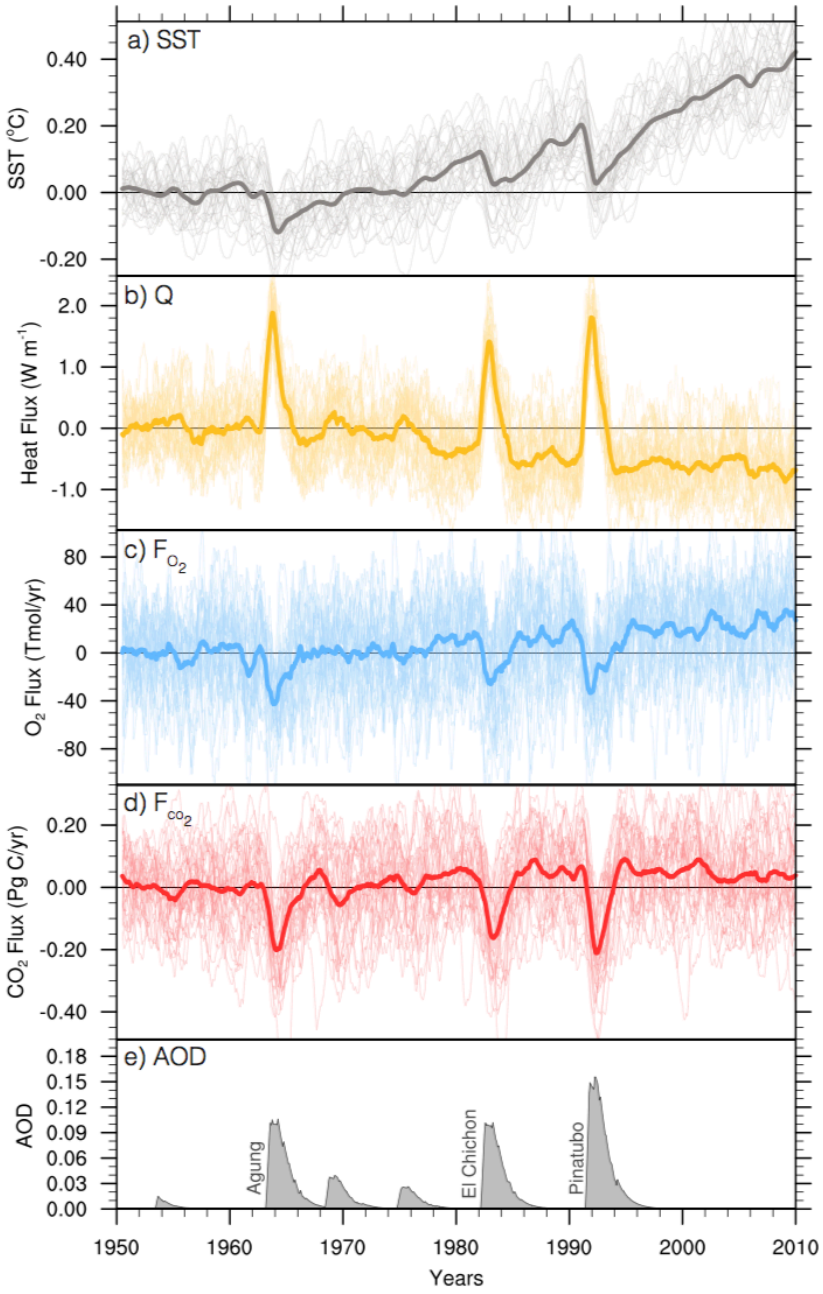

Figure 3.1. CESM LE anomalies in a) global mean SST, b) globally integrated air-sea heat flux (Q), c) O_2 flux (F_{O2}), c) natural (i.e. preindustrial) CO_2 flux (F_{CO2}), and d) stratospheric

(Figure 3.1 continued) Aerosol Optical Depth (AOD) at 500nm. Thin lines denote individual ensemble runs, while thick lines represent the LE mean. Time series are seasonally detrended (i.e. seasonal cycle is removed) and smoothed with a 12-month running mean, and anomalies are calculated from 1950-1959 mean. Positive flux denotes flux out of the ocean.

3. Oceanic Imprints of Tropical Eruptions

a. Global Mean Response

Figure 3.1 illustrates the CESM response in global mean SST and air-sea heat flux, and the globally integrated O_2 and CO_2 fluxes following the eruptions of Agung, El Chichon, and Pinatubo. The LE mean (bold lines) isolates clearly the effects of volcanic and anthropogenic forcing from internal noise, which dominates interannual-to-decadal variability in individual ensemble members (thin lines). The multi-decadal rise in global mean SST due to greenhouse gas forcing (~0.4 ºC) from 1950 to 2010 is punctuated by sharp declines of about 0.1-0.2 ºC in the year following the eruption. Similarly, the long-term oceanic uptake of heat is disrupted by massive ocean heat loss events of about 2 W m^{-2} within 6-9 months following eruptions. Substantial oceanic uptake of O_2 up to 60 Tmol.yr^{-1} also follow volcanic events, acting in the opposite sense of the long-term anthropogenic outgassing of O_2 due to enhanced stratification and reduced gas solubility. "Natural" CO_2 uptake of up to 0.3 Pg C yr^{-1} following eruptions is evident as well, opposing a weak long-term outgassing trend due to anthropogenic warming.

The global ocean response for each variable is relatively consistent across eruptions and scales with eruption magnitude, with Pinatubo showing the largest response across all variables. Key differences, however, do arise in the timing and signal-to-noise ratio of physical and biogeochemical ocean anomalies. Whereas the

volcanic heat flux anomaly emerges clearly from internal noise, the O_2 flux response is well within the 2σ ensemble members spread due to internal variability, likely due to regional cancellation effects or greater O_2 sensitivity to unforced variability. The recovery periods also vary between variables, with faster recovery in heat and natural CO_2 fluxes (~ 2 years) compared to a slower relaxation in SST and O_2 (4-6 years) that induces decadal-like variability.

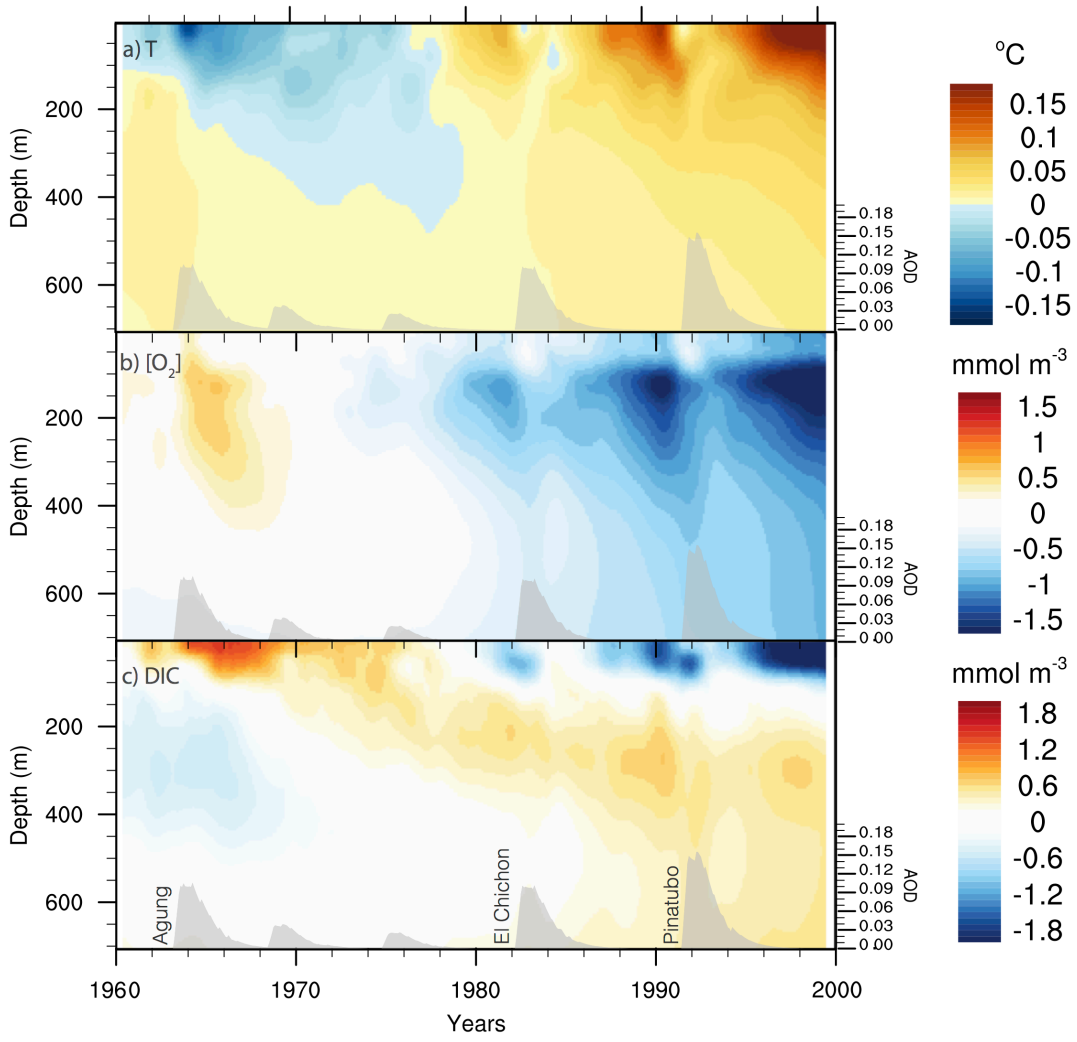

Figure 3.2. Globally averaged vertical profile of CESM LE mean anomalies in a) temperature, b) $[O_2]$, and c) DIC. AOD (right axis) is also shown within each panel. Anomalies are calculated from the 1950-1959 mean and are smoothed with a 12-month running mean.

These air-sea flux anomalies have profound and persistent integrated effects on vertical profiles of heat, [O_2], and DIC globally (Figure 3.2). The long-term ocean impacts of anthropogenic greenhouse gas forcing are evident through gradual heat uptake and oxygen and DIC loss in the upper ocean, and are punctuated by volcanic events. These volcanic impacts are particularly visible following the Agung eruption, when the anthropogenic signal is largely absent. Substantial cooling occurs after each event in the upper 100 m, propagating down to 500 m in depth through advective and diffusive mixing processes, and persists for more than a decade post-eruption. [O_2] anomalies show maxima below 100 m in depth, suggesting a biological or dynamical response, and persist for 6-7 years post eruption. Figure 3.2 shows that the gradual penetration of anthropogenic heat, and [O_2] and natural DIC loss is immediately, though only temporarily, interrupted by the El Chichon and Pinatubo eruptions, acting to significantly delay the advance of ocean warming, deoxygenation and natural carbon loss in the upper ocean over the second half of the 20th century.

b. Spatial Patterns

Figure 3.3 illustrates the spatial response in the CESM LE mean during the 3 years following the Pinatubo eruption. Ocean heat loss is strongest during the first year (year 0, 1-12 months post eruption) following the eruption with extensive heat flux anomalies and SST cooling over the tropics (Figure 3.3a), as expected from the immediate effects of stratospheric aerosol scattering. SST cooling intensifies in the subsequent year (year 1) over most of the North and South Pacific, particularly over

the Northwest Pacific subpolar region where extensive ocean heat loss also occurs (Figure 3.3b). El Niño-like tropical Pacific surface warming accompanies this cooling, and is associated with significant ocean heat loss along the equatorial region. In the following year (year 2), air-sea heat fluxes anomalies are largely subdued, while negative SST anomalies persist over the northwest subpolar and equatorial Pacific and the north Atlantic. We also note surface warming over the Southern Ocean that persists throughout the three years following eruption, inducing an asymmetrical SST response between hemispheres.

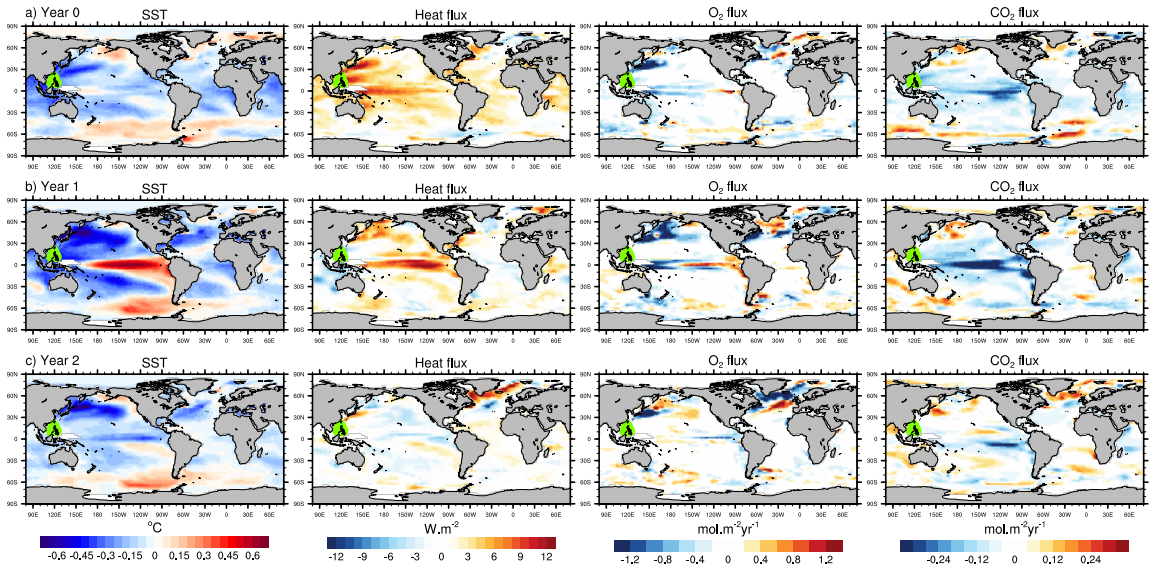

Figure 3.3. Evolution of annual mean anomalies in SST, Heat flux, F_{O2}, and F_{CO2} in the CESM LE mean during, a) 1-12 months (year 0), b) 13-24 months (year 1), c) 25-36 months (year 2) after the eruption of Pinatubo. Anomalies here are calculated as annual mean differences at specified years from the 5-year mean prior to the eruption year. Positive flux denotes flux out of the ocean. Green triangle indicates eruption location.

The ocean biogeochemical response is more regionally focused and varies less over time (right two panels of Figure 3.3), with the largest anomalies occurring during year 1 (13-24 months post eruption). Persistent and intense O_2 drawdown is evident over regions of intermediate and deep water formation such as the Northwest Pacific, North Atlantic, and the Southern Ocean. At lower latitudes, anomalous O_2 outgassing along the Pacific cold tongue acts to reduce the global oceanic O_2 uptake. CO_2 flux, on the other hand, is dominated by broad and intensive uptake in the tropical Pacific, and is accompanied by weak outgassing at higher latitudes. The low latitude ocean biogeochemical response to Pinatubo is reminiscent of El Niño impacts on air-sea O_2 and CO_2 exchanges that are typically dominated by equatorial ocean dynamics (Eddebbar et al., 2017; Feely et al., 2002).

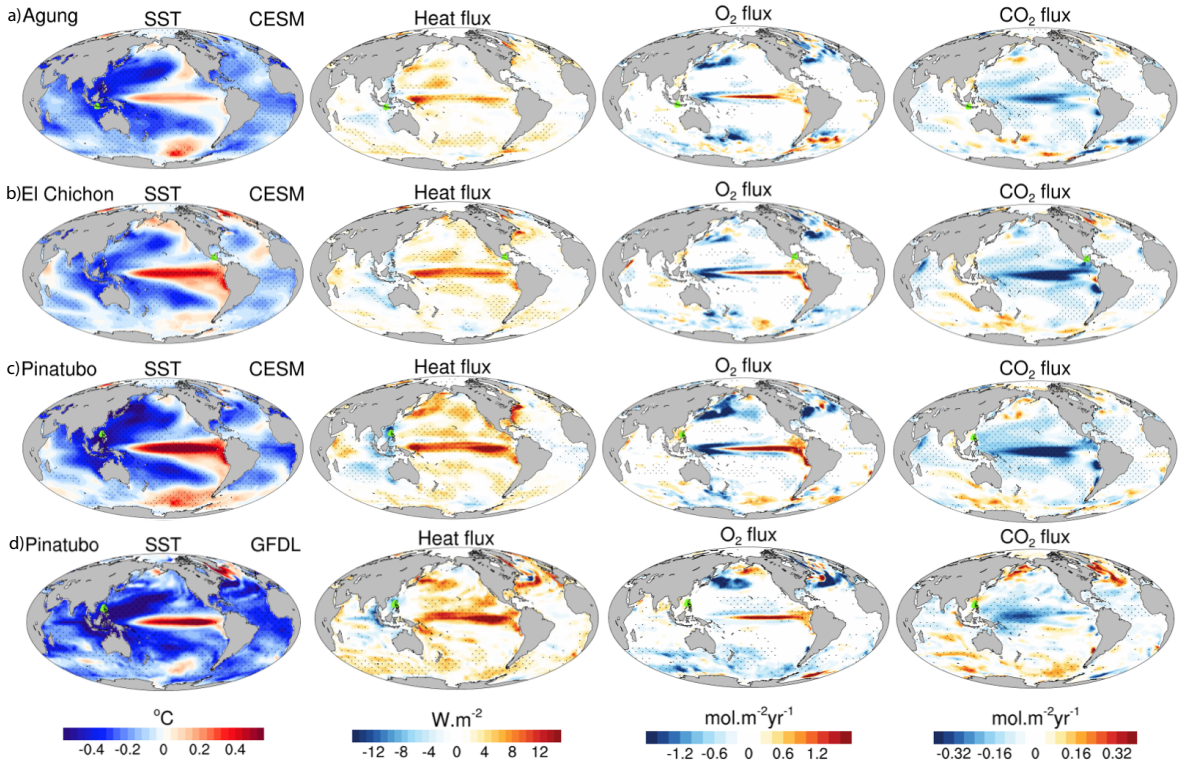

Figure 3.4. Anomalies in in SST, Heat flux, F_{O2}, and F_{CO2} in the CESM LE mean for the calendar year (i.e. 6-17 months) following the eruptions of a) Agung, b) El Chichon, and c) Pinatubo. d) is same as c) but for the GFDL LE mean. Anomalies are calculated as annual mean differences from the 5-year mean prior to the eruption year. Eruption locations are shown in green triangles. Stippling indicate statistically significant anomalies at the 95% confidence level. Positive flux denotes flux out of the ocean.

Figure 3.4 shows the oceanic response across all three eruptions. As found in the global response (Figure 3.1), the intensity of these patterns scales with the volcanic magnitude, with Pinatubo showing the most striking response. Similar patterns emerge for all variables across volcanic events, suggesting a relatively consistent response to tropical eruptions driven by similar governing mechanisms. These distinct spatial patterns at high latitudes and the El Niño-like response at low latitudes emerge despite

a zonally uniform volcanic forcing. Before we examine processes driving this response in detail, we first compare these CESM LE results to the GFDL LE response, and evaluate observations for these volcanic imprints.

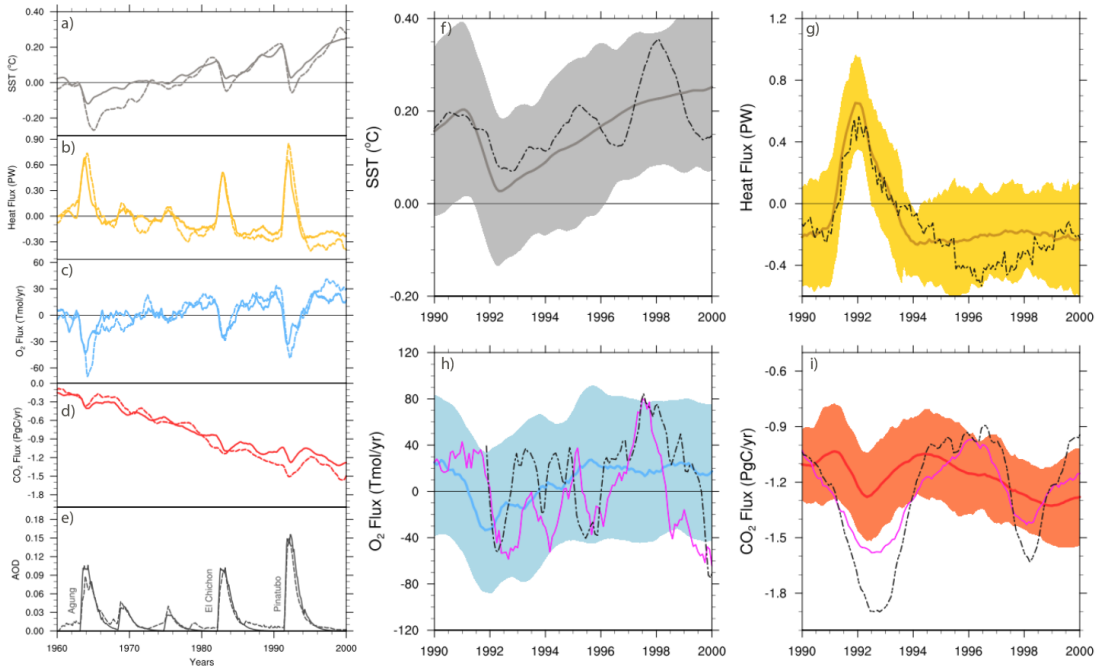

Figure 3.5. Comparison of CESM LE mean (solid line) and GFDL LE mean (dashed line) in a) global mean SST, b) air-sea heat, c) O_2 flux, d) CO_2 flux, and e) stratospheric AOD at 500nm. Right panels show a comparison of CESM LE mean to observations-based estimates during the Pinatubo period for f) global mean SST from the reynolds product (dashed black) and simulated SST (thick grey line), g) air-sea heat flux from the Liu et al (215) product and simulated heat flux (orange), h) O_2 flux (simulated LE in blue) vs. the observations-based flux of APO scaled down by 50% (black dashed) and hindcast simulation flux of APO (purple), and i) CO_2 flux (LE simulation in red) vs. observations-based (black dashed) and hindcast simulation (purple). The observations-based APO flux is normalized (by 50%) to visualize phase comparison with simulated APO variability in the hindcast simulation. Series are seasonally detrended and smoothed with a 12-month running mean. Anomalies in observations are aligned with models using the CESM LE 1990-91 mean as a reference period. Color shadings indicate 2σ across ensemble members. Positive flux denotes flux out of the ocean.

4. Comparison of Models and Observations

a. Comparison to the GFDL LE

A comparison of the CESM LE and GFDL LE means in Figure 3.5a-e shows a similar ocean response despite differences in model structure and volcanic forcing. We note, however, slightly larger SST cooling, ocean heat loss and O_2 uptake in GFDL LE (Figure 3.5a-c, dashed line), particularly following Agung even though AOD values used in the GFDL simulations are actually lower. A slightly larger response to the long-term anthropogenic forcing is also found in GFDL LE, suggesting a higher sensitivity to volcanic forcing in this model.

Due to the lack of a natural carbon tracer in GFDL, we compare the contemporary carbon flux response (i.e., anthropogenic and natural) in both models, and find noticeable interannual-to-decadal variability associated with volcanic events (Figure 3.5d). Similar to natural carbon, contemporary carbon uptake is initially intensified after eruptions, followed by a multiyear recovery. The Pinatubo eruption decade shows an intriguing deceleration of ocean carbon uptake when compared to volcanically weak decades (e.g., 1970's), especially in GFDL where recovery seems to overcompensate for the initial response.

The spatial patterns of the oceanic response are similar between the GFDL and CESM LE means following the Pinatubo eruption (Figure 3.4c-d), including the El Niño-like response at low latitudes and the convective patterns found at higher latitudes. More intensive SST cooling is evident in GFDL LE over the northern subtropical Pacific as well as a more confined warming in the equatorial Pacific region. The hemispheric response is more symmetrical in GFDL than in CESM due to broad cooling over the Southern Ocean and the Atlantic. In both models, these patterns are

statistically significant at the 95% confidence level across eruptions, with the exception of the weak equatorial Pacific warming following Agung in CESM, and the El Chichon and Agung eruptions (not shown) in GFDL, potentially due to their weaker forcing or earlier eruption season (Stevenson et al., 2017).

b. Comparison to Observations

Given the consistent global mean response across models, we focus our model-observation comparison on the CESM LE response after Pinatubo (Figure 3.5f-i). Similar to an individual ensemble member, volcanic imprints in observations (dashed black lines) are embedded within the climate system's internal variability, which we characterize here using the 2σ spread across ensemble members (shading).

Observed global SST cooling and ocean heat loss following the Pinatubo eruption are in general agreement in phase and magnitude with the CESM LE mean response (Figure 3.5f-g). A potentially longer heat flux recovery emerges in the observations-based product compared to the CESM LE mean response, though this behavior is well within the 2σ spread and may be influenced by internal variability. Global SST cooling is also observed despite the occurrence of an El Niño event during the eruption year, which typically tends to warm global SST. Similar spatial patterns emerge in observations during peak cooling (year 1), including the counterintuitive El Niño-like warming over the eastern and central equatorial Pacific and the Southern Ocean (Figure 3.6), revealing potentially detectable regional volcanic imprints in the ocean following Pinatubo.

Next, we compare the O_2 flux response to APO flux anomalies inferred from atmospheric measurements of O_2 and CO_2 (dashed black line in Figure 3.5h). APO variability on interannual timescales is largely dominated by changes in air-sea O_2 flux (Eddebbar et al., 2017), and thus APO can be used to compare models and observations of air-sea O_2 flux anomalies following eruptions. A noticeable APO drawdown is observed followed by large variability, which is in line with the expected volcanic response and the low signal-to-noise found in CESM LE (Figure 3.1c). A hindcast simulation of CESM (purple line in Figure 3.5h) which independently simulates the ocean response to "observed" atmospheric forcing, shows a similarly delayed APO drawdown, recovery, and enhanced variability that are driven primarily by O_2 fluxes, lending further confidence in the observed APO features. We note that the "observed" APO flux has been normalized by 50% to visualize phase comparison with the CESM LE and hindcast simulation and that the actual magnitude of the APO anomaly following Pinatubo exceeds 170 $Tmol.yr^{-1}$, which is well outside the 2σ ensemble spread.

The SOCAT-based CO_2 flux anomaly (dashed black line in Figure 3.5h) also shows vigorous ocean carbon uptake following Pinatubo that is in phase with the CESM LE and hindcast results (red and purple lines respectively). This observed CO_2 uptake represents the largest flux anomaly during the 1990's which includes the reduced outgassing due to the 1997-1998 El Niño event (Feely et al., 2002), and is well outside the 2σ spread, independently supporting a larger biogeochemical sensitivity to eruptions in observations.

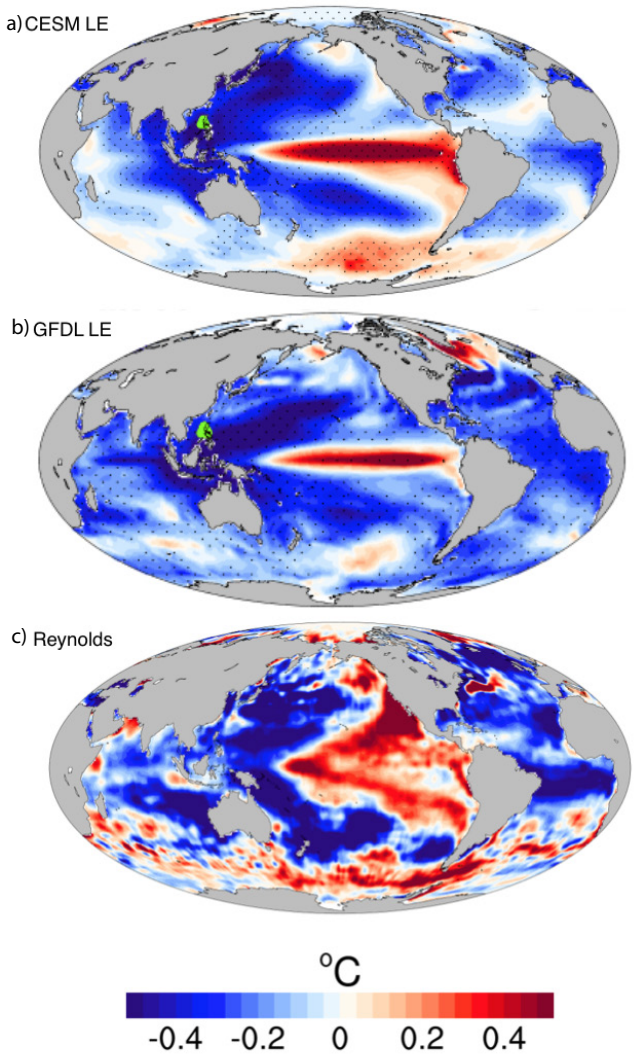

Figure 3.6. Spatial SST anomalies in the a) CESM LE mean, b) GFDL LE mean, and c) observations, during year 1 (13-24 months post eruption). Anomaly is calculated as annual mean difference from the 5-year mean prior to eruption year. Stippling indicate statistical significance at the 95% confidence level using a two-tailed Student's t-test.

5. Mechanisms

The general consistency of the ocean response across eruptions, models and observations (Figure 3.4-3.6) indicates distinct and robust mechanisms driving the oceanic response to tropical eruptions. The emergence of an El Niño-like response is

especially of interest, given its central role in modulating the SST, heat and CO_2 flux anomalies and buffering the global O_2 uptake. Next, we examine governing processes driving the physical and biogeochemical ocean response, focusing again on the Pinatubo eruption.

a. ENSO Response

The time evolution of equatorial Pacific (2ºN-2ºS) SST and mixed-layer depth anomalies after Pinatubo is shown for the CESM and GFDL LE means and observations in Figure 3.7. In both models, initial cooling in the eastern and central Pacific directly follows eruption (year 0). This is quickly followed by considerable warming (~ 1ºC) 12 months later (year 1) peaking in early winter in CESM and late winter in GFDL, before cooling takes over again in subsequent years (year 2 and 3). These SST changes are preceded in both models by anomalies in mixed layer depth that propagate from the western and central Pacific, suggesting a dynamic source of SST anomalies. In contrast to the simulations, observations show substantial warming during the eruption year (Figure 3.7b-d), likely due to an El Niño event that was already underway prior to eruption. Similarly to the models, a subsequent moderate SST warming and mixed layer deepening is also observed in the central and eastern Pacific. This observed warming peaks in late winter of the year following the eruption (year 1) and exhibits El Niño-like global patterns (Figure 3.6c). Figure 3.7 illustrates a temporally rich and complex equatorial SST response that is consistent between models and with potentially detectable imprints in nature.

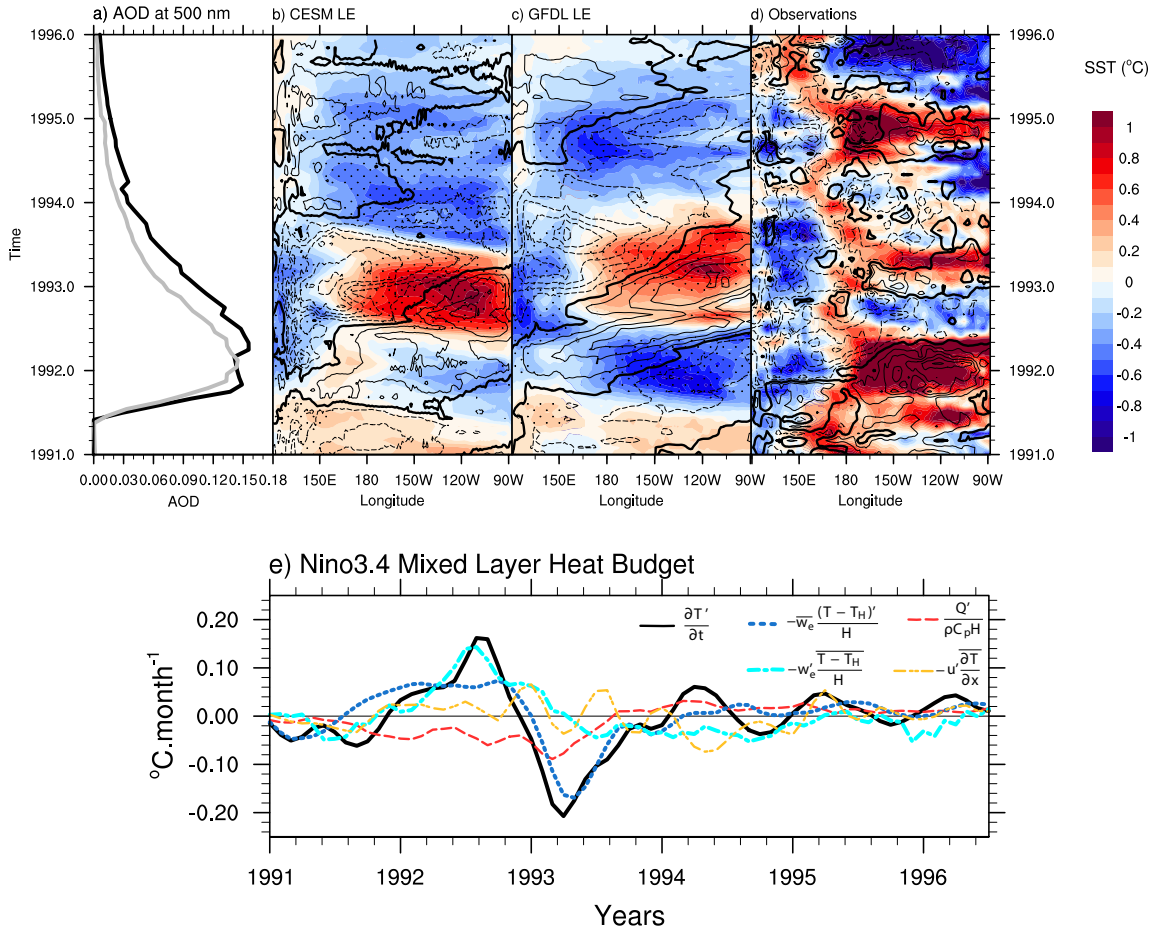

Figure 3.7. Hovmöller of a) AOD from CESM (black) and GFDL (gray), and anomalies in SST (shading) and mixed layer depth (contour) averaged over the equatorial Pacific band (2ºN-2ºS) following Pinatubo for the b) CESM LE mean, c) GFDL LE mean, and d) observations from the NOAA Reynolds product and GODAS reanalysis. e) Mixed layer heat budget over the Niño3.4 equatorial region (2ºN-2ºS) showing only dominant terms for visual clarity, including heating tendency (black), thermocline feedback term (dotted dark blue), Ekman upwelling feedback (cyan), heat flux (dashed red), and zonal advective term (orange dashed). Mixed layer heat budget terms are smoothed with a 3-month running mean. Mixed layer anomalies are contoured every 3m for models and every 10 m for observations. 20ºC isotherm depth is used to represent mixed layer depths for the GFDL LE and observations. Stippling indicates significance at the 95% confidence level using a two-tailed Student's t-test.

To understand the counterintuitive warming response to volcanic radiative cooling, we examine the mixed layer heat budget over the equatorial Niño3.4 region in the CESM LE mean, following Huang et al. (2010) as:

$$\frac{\partial T}{\partial t} = \frac{Q}{\rho C_p H} - u\frac{\partial T}{\partial x} - v\frac{\partial T}{\partial y} - w_e\frac{T - T_H}{H} - D$$

where T represents the mixed layer mean temperature and T_H represents temperature at the base of the mixed layer, Q represents the net air-sea heat flux going into the mixed layer, ρ is seawater density, Cp is seawater heat capacity, H is the mixed layer depth, u and v represent zonal and meridional current velocities respectively averaged over the mixed layer, D represents residual contributions from diffusive mixing and mesoscale processes, and w_e is the entrainment velocity, calculated as:

$$w_e = \frac{\partial H}{\partial t} + u_h\frac{\partial H}{\partial x} + v_h\frac{\partial H}{\partial y} + w_h$$

where u_h , v_h , w_h represents velocities at the base of the mixed layer.

For visual clarity, only dominant terms driving $\frac{\partial T'}{\partial t}$ (black line) are shown in Figure 3.7e, where a prime notation (e.g., T') represents an anomaly while a bar notation (e.g., $\overline{w_e}$) indicates a long-term mean. Figure 3.7e shows that the mixed layer heating tendency $\frac{\partial T'}{\partial t}$ (black line) is driven in the 12 months following eruption primarily by the thermocline feedback term ($-\overline{w_e}\frac{(T-T_H)'}{H}$, dotted dark blue), which represents the upwelling by the mean entrainment velocity transporting anomalies in the vertical temperature contrast at the base of the mixed layer. Warming of the mixed layer is later reinforced and eventually dominated by the Ekman upwelling feedback term ($-w_e'\frac{\overline{T-T_H}}{H}$, dashed cyan), which represents the weakened upwelling of cold thermocline waters. The zonal advective term ($-u'\frac{\overline{\partial T}}{\partial x}$, dashed orange) also contributes

to warming, albeit to a much lesser extent. In addition to initiating the warming response, the thermocline feedback term ($-\overline{w_e}\frac{(T-T_H)'}{H}$) also drives the termination of the warming event and subsequent cooling. The important role of the thermocline feedback in the initiation of the warming response and lagged dominance of the Ekman upwelling feedback reflects two possible and distinct mechanisms:

i) upwelling of unperturbed subsurface waters weakens surface cooling thereby reducing the zonal SST gradient (i.e., ocean thermostat mechanism), and initiating Bjerknes feedbacks that lead to El Niño; or

ii) upwelling of warm subsurface anomalies (e.g., due to deepening of the thermocline by internal waves) warms SST in the east, and leads to El Niño through initiation of Bjerknes feedbacks.

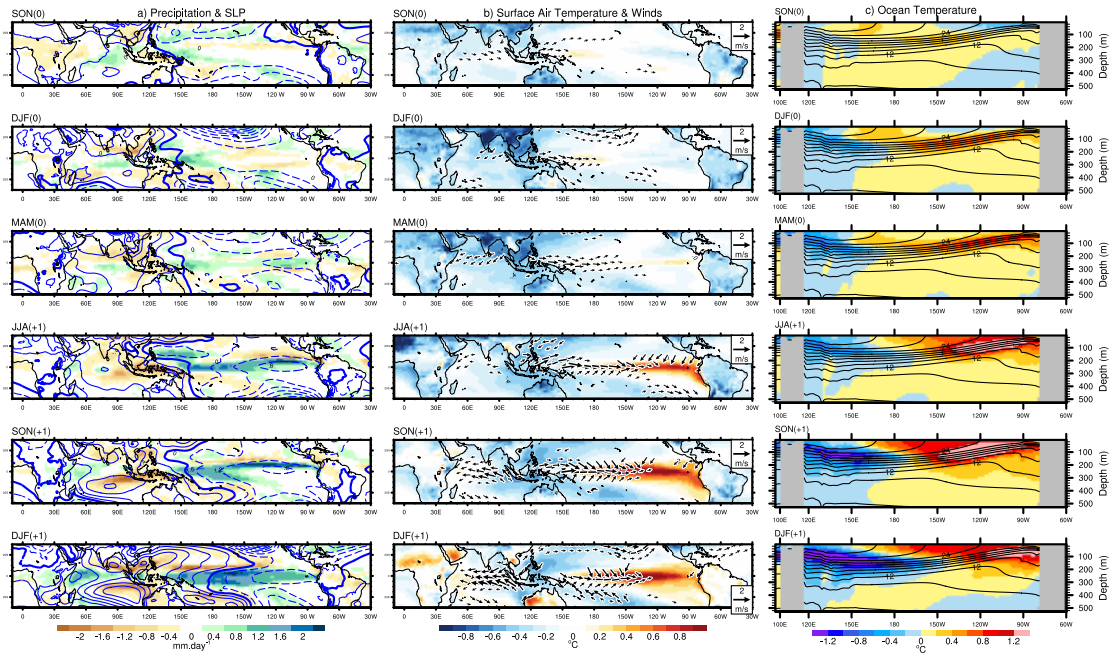

Figure 3.8. Seasonal evolution of anomalies following the eruption of Pinatubo in a) rainfall and SLP, b) surface air temperatures, and winds, and c) ocean temperatures in longitude vs.

(Figure 3.8 continued) depth averaged over the equatorial Pacific sector (2ºN-2ºS) in the CESM LE mean. Blue contours in panel a) show SLP anomalies contoured every 0.2 hPa. Vectors show wind anomalies with 2 m reference wind in upper right box; wind anomalies weaker than 0.5 $m.s^{-1}$ are omitted for visual clarity. Black contours in panel c) show climatological mean ocean temperature averaged over 2ºN-2ºS, contoured every 2ºC.

To visualize which mechanism is at play, Figure 3.8 illustrates the seasonal evolution in the CESM LE mean of precipitation, sea level pressure, surface air temperature and wind anomalies and equatorial ocean temperature anomalies at depth following Pinatubo. In contrast to what is expected from the dynamical thermostat mechanism (Mann et al., 2005; Emile-Geay et al., 2008), the equatorial Pacific zonal SST gradient actually increases in fall [SON(0)] and winter [DJF(0)] following eruption through surface cooling in the east (Figure 3.8b, upper two panels). This SST cooling overlays an increasingly large subsurface warming in the eastern and central Pacific associated with a gradual deepening of the thermocline (Figure 3.7a and 3.8c). No significant surface wind anomalies in the eastern Pacific superpose this initial subsurface warming, indicating remote forcing via the ocean from the western Pacific, where persistent westerly wind anomalies drive the eastward propagation of downwelling Kelvin waves from fall [SON(0)] through spring [MAM(0)] following the eruption. This subsurface warming feeds eastern and central equatorial Pacific SST warming, which reduces the zonal SST gradient and significantly weakens the Walker circulation during the subsequent summer [JJA (+1)] and fall [SON (+1)], leading to the full development of El Niño conditions by winter [DJF(+1)] of the following year. Figure 3.8 thus illustrates that the initial surface wind anomalies over the western

Pacific play a more prominent role in initiating the El Niño response than the buffering effects of the ocean dynamical thermostat evoked by Mann et al. (2005).

These initial and persistent westerly wind anomalies initiating El Niño are associated with dry conditions and cold surface air temperatures over the Maritime Continent and South Asia (Figure 3.8a-b upper three panels). An expected consequence of volcanic radiative forcing is faster cooling over land relative to ocean (Ohba et al., 2013), due to its lower heat capacity and distinct surface feedbacks, resulting in a striking land-ocean temperature gradient between the Maritime Continent and the western Pacific. Following the Gill model, which predicts an eastward propagation of easterly wind-inducing atmospheric Kelvin waves following heating of equatorial convective regions (Gill 1980), the intense volcanic cooling of the Maritime Continent suppresses convection and induces anomalous divergence and eastward atmospheric Kelvin waves propagation of westerly wind anomalies over the western Pacific. These persistent westerly wind anomalies continue to excite oceanic downwelling Kelvin waves throughout the eruption year (year 0) until the Bjerknes feedbacks take over [JJA(0) onward], when surface warming and weakened walker circulation dominate, along with increased rainfall over most of the equatorial Pacific and a southward migration of the Inter-Tropical Converge Zone (ITCZ).

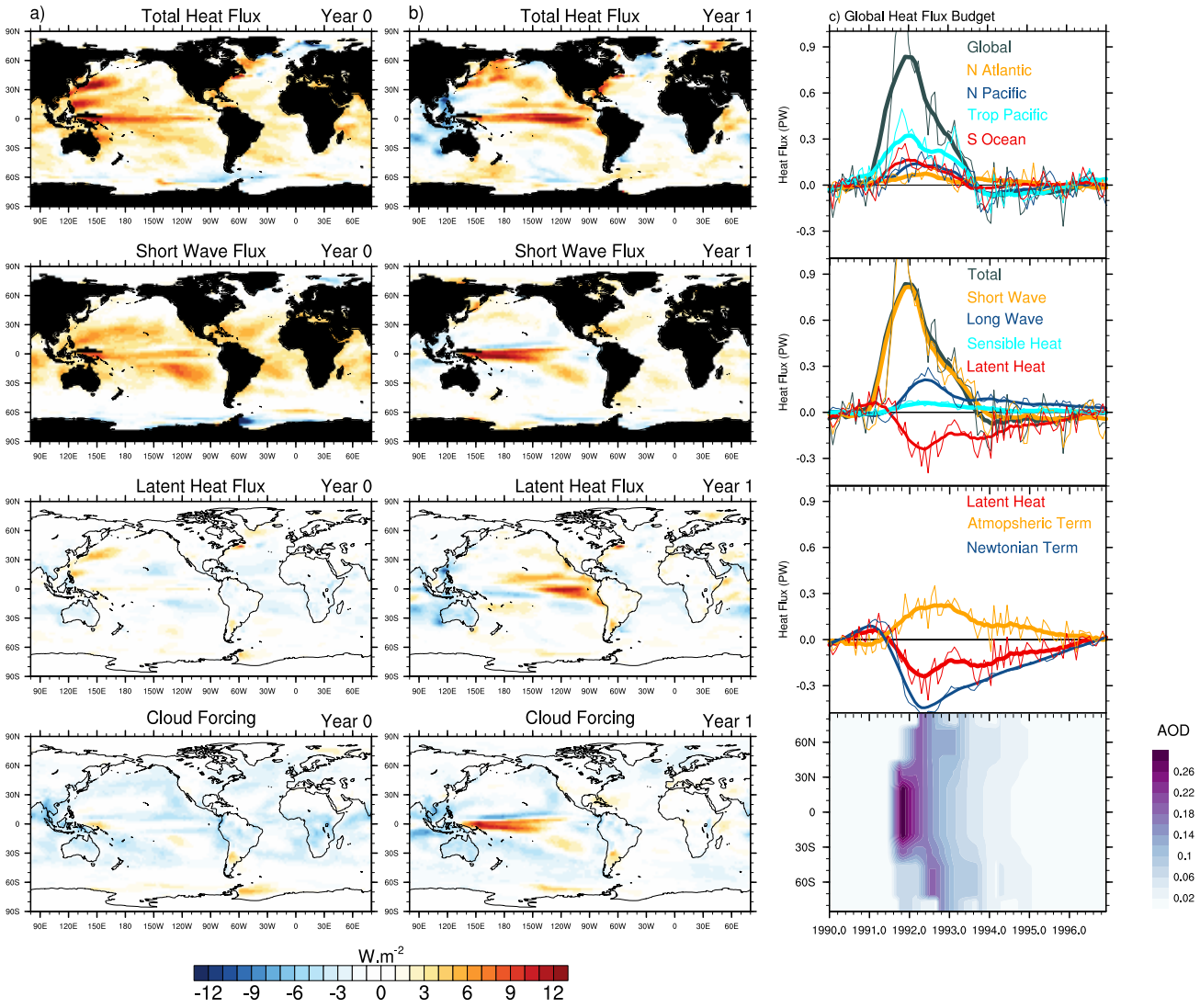

Figure 3.9. Anomalies in total heat, shortwave, latent heat fluxes, and cloud forcing during a) the Pinatubo eruption year (0-11 months post eruption), and b) a year after the eruption year (12-23 months). Panel c) shows the globally integrated heat flux budget, decomposed by region (top) and by flux component (2nd from top), including short-wave, long-wave, sensible, and latent heat fluxes. Third panel shows latent heat fluxes decomposed into atmospheric and Newtonian terms. Lower panel shows latitudinal distribution of AOD at 500 nm. Thin lines indicate unfiltered series, while bold lines show 12-month running means. Positive anomalies denote anomalous flux out of the ocean.

b. Ocean Heat Response

While oceanic heat loss is expected following eruptions due to reduced short-wave radiation, it is unclear how feedbacks in the ocean-atmosphere system amplify or dampen the total air-sea heat flux response or what determines its distinct spatial patterns and evolution. We examine the contribution of different components of the net air-sea heat flux (Q_T) in the CESM LE mean, which is calculated as:

$$Q_T = Q_{SW} + Q_{LW} + Q_{SH} + Q_{LH}$$

where Q_{SW} and Q_{LW} represent short-wave and long-wave radiative fluxes respectively, and Q_{LH} and Q_{SH} represent turbulent latent heat and sensible heat fluxes respectively. Latent heat fluxes are driven by two distinct processes: a Newtonian term (Q_{NT}), i.e. the ocean's SST damping response, and an atmospheric term (Q_{ATM}) due to changes in surface humidity, winds, and other atmospheric properties. We isolate contributions from Q_{NT} following (Xie et al., 2010) as:

$$Q_{NT} = \frac{L}{R_v \overline{T}^2} \overline{Q_{LH}} T'$$

where L is the latent heat of evaporation, R_v is the water vapor gas constant, Q_{LH} represent the mean latent heat flux, T' is the SST anomaly, and calculate Q_{ATM} as a residual ($Q_{ATM} = Q_{LH} - Q_{NT}$).

The initial heat flux response (year 0) is dominated by shortwave anomalies over the tropics (Figure 3.9a), as expected due to the immediate and direct effects of aerosol scattering following a tropical eruption. However, the anomalies in Q_{SW} are not latitudinally uniform as expected from zonally uniform volcanic forcing, but are

modified regionally by a widespread decrease in cloud radiative forcing due to reduced cloud cover and weakened albedo. Cloud feedbacks, thus, act initially to dampen the volcanic radiative cooling effects in CESM, weakening the initial oceanic heat loss.

The subsequent response (year 1) involves a more subtle balance between heat flux components (Figure 3.9b-c). Q_{SW} still dominates the total response despite a significantly diminished tropical AOD. Q_{SW} anomalies are localized over the equatorial Pacific region and are driven largely by enhanced cloud albedo due to El Niño-related shifts in convection (Figure 3.8a). This heat loss is reinforced globally by widespread anomalies in Q_{LW} and to a smaller extent by sensible heat flux anomalies over the north subpolar Pacific (not shown). Latent heat anomalies further reinforce the tropical Pacific Q_T anomalies in the east, but act to buffer the net heat flux response globally through the buffering effects of Q_{NT} (Figure 3.9c), analogously to the ocean response to anthropogenic forcing (Xie et al., 2010).

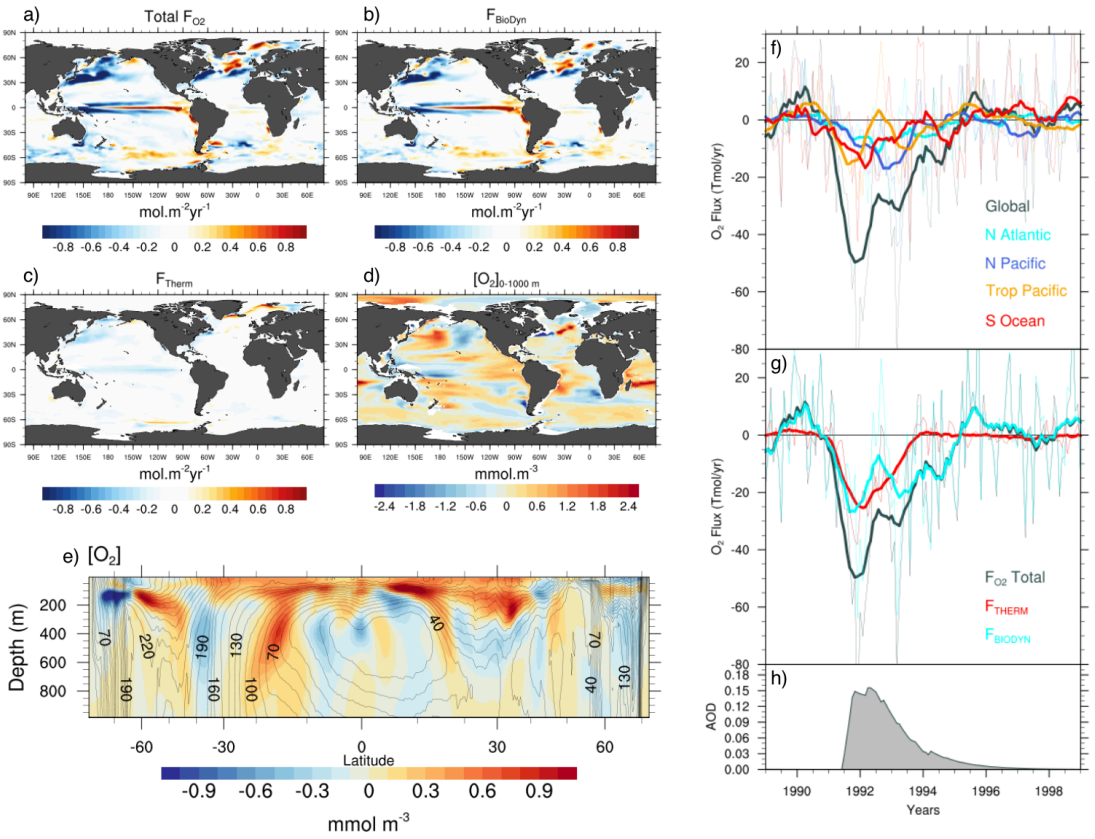

Figure 3.10. Anomalies following Pinatubo in a) O_2 flux, decomposed by b) biodynamical and c) thermal contributions, d) depth-averaged $[O_2]$ in the upper 0-1000 m ocean, e) zonally averaged $[O_2]$ change in the upper 1000 m. Right panel, shows global O_2 flux decomposition by f) regional contributions and g) process contributions. h) Globally averaged 500 nm AOD. Spatial anomalies are annual mean differences during two years after eruption from the 5-year mean prior to eruption. Thin lines indicate unfiltered series, while bold lines show 12-month running means. Positive flux denotes anomalous O_2 flux out of the ocean.

c. Oxygen Response

The simultaneous global uptake of O_2 and CO_2 shown in Figure 3.1 initially suggests thermal effects as a dominant driver of O_2 and CO_2 response, since cooling would increase solubility and drive influx in both gases. However, the spatial patterns of O_2 and CO_2 uptake are negatively correlated (Figure 3.3), suggesting that biological and dynamical processes (e.g., convection and upwelling of O_2-depleted, DIC-rich

waters) may play a more prominent role (Figure 3.10). We decompose the contribution of these effects as:

$$F_{O_2} = F_{Therm} + F_{BioDyn}$$

where F_{Therm}, the thermal component of O_2 flux, is calculated following (Keeling et al., 1993) as:

$$F_{Therm} = \frac{\partial [O_2]^{sol}}{\partial T} \frac{Q_T}{\rho . C_p}$$

where $[O_2]^{sol}$ represents surface O_2 solubility, Q_T is the net air-sea heat flux, ρ is water density, and C_p is seawater heat capacity. F_{BioDyn}, the O_2 flux component due to biological and dynamical processes, is computed as a residual.

As noted in Chapter 1, the heat scaling formula of Keeling et al. (1993) assumes that mixed layer oxygen equilibrates instantly in response to heat fluxes, and neglect the effects of mixing and penetration of shortwave irradiance below the mixed layer on gas supersaturation, which is suggested to lead to ~20% reduction in the amplitude of the seasonal cycle of O_2 flux (Dietz and Oschlies, 2005; Jin et al., 2007). We re-evaluate these effects on interannual timescales using a 100-year coupled simulation of CESM using an abiotic O_2 tracer that is inactive biologically and thus acts like an inert gas. Figure 3.11a shows that, similarly to Jin et al. (2007) and Dietz and Oschlies (2005), the heat scaling formula of Keeling et al. (1993) overestimates the thermal exchange of O_2 by about 20%. However, on interannual timescales, this method performs strikingly well (Figure 3.11b), likely due to disproportionately smaller effects of disequilibrium on interannual timescales. We conclude that the O_2

flux decomposition used in this study is robust for the volcanic timescales considered here.

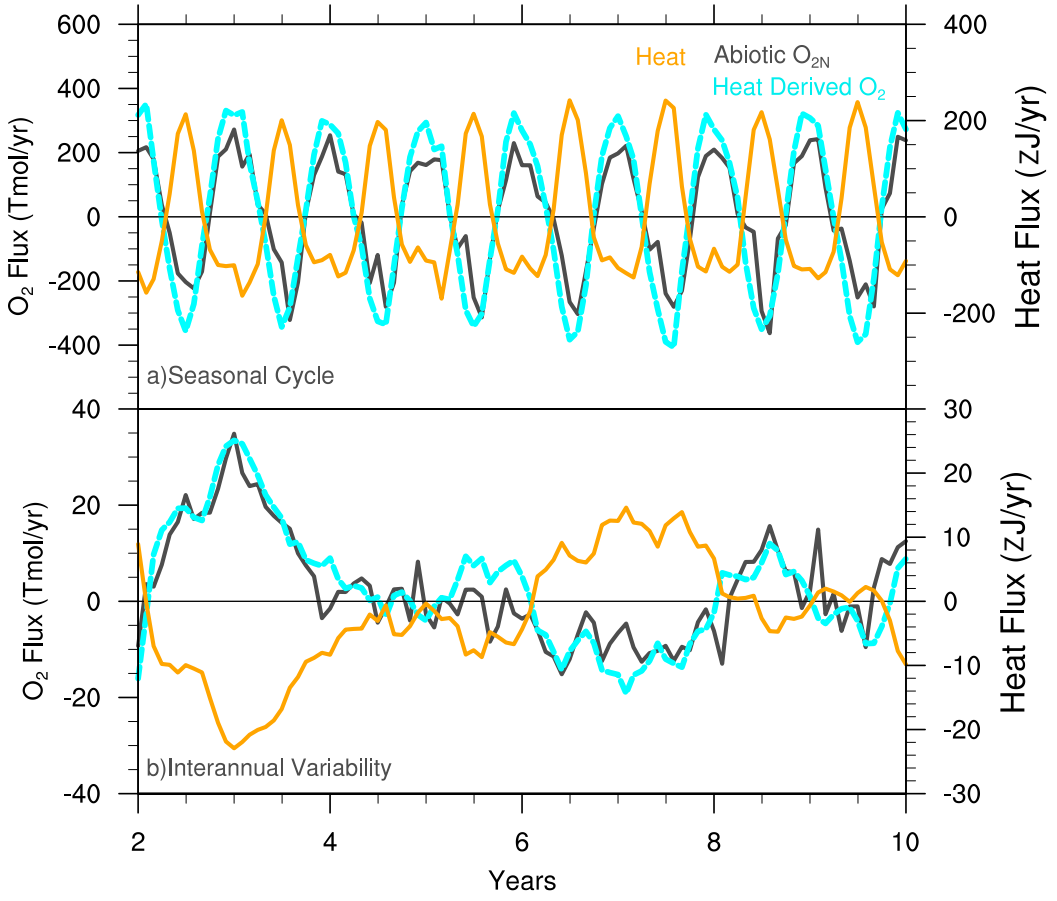

Figure 3.11. a) Seasonal cycle and b) interannual variability in abiotic (thermal) O_2 flux (black) and heat-derived thermal flux (cyan) vs. heat flux (orange) from a 100 year unforced coupled (control) simulation of CESM.

Figure 3.10g shows that thermal and "biodynamical" effects reinforce each other and contribute nearly equally to the global response, but that the F_{BioDyn} response persists longer. Whereas the global F_{Therm} response is the sum of relatively uniform but

weaker spatial anomalies, the F_{BioDyn} response is a net balance of intense O_2 uptake at high latitudes and anomalous outgassing along the equatorial Pacific (Figure 3.10b-c). This anomalous equatorial O_2 outgassing reflects the suppression of climatological ocean O_2 uptake along the cold tongue due to ENSO-related weakening of vertical transport of O_2-depleted waters by reduced upwelling rates and deepening of thermocline as illustrated in Figure 3.7b and Figure 3.8. Weaker anomalous O_2 uptake also occurs as these waters diverge off the equator, likely due to El Niño-induced reduction in primary productivity (Eddebbar et al., 2017).

At higher latitudes, the F_{BioDyn} response is associated with intense surface cooling and large sensible heat and carbon fluxes to the atmosphere (Figure 3.3), indicating vigorous convection and upwelling due to weakened stratification during anomalously cool winter seasons following eruptions. These ventilation events lead to significant O_2 drawdown and introduction of new [O_2] into the subtropical thermocline through mode and intermediate water mass formation, as shown by the depth-integrated [O_2] anomalies and vertical profile of zonally averaged [O_2] (Figure 3.10d-e). Over the tropical Pacific, a strong dipole in [O_2] anomalies emerges due to ENSO-related isopycnal heaving and contraction of the eastern tropical Pacific Oxygen Minimum Zone following eruption. Figure 3.10 describes yet another complex ocean response to tropical eruptions, whereby intensified convection and ventilation of interior waters drives substantial O_2 drawdown that is compensated in the global integral by the opposing effects of the El Niño response at lower latitudes.

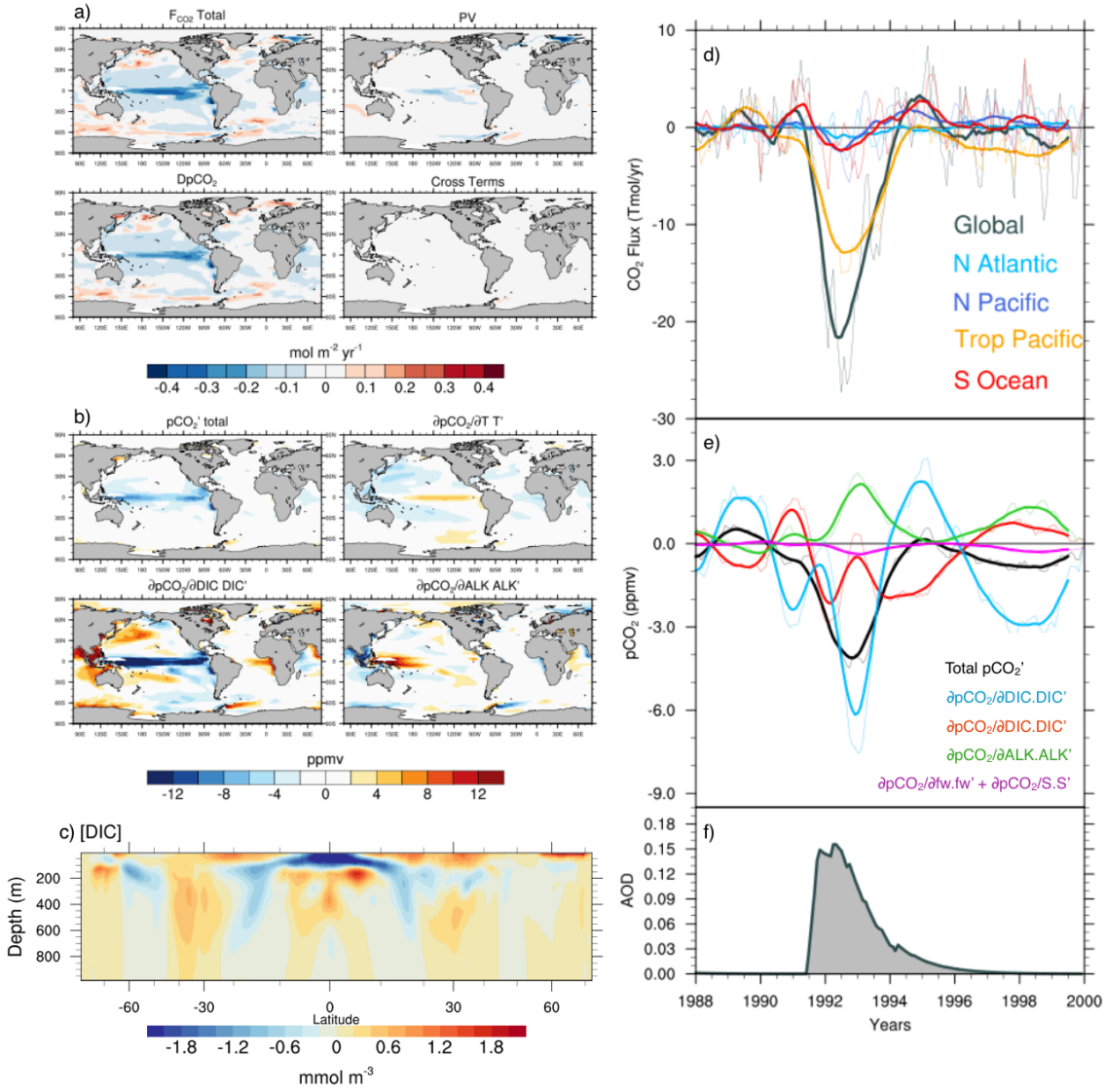

Figure 3.12. Anomalies in a) CO_2 flux decomposed by contributions from gas exchange piston velocity (PV'), ΔpCO_2', and cross terms, and b) pCO_2 anomalies decomposed into thermal, DIC, and alkalinity contributions. c) Shows anomalies in zonally averaged DIC with depth, averaged during the two years following eruption. Right panel shows d) regional flux contributions, e) process contributions to tropical Pacific pCO_2 anomalies including temperature, DIC, Alkalinity, freshwater, and salinity effects, and f) AOD at 500 nm with latitude. Spatial anomalies are annual mean differences during two years after eruption from the 5-year mean prior to eruption. Thin lines show unfiltered series, while bold lines show 12-month running means. Positive flux denotes anomalous CO_2 flux out of the ocean.

d. Carbon Response

In contrast to the O_2 flux response described above, CO_2 uptake occurs primarily in the tropical Pacific, dominating over small outgassing anomalies at high latitudes (Figure 3.12a and 3.12d). Various processes influence the air-sea exchange of CO_2, which is calculated in the models following Wanninkhof (1992) as $F_{\mathrm{CO}_2} = K\Delta p\mathrm{CO}_2$ where K is the gas exchange piston velocity, a function of wind, ice fraction, and the Schmidt number, and $\Delta p\mathrm{CO}_2$ is the atmospheric-ocean difference in the partial pressure of CO_2. We use a Taylor expansion to separate the effects of gas piston velocity due to changes in winds and sea ice fraction vs. changes in $\Delta p\mathrm{CO}_2$, following Long et al. (2013):

$$F'_{CO_2} = \overline{K}\Delta p\mathrm{CO}'_2 + K'\overline{\Delta p\mathrm{CO}_2} + (\,K'\Delta p\mathrm{CO}'_2 - \overline{K'\Delta p\mathrm{CO}'_2})$$

Figure 3.12 shows that $\Delta p\mathrm{CO}_2$ drives most of the CO_2 flux anomaly and that reduced piston velocity, due to weakened easterlies (Figure 3.8b), reinforces those changes in the central equatorial Pacific. We examine the contribution of different processes driving the surface ocean $p\mathrm{CO}_2$ anomaly, including changes in surface temperature (*T'*), DIC (DIC'), alkalinity (*ALK*'), salinity (*S'*) and freshwater fluxes (*fw*'), following Lovenduski et al. (2007), as:

$$p\mathrm{CO}'_2 = \frac{\partial p\mathrm{CO}_2}{\partial T}T' + \frac{\partial p\mathrm{CO}_2}{\partial \mathrm{DIC}}\mathrm{DIC}' + \frac{\partial p\mathrm{CO}_2}{\partial ALK}ALK' + \frac{\partial p\mathrm{CO}_2}{\partial S}S' + \frac{\partial p\mathrm{CO}_2}{\partial fw}fw'$$

where *ALK* and DIC are salinity-normalized to isolate effects of fresh water on DIC and alkalinity.

Figure 3.12b and 3.12e show that DIC effects in the tropical Pacific dominate surface *p*CO2 changes. This DIC influence is regionally counteracted by the alkalinity effect over the western Pacific and by weak warming effects along the equator, while pCO_2 changes due to freshwater fluxes and salinity effects are of minor importance. DIC effects, however, act in the opposite sense outside of the tropical Pacific, likely due to enhanced convection and upwelling at higher latitudes where they are largely canceled by strong cooling effects.

The El Niño-like response to Pinatubo thus explains most of the changes to global carbon uptake, as a deepened thermocline and reduced upwelling rates weaken DIC transport to the surface and suppresses the outgassing of natural CO_2 in the tropical Pacific. The zonally-averaged vertical DIC anomalies shown in Figure 3.10c reflect the effects of these dynamical processes and further indicate that positive anomalies in DIC occur primarily in the subtropical upper waters as anomalously under-saturated equatorial waters take up CO_2 and diverge poleward where cooling intensifies carbon uptake. Figure 3.12, thus, illustrates that volcanic eruptions lead to anomalous CO_2 uptake primarily through reduced tropical Pacific outgassing of natural CO_2 via ENSO modulation of DIC transport to the surface.

6. Discussion and Summary

In this study, we evaluate the physical and biogeochemical ocean response to tropical eruptions in the Large Ensemble suites of CESM and GFDL. We find intense ocean cooling and O_2 and CO_2 uptake immediately follow eruptions in both models. These volcanic events act to significantly interrupt the advance of ocean warming,

deoxygenation, and natural carbon loss in the ocean's interior, and drive pronounced interannual-to-decadal variability in heat, O_2 and carbon fluxes and budgets. The spatial patterns associated with tropical eruptions in the CESM and GFDL LE suggest intensified convection and ventilation at higher latitudes and the development of El Niño-like conditions in the tropical Pacific. This El Niño-like response maintains persistent ocean heat loss beyond the lifetime of aerosols scattering through modulation of tropical clouds, and suppresses natural CO_2 outgassing in the tropical Pacific while buffering the oceanic O_2 uptake at high latitudes, thus playing a major role in the physical and biogeochemical ocean response to tropical eruptions.

The tropical climate evolution following Pinatubo shown here may help reconcile the immediate cooling found in certain models (McGregor and Timmermann 2011) with the subsequent El Niño warming indicated by paleoproxies (Adams et al., 2003; Li et al., 2013). Initial cooling in the tropical Pacific, however, is short-lived and weak in the CESM LE whereas the El Niño warming is robust, similar to paleoproxy findings (Stevenson et al., 2017). Here, we also note the existence of warm anomalies in observations that are consistent with the simulated response following Pinatubo, peaking in late winter/early spring winter of 1993, and occurring alongside intense cooling globally. The El Niño warming shown in CESM and GFDL LE is in general agreement with recent findings by other models, including the Model for Interdisciplinary Research on Climate (MIROC; Ohba et al., 2013), Institut Pierre-Simon Laplace model (IPSL; Khodri et al., 2017), the GFDL Climate Model, version 2.1 (CM2.1; Predybaylo et al., 2017), as well as the Last Millennium Ensemble (LME)

experiment of CESM described in Stevenson et al. (2017). We note, however, that the peak El Niño warming occurs during boreal winter in CESM and GFDL LE rather than boreal summer as found in other models (Khodri et al., 2017), consistent with a seasonally phased-locked response. We also note that the ENSO evolution described here is evident in both models following Pinatubo, and is less clear after the Agung and El Chichon eruptions, likely due to their weaker radiative forcing effects. The inter-model differences in the temporal evolution of ENSO and lack of a strong SST response in weaker eruptions may explain the lack of a robust El Niño response in CMIP5 ensemble studies (Ding et al., 2014).

Whereas a coherent volcanic response of ENSO is emerging across model-based and paleoproxy-based studies, proposed mechanisms remain at odds. Our results show a prominent role for the thermocline feedback in initiating surface equatorial warming, followed by a dominance of the Ekman upwelling feedback, while other processes (e.g. horizontal advection) play a minor role. This is in contrast to the dominance of meridional advection reported in the CESM LME (Stevenson et al., 2017) despite model similarity, signaling perhaps distinct processes for volcanic events of higher magnitudes or of different timing of eruptions. We also stress that the CESM LE mechanism described here is distinct from the ocean dynamical thermostat, where upwelling of unperturbed waters buffer volcanic cooling and reduces the equatorial zonal SST gradient (Mann et al., 2005; Emile-Geay et al., 2008). Here, significantly warmer waters, rather than "pristine" thermocline waters, are initially upwelled in the eastern and central equatorial Pacific leading to the full development

of El Niño through Bjerknes feedbacks. This subsurface warming is remotely forced by downwelling Kelvin waves that are excited by westerly wind anomalies over the western Pacific. Ohba et al. (2013) first reported the prevalence of these westerly wind anomalies following eruptions, but proposed their role in ENSO through direct weakening of the Walker circulation. The subsurface temperature evolution shown here suggests an oceanic link through the propagation of downwelling Kelvin waves that lead to a warmer source of upwelling. This mechanism is in general agreement with the model findings of Khodri et al. (2017) who report similar westerly wind anomalies, but which they link to a weakening of the western African monsoon. We do not find major changes in atmospheric circulation over the African continent (Figure 3.8), and suggest instead a localized source for westerly wind anomalies due to intense cooling and suppression of convection over South Asia and the Maritime Continent. The major role and persistence of these westerly wind patterns highlight the need for improved understanding of the atmospheric response to tropical eruptions over the tropical Indo-Pacific.

The CESM and GFDL LE results also indicate a significant role for ocean dynamics in driving the biogeochemical response to tropical eruptions. This is especially evident in the anomalous CO_2 uptake following eruptions, which is driven here primarily by El Niño-induced deepening of thermocline and weakening of upwelling rates, rather than the temperature-dependent solubility effects as currently understood (Brovkin et al., 2010; Frölicher et al., 2011, 2013). The CO_2 flux response shown here, in turn, indicates a robust El Niño-like ocean response, even when the

SST anomaly is ambiguous (e.g., Agung), providing similar insights gained from sea surface heights anomalies which show El Niño-like patterns following eruptions even in the absence of corresponding El Niño-like SST warming (Maher et al., 2015). Further, the early initiation and persistence of the CO_2 flux response suggest that volcanically forced El Niño behavior is distinct from internally generated El Niño.

The larger volcanic impacts on O_2 and CO_2 fluxes found in observations suggest a weak biogeochemical response to volcanic eruptions in models. Similar weak sensitivity in models has also been reported in comparisons of simulated vs. observed long-term [O_2] trends (Schmidtko et al., 2017) and interannual variability of [O_2] and APO fluxes (Rödenbeck et al., 2008; Long et al., 2016; Eddebbar et al., 2017). A possible source of the underestimate in the biogeochemical response to volcanoes is the lack of iron deposition from volcanic ash in models, as iron fertilization would lead to enhanced photosynthesis, and further CO_2 uptake (Hamme et al., 2010; Langmann et al., 2010). While the larger CO_2 uptake response found in observations supports a potential role for the neglected effects of iron fertilization in the models, the large observed APO uptake is not coherent with these effects, as iron fertilization would drive APO outgassing instead. The net balance of enhanced biological production vs. convection and ventilation on O_2 in the presence of iron fertilization however is not clear and merits further investigation.

The volcanic impacts presented here have important implications for interpreting recently observed trends in the ocean. The volcanic modulation of tropical climate, for instance, puts the multi-decadal variability of ENSO reported in coral-

based paleo-proxies (Sanchez et al., 2016) within the geologic context of variability in volcanic activity, as enhanced volcanic periods would be dominated by a positive phase of ENSO. Further, the strong volcanic modulation of oceanic O_2 in the north subpolar and subtropical Pacific during the 1960's, 1980's, and 1990's may have contributed to the well-observed bi-decadal variability of [O_2] in this region (Keeling et al., 2010). Similarly, the trend towards reduced carbon uptake during the recovery period (i.e., 1993-1997) following Pinatubo found in both CESM and GFDL LE is in line with the weakening of the ocean carbon sink during the 1990's reported by recent synthesis of the SOCAT pCO_2 data (Landschützer et al., 2015). Finally, enhanced ocean heat uptake remains the leading explanation for the decadal "hiatus" in global surface warming (Yan et al., 2016). While attention has been given primarily to anomalies in the 2000's decade, weaker ocean heat uptake in prior decades (1980s-1990's) due to the integrated effects of the Agung and Pinatubo eruptions may also play a role in modulating decadal variability in the ocean heat content and surface trends. While evaluating the signature of volcanic events in interior ocean properties remain challenged by sparse sampling and instrument calibration error, the volcanic signals emerging in the CESM and GFDL LE provide an important first step in evaluating trends and spatial patterns from externally forced variability and its interaction with ENSO.

Tropical eruptions reveal a complex ocean response to uniform radiative forcing that is highly relevant to discussions of geoengineering, which rarely address potential impacts on the oceans. One possible unintended consequence of a Pinatubo-

scale anthropogenic injection of sulfate aerosols in the stratosphere includes a counterintuitive El Niño-like warming over the tropical Pacific due to westerly wind anomalies arising from intense cooling and suppressed convection over the Maritime Continent. Systemic deepening of the central and eastern equatorial thermocline and weakening of equatorial upwelling may also lead to reduced nutrient supply to the surface, thereby reducing primary productivity. Similarly to volcanic eruptions, radiative management may also have positive outcomes for marine ecosystems, through immediate cooling and oxygenation of an increasingly warming and de-oxygenated ocean in the 21st century. Radiative management schemes, however, will likely involve subsequent injections that are maintained over several decades. The ocean response to radiative management, thus, likely defies a simple comparison to short-lived perturbations described here, and motivates a closer examination of geoengineering impacts on the oceans.

Acknowledgements

Chapter 3, in part, is currently being prepared for submission for publication of the material. Eddebbar, Y. A., Rodgers, K., Long, M.C., Subramanian, A., Xie, S-P., Keeling R.F. The dissertation author was the primary investigator and author of this material.

References

Adams, J. B., M. E. Mann, and C. M. Ammann, 2003: Proxy evidence for an el nino-like response to volcanic forcing. Nature, 426 (6964), 274–278.

Allan, R. P., C. Liu, N. G. Loeb, M. D. Palmer, M. Roberts, D. Smith, and P.-L. Vidale, 2014: Changes in global net radiative imbalance 1985–2012. Geophysical research letters, 41 (15), 5588–5597.

Ammann, C. M., G. A. Meehl, W. M. Washington, and C. S. Zender, 2003: A monthly and latitudinally varying volcanic forcing dataset in simulations of 20th century climate. Geophysical Research Letters, 30 (12).

Anderson, J. L., V. Balaji, A. J. Broccoli, W. F. Cooke, T. L. Delworth, K. W. Dixon, L. J. Donner, K. A. Dunne, S. M. Freidenreich, and S. T. Garner, 2004: The new gfdl global atmosphere and land model am2–lm2: Evaluation with prescribed sst simulations. Journal of Climate, 17 (24), 4641–4673.

Balmaseda, M. A., K. E. Trenberth, and E. Källén, 2013: Distinctive climate signals in reanalysis of global ocean heat content. Geophysical Research Letters, 40 (9), 1754–1759.

Behringer, D., and Y. Xue, 2004: Evaluation of the global ocean data assimilation system at ncep: The pacific ocean. Proc. Eighth Symp. on Integrated Observing and Assimilation Systems for Atmosphere, Oceans, and Land Surface.

Bopp, L., L. Resplandy, J. C. Orr, S. C. Doney, J. P. Dunne, M. Gehlen, P. Halloran, C. Heinze, T. Ilyina, R. Seferian, and J. Tjiputra, 2013: Multiple stressors of ocean ecosystems in the 21st century: projections with cmip5 models. Biogeosciences, 10 (10), 6225–6245, doi:10.5194/bg-10-6225-2013, URL https://www.biogeosciences.net/10/6225/2013/.

Brovkin, V., S. J. Lorenz, J. Jungclaus, T. Raddatz, C. Timmreck, C. H. Reick, J. Segschneider, and K. Six, 2010: Sensitivity of a coupled climate-carbon cycle model to large volcanic eruptions during the last millennium. Tellus B, 62 (5), 674–681.

Clement, A. C., R. Seager, M. A. Cane, and S. E. Zebiak, 1996: An ocean dynamical thermostat. Journal of Climate, 9 (9), 2190–2196.

Danabasoglu, G., S. C. Bates, B. P. Briegleb, S. R. Jayne, M. Jochum, W. G. Large, S. Peacock, and S. G. Yeager, 2012: The ccsm4 ocean component. Journal of Climate, 25 (5), 1361–1389.

Delworth, T. L., V. Ramaswamy, and G. L. Stenchikov, 2005: The impact of aerosols on simulated ocean temperature and heat content in the 20th century. Geophysical Research Letters, 32 (24), doi:10.1029/2005GL024457, URL http://dx.doi.org/10.1029/ 2005GL024457, l24709.

Ding, Y., J. A. Carton, G. A. Chepurin, G. Stenchikov, A. Robock, L. T. Sentman, and J. P. Krasting, 2014: Ocean response to volcanic eruptions in coupled model intercomparison project 5 simulations. Journal of Geophysical Research: Oceans, 119 (9), 5622– 5637, doi:10.1002/2013JC009780, URL http://dx.doi.org/10.1002/ 2013JC009780.

Dunne, J. P., A. Gnanadesikan, J. L. Sarmiento, and R. D. Slater, 2010: Technical description of the prototype version (v0) of tracers of phytoplankton with allometric zooplankton (topaz) ocean biogeochemical model as used in the princeton ifmip model. Biogeosciences, 7 (Supplement).

Dunne, J. P., J. G. John, A. J. Adcroft, S. M. Griffies, R. W. Hallberg, E. Shevliakova, R. J. Stouffer, W. Cooke, K. A. Dunne, M. J. Harrison, and J. P. Krasting, 2012: Gfdls esm2 global coupled climate–carbon earth system models. part i: Physical formulation and baseline simulation characteristics. Journal of Climate, 25 (19), 6646– 6665.

Dunne, J. P., J. G. John, E. Shevliakova, R. J. Stouffer, J. P. Krasting, S. L. Malyshev, P. C. Milly, L. T. Sentman, A. J. Adcroft, W. Cooke, and K. A. Dunne, 2013: Gfdls esm2 global coupled climate– carbon earth system models. part ii: carbon system formulation and baseline simulation characteristics. Journal of Climate, 26 (7), 2247– 2267.

Dutton, E. G., and J. R. Christy, 1992: Solar radiative forcing at selected locations and evidence for global lower tropospheric cooling following the eruptions of el chichn and pinatubo. Geophysical Research Letters, 19 (23), 2313–2316, doi:10.1029/92GL02495, URL http://dx.doi.org/10.1029/92GL02495.

Eddebbar, Y. A., M. C. Long, L. Resplandy, C. Rödenbeck, K. B. Rodgers, M. Manizza, and R. F. Keeling, 2017: Impacts of enso on air-sea oxygen exchange: observations and mechanisms. Global Biogeochem. Cycles, doi:10.1002/2017gb005630.

Emile-Geay, J., R. Seager, M. A. Cane, E. R. Cook, and G. H. Haug, 2008: Volcanoes and enso over the past millennium. Journal of Climate, 21 (13), 3134–3148, doi:10.1175/2007JCLI1884. 1, URL https://doi.org/10.1175/2007JCLI1884.1, https://doi.org/10. 1175/2007JCLI1884.1.

Feely, R. A., J. Boutin, C. E. Cosca, Y. Dandonneau, J. Etcheto, H. Y. Inoue, M. Ishii, C. Le Quéré, D. J. Mackey, M. McPhaden, and N. Metzl, 2002: Seasonal and interannual variability of co 2 in the equatorial pacific. Deep Sea Research Part II: Topical Studies in Oceanography, 49 (13), 2443–2469.

Frölicher, T. L., F. Joos, G.-K. Plattner, M. Steinacher, and S. C. Doney, 2009: Natural variability and anthropogenic trends in oceanic oxygen in a coupled carbon cycleclimate model ensemble. Global Biogeochemical Cycles, 23 (1), n/a–n/a, doi:10.1029/2008GB003316, URL http://dx.doi.org/10.1029/2008GB003316, gB1003.

Frölicher, T. L., F. Joos, and C. C. Raible, 2011: Sensitivity of atmospheric co2 and climate to explosive volcanic eruptions. Biogeosciences, 8 (8), 2317, copyright - Copyright Copernicus GmbH 2011; Last updated - 2011-10-05.

Frölicher, T. L., F. Joos, C. C. Raible, and J. L. Sarmiento, 2013: Atmospheric co2 response to volcanic eruptions: The role of enso, season, and variability. Global Biogeochemical Cycles, 27 (1), 239–251, doi: 10.1002/gbc.20028, URL http://dx.doi.org/10.1002/gbc.20028.

Gill, A., 1980: Some simple solutions for heat-induced tropical circulation. Quarterly Journal of the Royal Meteorological Society, 106 (449), 447–462.

Gleckler, P. J., K. M. AchutaRao, J. M. Gregory, B. D. Santer, K. E. Taylor, and T. M. L. Wigley, 2006: Krakatoa lives: The effect of volcanic eruptions on ocean heat content and thermal expansion. Geophys. Res. Lett., 33, L17 702, doi:http://dx.doi.org/10.1029/ 2006GL026771.

Griffies, S. M., M. Schmidt, and M. Herzfeld, 2009: Elements of mom4p1. GFDL Ocean Group Tech. Rep, 6, 444.

Hamme, R. C., P. W. Webley, W. R. Crawford, F. A. Whitney, M. D. DeGrandpre, S. R. Emerson, C. C. Eriksen, K. E. Giesbrecht, J. F. Gower, M. T. Kavanaugh, and M. A. Peña, 2010: Volcanic ash fuels anomalous plankton bloom in subarctic northeast pacific. Geophysical Research Letters, 37 (19), doi:10.1029/2010GL044629, URL http:// dx.doi.org/10.1029/2010GL044629, l19604.

Huang, B., Y. Xue, D. Zhang, A. Kumar, and M. J. McPhaden, 2010: The ncep godas ocean analysis of the tropical pacific mixed layer heat budget on seasonal to interannual time scales. Journal of Climate, 23 (18), 4901–4925.

Hunke, E., W. Lipscomb, A. Turner, N. Jeffery, and S. Elliott, 2008: Cice: the los alamos sea ice model, documentation and software, version 4.0. los alamos national laboratory tech. rep. Tech. rep., LA- CC-06-012.

Hurrell, J. W., M. M. Holland, P. R. Gent, S. Ghan, J. E. Kay, P. J. Kushner, J. F. Lamarque, W. G. Large, D. Lawrence, K. Lindsay, and W. H. Lipscomb, 2013:

The community earth system model: a framework for collaborative research. Bulletin of the American Meteorological Society, 94 (9), 1339–1360.

Ito, T., S. Minobe, M. C. Long, and C. Deutsch, 2017: Upper ocean o2 trends: 19582015. Geophysical Research Letters, 44 (9), 4214– 4223, doi:10.1002/2017GL073613, URL http://dx.doi.org/10.1002/ 2017GL073613, 2017GL073613.

Kay, J. E., C. Deser, A. Phillips, A. Mai, C. Hannay, G. Strand, J. M. Arblaster, S. C. Bates, G. Danabasoglu, J. Edwards, and M. Holland, 2014: The Community Earth System Model (CESM) Large Ensemble Project: A Community Resource for Studying Climate Change in the Presence of Internal Climate Variability. Bull. Amer. Meteor. Soc., doi:10.1175/BAMS-D-13-00255.1.

Keeling, R., and A. Manning, 2014: Studies of recent changes in atmospheric o2 content. Treatise on Geochemistry, 385–404, doi: 10.1016/b978- 0- 08- 095975- 7.00420- 4.

Keeling, R. F., A. Körtzinger, and N. Gruber, 2010: Ocean deoxygenation in a warming world.

Keeling, R. F., R. P. Najjar, M. L. Bender, and P. P. Tans, 1993: What atmospheric oxygen measurements can tell us about the global carbon cycle. Global Biogeochemical Cycles, 7 (1), 37–67.

Khodri, M., T. Izumo, J. Vialard, S. Janicot, C. Cassou, M. Lengaigne, J. Mignot, G. Gastineau, E. Guilyardi, N. Lebas, and A. Robock, 2017: Tropical explosive volcanic eruptions can trigger el niño by cooling tropical africa. Nature Communications, 8 (1), 778.

Landschützer, P., N. Gruber, F.A. Haumann, C. Rödenbeck, D.C. Bakker, S. Van Heuven, M. Hoppema, N. Metzl, C. Sweeney, T. Takahashi, and B. Tilbrook, 2015: The reinvigoration of the southern ocean carbon sink. Science, 349 (6253), 1221–1224.

Langmann, B., K. Zaksek, M. Hort, and S. Duggen, 2010: Volcanic ash as fertiliser for the surface ocean. Atmospheric Chemistry and Physics, 10 (8), 3891–3899, doi:10.5194/acp-10-3891-2010, URL https://www.atmos-chem-phys.net/10/3891/2010/.

Li, J., S. P. Xie, E. R. Cook, M. S. Morales, D. A. Christie, N. C. Johnson, F. Chen, R. D'Arrigo, A. M. Fowler, X. Gou, and K. Fang, 2013: El Niño modulations over the past seven centuries. Nature Climate Change, 3 (9), 822–826.

Liu, C., R. P. Allan, P. Berrisford, M. Mayer, P. Hyder, N. Loeb, D. Smith, D., P. L. Vidale, and J. M. Edwards, 2015: Combining satellite observations and reanalysis energy transports to estimate global net surface energy fluxes 1985–2012. Journal of Geophysical Research: Atmospheres, 120 (18), 9374–9389.

Liu, F., J. Li, B. Wang, J. Liu, T. Li, G. Huang, and Z. Wang, 2017: Divergent el nin˜o responses to volcanic eruptions at different latitudes over the past millennium. Climate Dynamics, 1–14.

Long, M. C., C. A. Deutsch, and T. Ito, 2016: Finding forced trends in oceanic oxygen. Global Biogeochem. Cycles, 30, doi:10.1002/ 2015GB005310.

Long, M. C., K. Lindsay, S. Peacock, J. K. Moore, and S. C. Doney, 2013: Twentieth-century oceanic carbon uptake and storage in cesm1 (bgc). Journal of Climate, 26 (18), 6775–6800.

Lovenduski, N. S., N. Gruber, S. C. Doney, and I. D. Lima, 2007: Enhanced co2 outgassing in the southern ocean from a positive phase of the southern annular mode. Global Biogeochemical Cycles, 21 (2).

Maher, N., S. McGregor, M. H. England, and A. S. Gupta, 2015: Effects of volcanism on tropical variability. Geophysical Research Letters, 42 (14), 6024–6033, doi:10.1002/2015GL064751, URL http: //dx.doi.org/10.1002/2015GL064751, 2015GL064751.

Mann, M. E., M. A. Cane, S. E. Zebiak, and A. Clement, 2005: Volcanic and solar forcing of the tropical pacific over the past 1000 years. Journal of Climate, 18 (3), 447–456, doi:10.1175/JCLI-3276.1, URL https://doi.org/10.1175/JCLI-3276.1, https://doi.org/10.1175/ JCLI- 3276.1.

McGregor, S., and A. Timmermann, 2011: The effect of explosive tropical volcanism on enso. Journal of Climate, 24 (8), 2178– 2191, doi:10.1175/2010JCLI3990.1, URL https://doi.org/10.1175/ 2010JCLI3990.1, https://doi.org/10.1175/2010JCLI3990.1.

McKinley, G. A., D. J. Pilcher, A. R. Fay, K. Lindsay, M. C. Long, and N. Lovenduski, 2016: Timescales for detection of trends in the ocean carbon sink. Nature, 530, 469–472, doi:10.1038/nature16958.

Moore, J. K., K. Lindsay, S. C. Doney, M. C. Long, and K. Misumi, 2013: Marine ecosystem dynamics and biogeochemical cycling in the community earth system model [cesm1 (bgc)]: Comparison of the 1990s with the 2090s under the rcp4. 5 and rcp8. 5 scenarios. Journal of Climate, 26 (23), 9291–9312.

Ohba, M., H. Shiogama, T. Yokohata, and M. Watanabe, 2013: Impact of strong tropical volcanic eruptions on enso simulated in a coupled gcm. Journal of Climate, 26 (14), 5169–5182, doi:10.1175/JCLI- D- 12- 00471.1, URL https://doi.org/10.1175/ JCLI-D-12-00471.1, https://doi.org/10.1175/JCLI-D-12-00471.1.

Pollack, J. B., O. B. Toon, C. Sagan, A. Summers, B. Baldwin, and W. Van Camp, 1976: Volcanic explosions and climatic change: A theoretical assessment. Journal of Geophysical Research, 81 (6), 1071–1083, doi:10.1029/JC081i006p01071, URL http://dx.doi.org/ 10.1029/JC081i006p01071.

Predybaylo, E., G. L. Stenchikov, A. T. Wittenberg, and F. Zeng, 2017: Impacts of a pinatubo-size volcanic eruption on enso. Journal of Geophysical Research: Atmospheres, 122 (2), 925–947.

Rampino, M. R., and S. Self, 1982: Historic eruptions of tambora (1815), krakatau (1883), and agung (1963), their stratospheric aerosols, and climatic impact. Quaternary Research, 18 (2), 127143, doi:10.1016/0033- 5894(82)90065- 5.

Reynolds, R. W., N. A. Rayner, T. M. Smith, D. C. Stokes, and W. Wang, 2002: An improved in situ and satellite sst analysis for climate. Journal of climate, 15 (13), 1609–1625.

Robock, A., 2000: Volcanic eruptions and climate. Reviews of Geophysics, 38 (2), 191–219, doi:10.1029/1998RG000054, URL http: //dx.doi.org/10.1029/1998RG000054.

Rödenbeck, C., C. Le Quéré, M. Heimann, and R. Keeling, 2008: Interannual variability in oceanic biogeochemical processes inferred by inversion of atmospheric o2/n2 and co2 data. Tellus B, 60 (5), 685– 705.

Rödenbeck, C., D. C. Bakker, N. Metzl, A. Olsen, C. L. Sabine, N. Cassar, F. Reum, R. F. Keeling, and M. Heimann, 2014: Interannual sea-air co2 flux variability from an observation-driven ocean mixed-layer scheme. Biogeosciences Discussions, 11, 3167–3207.

Rodgers, K., J. Lin, and T. Frölicher, 2015: Emergence of multiple ocean ecosystem drivers in a large ensemble suite with an earth system model. Biogeosciences, 12 (11), 3301.

Sanchez, S., C. Charles, J. Carriquiry, and J. Villaescusa, 2016: Two centuries of coherent decadal climate variability across the pacific north american region. Geophysical Research Letters, 43 (17), 9208– 9216.

Sarmiento, J., 1993: Atmospheric CO2 Stalled. Nature, 365 (6448), 697–698, doi:10.1038/365697a0.

Sato, M., J. E. Hansen, M. P. McCormick, and J. B. Pollack, 1993: Stratospheric aerosol optical depths, 1850–1990. Journal of Geophysical Research: Atmospheres, 98 (D12), 22 987–22 994.

Schmidtko, S., L. Stramma, and M. Visbeck, 2017: Decline in global oceanic oxygen content during the past five decades. NATURE, 542 (7641), 335+.

Segschneider, J., A. Beitsch, C. Timmreck, V. Brovkin, T. Ilyina, J. H. Jungclaus, S. J. Lorenz, K. D. Six, and D. Zanchettin, 2013: Impact of an extremely large magnitude volcanic eruption on the global climate and carbon cycle estimated from ensemble earth system model simulations. Biogeosciences, 10, 669–687.

Severinghaus, J. P., 1995: Studies of the terrestrial o 2 and carbon cycles in sand dune gases and in biosphere 2. Ph. D. thesis, Columbia University.

Stenchikov, G., T. L. Delworth, V. Ramaswamy, R. J. Stouffer, A. Wittenberg, and F. Zeng, 2009: Volcanic signals in oceans. Journal of Geophysical Research: Atmospheres, 114 (D16), doi:10.1029/2008JD011673, URL http://dx.doi.org/10.1029/ 2008JD011673, d16104.

Stenchikov, G. L., I. Kirchner, A. Robock, H.-F. Graf, J. C. Antua, R. G. Grainger, A. Lambert, and L. Thomason, 1998: Radiative forcing from the 1991 mount pinatubo volcanic eruption. Journal of Geophysical Research: Atmospheres, 103 (D12), 13837–13857, doi: 10.1029/98JD00693, URL http://dx.doi.org/10.1029/98JD00693.

Stephens, B. B., R. F. Keeling, M. Heimann, K. D. Six, R. Murnane, and K. Caldeira, 1998: Testing global ocean carbon cycle models using measurements of atmospheric o2 and co2concentration. Global Biogeochem. Cycles, 12 (2), 213–230, doi:10.1029/97gb03500.

Stevenson, S., J. T. Fasullo, B. L. Otto-Bliesner, R. A. Tomas, and C. Gao, 2017: Role of eruption season in reconciling model and proxy responses to tropical volcanism. Proceedings of the National Academy of Sciences, 114 (8), 1822–1826, doi:10.1073/ pnas.1612505114.

Wanninkhof, R., 1992: Relationship between wind speed and gas exchange over the ocean. J. Geophys. Res., 97 (C5), 7373–7382, doi: 10.1029/92JC00188.

Xie, S.-P., C. Deser, G. A. Vecchi, J. Ma, H. Teng, and A. T. Wittenberg, 2010: Global warming pattern formation: Sea surface temperature and rainfall. Journal of Climate, 23 (4), 966–986.

Yan, X.-H., T. Boyer, K. Trenberth, T. R. Karl, S.-P. Xie, V. Nieves, K.-K. Tung, and D. Roemmich, 2016: The global warming hiatus: Slowdown or redistribution? Earth's Future, 4 (11), 472–482.

Zanchettin, D., C. Timmreck, H.-F. Graf, A. Rubino, S. Lorenz, K. Lohmann, K. Kru¨ger, and J. Jungclaus, 2012: Bi-decadal variability excited in the coupled ocean–atmosphere system by strong tropical volcanic eruptions. Climate Dynamics, 39 (1-2), 419–444.

CHAPTER 4: ATMOSPHERIC OXYGEN AND CARBON CONSTRAINTS ON DECADAL TRENDS IN OCEANIC HEAT UPTAKE

Abstract

Global mean surface temperature (GMST) warming slowed down during the past decade and a half (~ 2000-2015). A leading explanation for this surface warming "hiatus" is the redistribution of energy within the climate system through intensified ocean heat uptake. Estimates of ocean heat uptake, however, differ significantly prior to global Argo coverage (~2006). Here we explore the use of continuous global time series of Atmospheric Potential Oxygen ($APO=O_2+1.1*CO_2$) to infer decadal changes in ocean heat uptake, based on potential negative coupling between air-sea exchanges of heat and APO. Observations show that APO is declining at a slower rate than is expected from fossil fuel combustion and oceanic uptake of anthropogenic carbon. This anomalous excess of APO, known as $APO_{Climate}$ and calculated as the difference between expected and observed APO, is driven by the outgassing effects of ocean warming, and has been recently introduced as an independent tracer for ocean heat uptake. Observations show a decadal trend towards weakened outgassing of $APO_{Climate}$ since 2000, in direct contrast to what is expected from enhanced ocean heat uptake during the hiatus. This inference, however, assumes that heat and APO fluxes are tightly and negatively coupled on interannual to decadal timescales. We examine this relation in coupled and hindcast simulations of CESM and GFDL, and find a weak coupling globally under natural variability. The weakening of this global relationship arises mainly due to equatorial dynamics, which positively couple heat and APO

exchange in the tropical Pacific, while APO and heat exchange remains negative at higher latitudes. These spatially distinct relationships suggest that APO trends are inconsistent with a dominant role for enhanced ocean heat uptake in the North Atlantic during the hiatus, but leave open the possibility for intensified sequestration of heat in the tropics, where O_2 and heat fluxes are modulated in the same direction. Due to different ratios of APO-to-heat exchange in each basin and potential regional cancellation effects in the global mean, the observed slowdown in the outgassing of $APO_{Climate}$ during the hiatus also allows for the possibility for no net change or even reduced rates of ocean heat uptake globally during this period.

1. Introduction

Global mean surface temperature (GMST) warming significantly slowed down at the turn of the 21st century, despite the continued build-up of carbon dioxide (CO_2) in the atmosphere (Trenberth and Fasullo, 2010). The decadal persistence of this surface warming slowdown (~2000-2015), termed the "hiatus", and its divergence from model projections, raised broad and profound questions for quantifying climate sensitivity and the planetary energy imbalance (e.g., the concept of the "missing heat") and the attribution of observed surface warming trends in past decades (Trenberth and Fasullo, 2010; 2014). The hiatus also has important implications for international climate policy (Victor and Kennel, 2014), which continue to rely on GMST as a major climate indicator and policy target (e.g., the 1.5ºC and 2ºC targets within the Paris Agreement). Although the recent large El Niño event of 2015-2016 seems to have put an end to the hiatus, the driving cause for this warming pause remains widely debated.

A leading explanation for this slowdown in surface warming involves the redistribution of energy within the climate system through accelerated ocean heat uptake (Meehl et al., 2011; 2013; Watanabe et al., 2013; Balmaseda et al., 2013). The location and driving mechanisms for this enhanced ocean heat uptake, however, remain ambiguous (Yan et al., 2017). Numerous studies, for instance, have argued for enhanced heat uptake over the low latitudes, where intensification of the easterlies associated with a negative phase of the Inter-decadal Pacific Oscillation (IPO) accelerated the sequestration of heat in the tropical Pacific thermocline (Meehl et al., 2011; 2013; Balmaseda et al., 2013; England et al., 2014) and the Indian ocean (Nieves et al., 2015; Liu et al., 2016). Using in-situ ocean observations and data assimilation methods, others have pointed instead at intensified ocean heat uptake at higher latitude basins, where decadal variability associated with the Meridional Overturning Circulation has supposedly led to more ocean heat uptake in the North Atlantic and the Southern Ocean (Chen and Tung, 2014; Drijfhout et al., 2014).

Observational estimates of the oceanic heat content (OHC), however, differ substantially prior to global Argo coverage (~2006) due to large uncertainties associated with substantial sampling gaps and instrumentation biases (Abraham et al., 2013), limiting the degree to which definitive conclusions can be drawn from in-situ observations and data assimilation estimates of OHC in studies of the hiatus. Further, models exhibit hiatus events in the absence of enhanced ocean heat uptake (Kanel et al., 2017). Theoretical and modeling evidence were also recently proposed for reduced ocean heat uptake during hiatus periods, whereby planetary energy imbalance and

GMST can be decoupled under natural variability, in contrast to their assumed tight coupling under anthropogenic forcing (Xie et al., 2016). A decadal-scale enhancement of low-level clouds, for instance, may act to reduce shortwave energy at the surface, driving GMST cooling and reduced ocean heat uptake simultaneously.

We evaluate here the role of changes in ocean heat uptake rates during the hiatus using a method that is independent of in-situ ocean observations or satellites, based on global continuous measurements of atmospheric $\delta(O_2/N_2)$ (referred to herein as atmospheric O_2) and CO_2 (Resplandy et al., submitted to *Nature,* 2017, referred to herein as "Resplandy et al., submitted"). This method is based on the well-known negative relationship between gas solubility and ocean temperature. Simply put, warm water holds less gas than colder water; as the ocean warms, atmospheric gas content is expected to increase (Keeling et al., 2004). To isolate oceanic effects from the influence of terrestrial processes, atmospheric O_2 and CO_2 time series are combined into an "Atmospheric Potential Oxygen" tracer (Stephens et al., 1998), calculated as: $APO = O_2 + 1.1*CO_2$, where the sum of O_2 and CO_2 using terrestrial oxidative ratio of 1.1 (Severinghaus, 1995) renders APO largely insensitive to terrestrial biospheric effects. Correcting for the influence of fossil fuel combustion, anthropogenic aerosol deposition, and the long-term trend in ocean uptake of anthropogenic carbon on atmospheric O_2 and CO_2 yields an APO residual or "$APO_{Climate}$" that reflects primarily the combined oceanic fluxes of O_2 and CO_2 due to ocean warming and other ocean processes (Keeling and Manning, 2014; Resplandy et al., submitted). On long timescales (multidecadal-to-centuries), changes in ocean biological and circulation

processes lead to opposing exchanges of O_2 and CO_2 due to their tight coupling in photosynthesis and respiration, analogously to land processes. Ocean warming, on the other hand, drives outgassing in both O_2 and CO_2 due to the temperature dependence of solubility in both gases. This reinforcing effect of temperature along with the cancellation effect of biological processes allows $APO_{Climate}$ to behave similarly to an inert gas, controlled primarily by ocean heating and cooling (Resplandy et al., 2016). This emerging strong relationship between the oceanic heat content and $APO_{Climate}$ is further supported by a well-constrained relationship from models and observed distributions of O_2 and DIC in the ocean's interior (Resplandy et al., 2016).

Resplandy and colleagues show that $APO_{Climate}$ has increased at a rate of 1.2 +/-0.5 permeg.yr^{-1} over the APO observations period (1991-2015). Using a model-derived APO-to-heat ratio of -3.8 nmol.J^{-1}, they estimate a long-term ocean warming rate of 1.3 +/-0.3 10^{22} J.y^{-1}, which corresponds to a planetary energy imbalance of 0.8 +/-0.2 W.m^{-2}, a value that is at the higher end, but within the uncertainty range, of estimates from in-situ ocean observations and satellites. The APO method provides a much needed estimate of ocean warming that is independent of ocean temperature measurements, thus improving confidence in those measurements. This study, however, leaves open the question of how APO and heat are coupled on time-scale shorter than ~25 years.

Here, we examine decadal trends in $APO_{Climate}$ in light of recent claims that accelerated ocean heat uptake led to the hiatus. The relationship between heat and APO exchange, however, has only been established for the long-term trends in ocean

warming (Resplandy et al., submitted), and their coupling due to externally forced (e.g., volcanoes) and unforced (e.g., ENSO) natural variability on interannual-to-decadal timescales has not been previously evaluated. This is especially relevant given the suggested central role for natural variability in driving the hiatus, whereby La Niña-like conditions (i.e. negative phase of the IPO) have been linked to the observed spatial anomalies in surface air and sea surface temperatures and the flattening of global mean temperature since 2000 (Kosaka and Xie 2013; Meehl et al., 2011) while prior decades were marked by more frequent El Niño events and a positive phase of the IPO. The first decade of the APO record (i.e., the 1990's) coincided with the June 1991 eruption of Pinatubo and the El Niño of 1997-1998, respectively the largest volcanic and ENSO events of the last 100 years, while the second decade of the APO record (i.e., 2000's) was dominated by La Niña-like conditions. Modes of natural variability such as ENSO and volcanic eruptions are known to have substantial and complex impacts on air-sea heat, O_2 and CO_2 exchange (McKinley et al., 2003; 2004; Resplandy et al., 2015; Frölicher et al., 2009; 2011; Eddebbar et al., 2017), and the subsequent coupling between heat and APO exchange due to these phenomena is not well understood. Finally, carbonate chemistry significantly buffers CO_2 flux variability on seasonal-to-interannual timescales (Keeling and Severinghaus, 2000), and thus the biological cancellation effect and the inert gas-like behavior of APO is likely to be reduced, as O_2 variability tends to dominate APO on shorter timescales.

In this study, we examine changes in decadal trends in the $APO_{Climate}$ and evaluate the relationship between air-sea heat and APO exchange in forced vs.

unforced variability on interannual-to-decadal timescales. Similar to Chapter 3, the Large Ensemble (LE) experiment of CESM and GFDL is used to isolate the structure of relationships between air-sea heat and APO exchanges arising from the "forced" component of variability, i.e., that due to increasing greenhouse gases and volcanic eruptions (LE mean response), from the coupling between heat and APO exchanges driven by internal variability. The response due purely to internal variability is evaluated in unforced control integrations (no anthropogenic or volcanic forcing used), which simulate the natural exchange of heat and APO due to internal variability of the climate system. To provide context for the analysis of observed $APO_{Climate}$ trends during the hiatus, we also examine a hindcast simulation of CESM over the 1960-2015 period. Finally, we explore mechanisms driving the coupling of heat and APO focusing on the tropical Pacific, and conclude with a brief summary.

2. Methods

a) Observations

In this chapter, we isolate APO variability due to ocean processes using an approach that is similar to Resplandy et al. (submitted), but using monthly resolution rather than annual means evaluated by Resplandy and colleagues. A global mean APO (APO_{GLB}) is calculated using regionally-weighted atmospheric O_2 and CO_2 time series from Scripps O_2 Network stations that span both the pre-hiatus and hiatus periods (1991-2016). These include the La Jolla, CA (32.9°N, 117°W), Alert, Canada (82.5°N, 62.5°W), and Cape Grim, Australia (40.5°S, 144.5°E) stations (Figure 2.2). O_2 and

CO_2 time series from other locations in the Scripps O_2 Network are not used in the global estimate due to their shorter observational periods, as detailed in the methods section of Chapter 2. Given the relatively fast timescale of mixing in the atmosphere (~1 year), the decadal trends evaluated here are unlikely to be sensitive to the number of stations used in the global APO mean. Atmospheric O_2 and CO_2 measurements at each location are obtained from flask samples collected twice a month during the January 1991 through December 2015 period, and are analyzed using interferometry for the $\delta(O_2/N_2)$ and an infrared analyzer for CO_2 at the Scripps Atmospheric Oxygen Program laboratory, respectively (Keeling and Manning, 2014).

Fossil fuel and cement production influence on APO_{GLB} are accounted for using fuel-specific oxidative ratios (Keeling, 1988) and fossil fuel consumption estimates from Boden et al. (2016) and Le Quéré et al. (2016). We correct for the influence of ocean uptake of anthropogenic carbon on APO_{GLB} using the pulse response function method of Joos et al. (1996), which is based on the HILDA model scaled by the integrated carbon uptake estimate of Sabine et al. (2004), following Rafelski et al. (2009). Figure 4.1a shows that this method achieves strikingly similar estimates as more complex methods such as the ocean data assimilation of Devries (2014) used in the Resplandy et al. (submitted) method, and coupled general circulation models like CESM and GFDL. We note that the influence of climate variability on ocean processes driving changes in air-sea carbon flux is not included in the ocean carbon uptake correction, since this is considered under the "natural" oceanic CO_2 flux, which contributes to $APO_{Climate}$. Similarly to the Resplandy method,

the influence of atmospheric deposition and fertilization effects of anthropogenic aerosols on APO is accounted for using simulations of the Institut Pierre Simon LaPlace (IPSL) ocean model with and without anthropogenic aerosols inputs. This term exerts a relatively minor influence on the APO trend (Figure 4.1b).

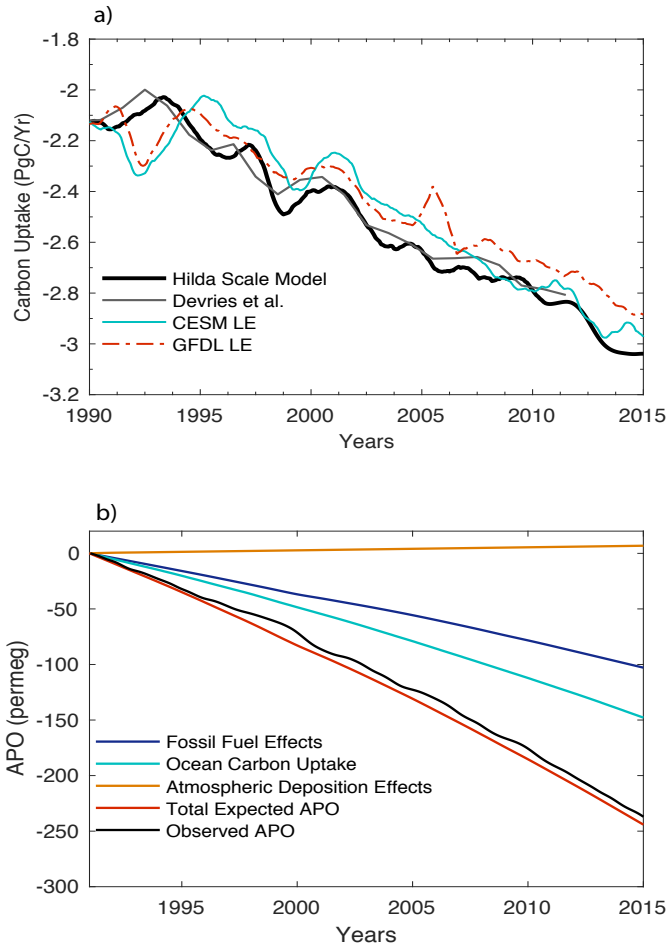

Figure 4.1. a) Estimates of anthropogenic carbon uptake by the ocean using the HILDA model pulse response function (black thick line) of Joos et al. (1996) scaled following Rafelski et al. (2009), data assimilation method (grey thin line) of Devries (2014), and CESM (cyan) and GFDL (red dashed) LE means. b) APO_{GLB} trends induced by fossil fuel effects (blue), ocean carbon uptake (cyan), and atmospheric deposition of aerosols (orange), and their total net effect on APO_{GLB} (red), along with observed APO_{GLB} (black).

The contribution of each of these processes to the APO_{GLB} trend is illustrated in Figure 4.1b, which shows that the total sum of fossil fuel burning, anthropogenic carbon uptake by the ocean, and atmospheric aerosol deposition result in an expected APO_{GLB} downward trend (red line) that is larger than observed (black line). The difference between expected and observed APO_{GLB}, referred to by Resplandy et al. (submitted) as "$APO_{Climate}$" shows a long-term increase that is in line with the long-term effects of ocean warming on O_2 and CO_2, as previously suggested in Keeling and Manning (2014). Large uncertainties accompany the corrections of fossil fuel burning, atmospheric deposition, and ocean uptake of anthropogenic carbon, in addition to observational uncertainty due to random and systematic error. These are estimated in Resplandy et al. (submitted) using a combination of an autoregressive model and a Monte Carlo approach. The global APO flux (F_{APO}), which represents the weighted sum of air-sea O_2, CO_2, and N_2 fluxes (see next section), can be estimated from $APO_{Climate}$ as $F_{APO} = M_{ATM}\, X_{O_2} \frac{dAPO_{Climate}}{dt}$, where M_{ATM} represents the number of moles in the atmosphere (1.8×10^{20} mol), and X_{O2} represents the atmospheric mixing ratio of O_2 (0.2095).

b) Models

To evaluate the relation between air-sea heat and APO exchange due to externally forced and internally generated natural variability, we evaluate APO and heat fluxes from the CESM LE experiments (Kay et al., 2014). The CESM LE is forced by historically observed CO_2 concentrations (1920-2005) and the RCP8.5 scenario (2006-2100) to simulate anthropogenic forcing, and uses the Amman et al.

(2003) volcanic AOD dataset to simulate volcanic forcing. As detailed in Chapter 3, averaging a large number of ensemble members isolates the impacts of anthropogenic and volcanic forcing in the LE mean since volcanic and anthropogenic forcing are similar across the ensemble, while modes of natural variability are randomized across ensemble members, due to the use of slightly different initial conditions (Deser et al., 2012).

The same CESM LE configuration used in Chapter 3 is employed here, namely the 1ºx1º nominal resolution of CESM version 1 which couples the Community Atmosphere Model, version 5 (Hurrell et al., 2013) to the Parallel Ocean Program, version 2 (POP2; Danabasoglu et al., 2012), and the Los Alamos Sea Ice Model, version 4 (Hunke and Lipscomb, 2008). Ocean biogeochemistry is coupled to POP2 using the Biogeochemical Elemental Cycling model (Moore et al., 2013). The LE mean is calculated for heat, APO, O_2, and CO_2 fluxes and other physical variables by averaging across 30 ensemble members for the period of 1920-2100. All ensemble runs were initialized from a 600-year spin-up model solution and were forced with an identical observed CO_2 mixing ratio evolution. Each ensemble member was initially perturbed with a round-off level perturbation (10^{-14} K) to atmospheric surface temperatures, which randomizes modes of variability within a decade across ensembles (Kay et al., 2014). To evaluate the coupling between heat and APO fluxes due to internal variability, we evaluate a 200-year control (unforced) simulation from the CESM LE experiment, where no external forcing is used (i.e. no anthropogenic, solar, or volcanic forcing). The GFDL LE (also described in Chapter 3) and an

unforced control simulation of GFDL (Dunne et al., 2012; 2013) spanning a 150-year period are also evaluated for model comparison.

To examine the behavior of APO flux and its relation with ocean heat uptake within the specific context of the hiatus, we evaluate a hindcast simulation of CESM conducted using the CORE2 forcing protocol (Griffies et al., 2009) as detailed in Chapter 2 but extended here through December 2015 using the updated NCEP reanalysis product. We focus on the 1990-2015 period and examine changes in heat and APO fluxes, which are calculated similarly to Chapter 2, as: $F_{APO} = F_{O_2} + 1.1F_{CO_2} - \frac{X_{O_2}}{X_{N_2}}F_{N_2}$, where X_{O2} (0.2095) and X_{N2} (0.7815) represent the atmospheric mixing ratios of O_2 and N_2 respectively. $F_{N2,}$ the air-sea flux of Nitrogen (N_2), is calculated following the heat flux scaling formula of Keeling et al. (1993). N_2 fluxes have a minor influence on APO, acting to slightly buffer the net outgassing effects of O_2 and CO_2 on APO. Similarly to Chapter 3, a preindustrial or "natural" CO_2 flux is used to calculate APO, in order to isolate the effects of climate variability on the natural carbon cycle. Monthly anomalies are derived for all series by removing the long-term monthly mean. Leading modes of natural variability associated with ENSO and the IPO are calculated in the unforced simulation using the Niño3.4 index, and the 1st Empirical Orthogonal Function of 9-year low pass filtered SST over the Pacific basin, respectively. Mode indices are linearly regressed against anomalies in heat and APO fluxes to evaluate their signature on the coupling between heat and APO. Throughout this chapter, a positive anomaly in the air-sea flux of heat, O_2 or CO_2 indicate anomalous flux out of the ocean, while a negative flux denotes ocean uptake.

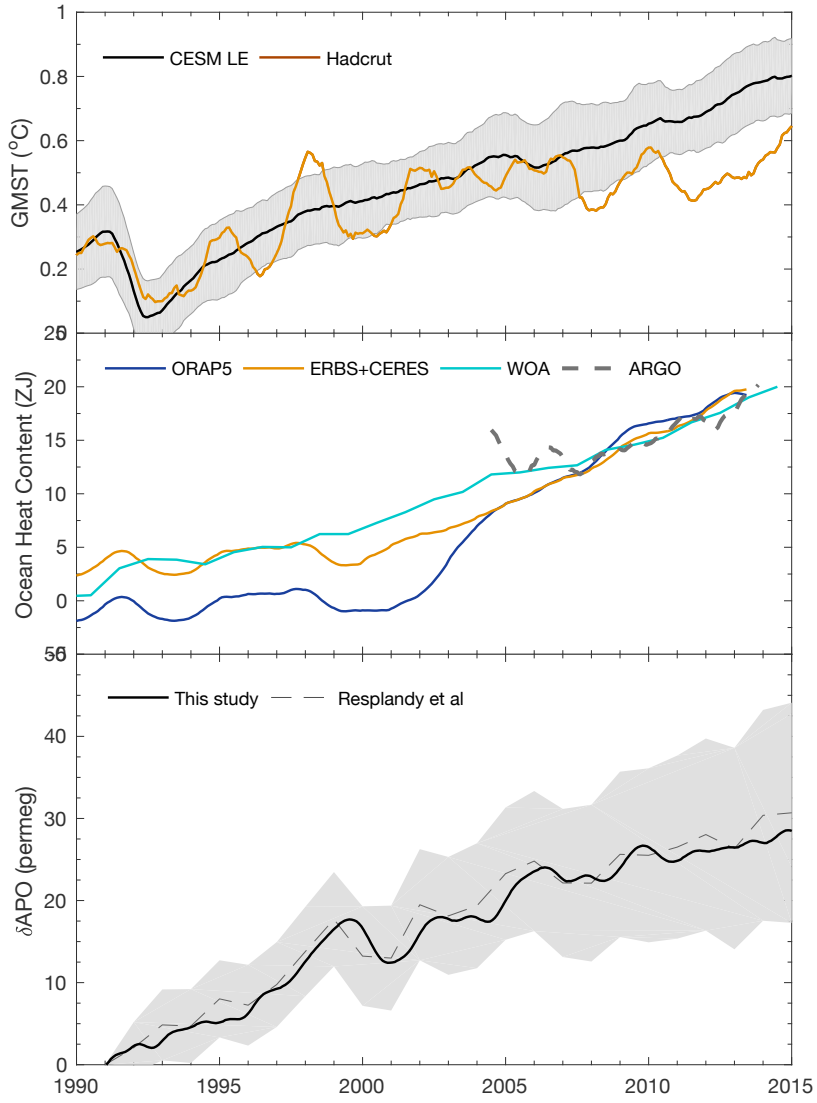

Figure 4.2. Observations during the January 1990-December 2014 period of a) global mean surface temperature (GMST) from the Hadcrut product (Morice et al., 2012; orange) vs. the CESM LE mean (black), where spread denotes 1σ across ensemble members; b) OHC estimates for the upper 0-2000 m ocean from the World Ocean Atlas product (cyan; Levitus et al., 2012), ORAP5 (navy blue; Zuo et al., 2017), Scripps Argo float (Roemmich et al., 2015) product (dashed grey), and CERES/ERBES-based ocean heating estimate (orange; Trenberth and Fasullo, 2014); and c) global $APO_{Climate}$ which represents the APO anomaly due to ocean warming and other ocean processes, accounting for the effects of fossil fuel combustion and cement production, anthropogenic ocean CO_2 uptake, and anthropogenic aerosol deposition (see Methods), using ocean carbon uptake estimates from Devries (2014) and annual mean APO time series in Resplandy et al. (submitted) and the scaled Hilda model ocean carbon estimate and monthly resolutions in this study. Shading indicates +/-2σ uncertainty as estimated in Resplandy et al. (submitted).

3. Results and Discussion

a) Observations

Figure 4.2 shows the $APO_{Climate}$, .i.e. the anomalous APO_{GLB} residual due to ocean processes, along with observed and simulated GMST and estimates of OHC from the World Ocean Atlas (WOA; Levitus et al., 2012), CERES-ERBES satellite-based energy imbalance scaled by 90% to reflect ocean heat uptake (Trenberth and Fasullo, 2014), and the Ocean Reanalysis Product, version 5 (ORAP5; Zuo et al., 2017). As noted in the introduction, estimates of OHC diverge substantially prior to global coverage of Argo floats (~2006). In line with Argo float observations, the long-term increase in $APO_{Climate}$ (1.19 permeg.yr^{-1} over the 1991-2014 period) suggests that the ocean continued to warm during the hiatus period, and that there is no pause in global planetary warming during this period. However, the rate of increase of $APO_{Climate}$ slows down by about 50% during the hiatus decade when compared to the previous decade. This slowdown in the $APO_{Climate}$ increase during a period of accelerated heat uptake is contrary to the expected coupling between APO and heat, whereby enhanced ocean heat uptake would drive larger APO release from the ocean.

To maintain consistency in decadal comparisons with other studies, we use the decadal periods adopted in Drijfhout et al. (2014) who synthesize estimate of changes in heat uptake rates during the hiatus from various reanalysis products (Table 4.1), using the January 1992 thru December 2000 period for the pre-hiatus or "warming" decade, and the January 2001 thru December 2009 period for the hiatus decade. Table 4.1 also summarizes the APO fluxes associated with decadal changes in heat uptake

rates from reanalysis products using the -3.8 $nmol.J^{-1}$ APO-to-heat ratio found in models by Resplandy et al. (submitted).

Table 4.1. Decadal change in ocean heat uptake rates (Drijfhout et al., 2014) and APO fluxes between the hiatus decade (2001-2009) and the pre-hiatus period (1992-2000). Expected APO change from each product are estimated using the -3.8$nmol.J^{-1}$ APO-to-heat flux ratio reported in Resplandy et al. (submitted), and inversely, the same ratio is used for estimating changes in ocean heat uptake from the observed change in the $APO_{Climate}$ trend.

	ERA-I	**CORE2**	**ORAP5**
Change in ocean heat uptake rate ($W.m^{-2}$)	0.80	0.60	1.10
$\Delta APO_{Climate}$ Expected ($Tmol.yr^{-1}$)	34.51	25.88	47.46
$\Delta APO_{Climate}$ Observed ($permeg.yr^{-1}$)	-0.49		
$\Delta APO_{Climate}$ Observed ($Tmol.yr^{-1}$)	-18.48		
Observed $\Delta APO_{Climate}$-derived Heat Uptake Rate Change ($W.m^{-2}$)	-0.29		

In all reanalysis products, Drijfhout et al. (2014) report enhanced ocean heat uptake of 0.6 to 1.1 $W.m^{-2}$ during the hiatus, corresponding to an expected enhanced APO outgassing of about 26 to 48 $Tmol.yr^{-1}$. In contrast, the observed decadal difference in $APO_{Climate}$ trends yields a reduced outgassing (or anomalous uptake) of -19 $Tmol.yr^{-1}$. This slowdown of $APO_{Climate}$ outgassing corresponds to a net reduced ocean heat uptake of about -0.3 $W.m^{-2}$, assuming a tight negative relationship (-3.8 $nmol.J^{-1}$) on interannual-to-decadal timescales between heat and APO.

The $APO_{Climate}$ uncertainties (2σ) estimated by Resplandy et al. (submitted) shown in Figure 4.2 are substantial and are dominated by uncertainties in fossil fuel consumption and ocean carbon uptake. A slowdown in the upward trend of $APO_{Climate}$ over the hiatus decade, for instance, may arise from fossil fuel correction biases due to underreporting of fossil fuel consumption over this period. A recent synthesis of SOCAT-based dataset (Landschützer et al., 2015) have suggested the oceanic carbon

sink may have intensified since ~2000 due to natural variability in the Southern Ocean. Such a change would be reflected in the $APO_{Climate}$ trends as a natural CO_2 flux contribution in the APO flux calculation, which is not well understood on decadal timescales. While underreporting of fossil fuel consumption during the hiatus or intensification in ocean carbon uptake may play a role in this counterintuitive decadal trend in $APO_{Climate}$, an even more pressing and important uncertainty is whether the same tightly negative relationship between heat and APO exists on these timescales. We, thus, evaluate next the coupling between heat and APO due to anthropogenic warming and volcanic cooling (i.e. "forced coupling"), and their emerging relationship due to natural variability (i.e. "unforced coupling").

b) Forced vs. Unforced Coupling of Air-sea Heat and APO Exchange

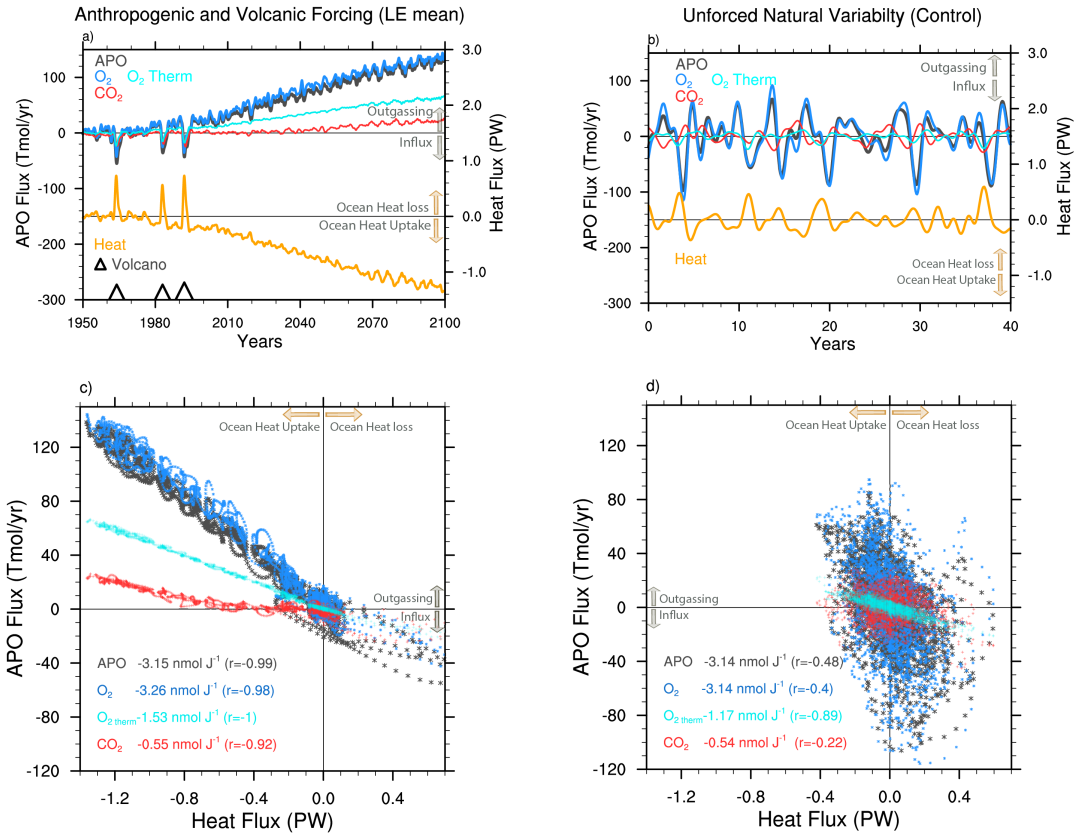

Figure 4.3. Coupling between air-sea heat and APO fluxes in forced vs. unforced simulations of CESM. Time series (a-b) and scatter (c-d) of globally integrated anomalies in APO (black), O_2 (blue), CO_2 (red), and thermal O_2 ($O_{2\,\mathrm{therm}}$) fluxes (cyan), vs. heat (orange) fluxes in the LE mean (left) and control run (right) of CESM. Also shown in c) and d) are linear regression coefficients (nmol.J^{-1}) representing APO-to-heat ratios, and correlation coefficients (r) between heat and gas fluxes. a) and c) are derived from the mean of the LE, while b) and d) represent flux anomalies from a single unforced simulation. Panel b) shows years 0-40 from a 200 years control simulation for clarity, while panel d) shows the scatter from the full simulation period. The LE mean series were smoothed with an 18-month low-pass filter, while the control run series were smoothed with 1.5-20-year band-pass filter to isolate interannual-to-decadal variability. A positive flux indicates anomalous flux out of the ocean, and vice versa, a negative flux indicates ocean uptake.

Figure 4.3 shows the relationship between global APO and heat fluxes in the CESM LE mean and a CESM control simulation. In the LE mean, anthropogenic warming leads to APO outgassing (Figure 4.3a), while volcanic cooling leads to uptake of APO (Agung, El Chichon, and Pinatubo eruptions represented as triangles in

Figure 4.3a). Figure 4.3c indicates a tightly negative linear relationship emerges under this forced setting (r^2=0.98), with an APO-to-heat flux ratio of about -3.15 nmol.J^{-1}, a value that is smaller but within the spread of the ratio of -3.8 +/-0.8 nmol.J^{-1} reported across models in Resplandy et al. (submitted). The components of the APO flux are also shown, indicating much larger outgassing of O_2 than CO_2, since thermal fluxes and biodynamical fluxes are reinforced in O_2, but largely cancel out for CO_2. The thermal component of O_2 accounts for about 50% of total O_2 outgassing.

In the unforced setting (Figure 4.3b and d), however, the strength of the relation between air-sea heat and APO exchange due to natural variability is reduced substantially (r^2=0.22). We note, for instance, periods of large APO variability that are not associated with major changes in heat flux (e.g., control simulation years 12-16 and 28-32 in Figure 4.3b). Note that the same axis scale is used in forced and unforced panels, which shows larger noise-to-anthropogenic signal in APO than for heat. This larger sensitivity of APO to internal variability processes is likely due to steeper vertical gradients in O_2 and DIC than for temperature. Similarly to the forced coupling, the relation between APO and heat fluxes is dictated mainly by O_2, though the thermal component of O_2 (cyan line in Figure 4.3b) plays a much weaker role in the unforced variability of APO.

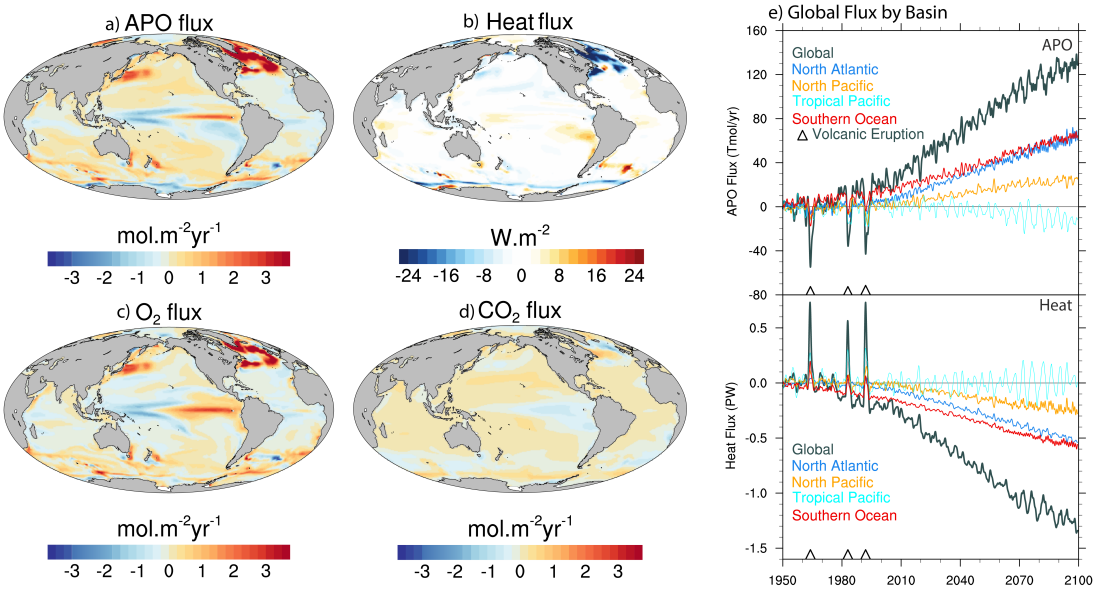

Figure 4.4. Air-sea flux anomalies of APO, O_2, CO_2 and heat due to anthropogenic forcing, shown as differences between the 2090-99 and 2000-09 decades in a) APO, b) heat, c) O_2, and d) CO_2 flux in the CESM LE mean. Panel e) shows globally integrated APO (black) and heat (orange) flux in the CESM LE mean, decomposed by dominant basins, including the north Atlantic (20ºN-70ºN), North Pacific (20ºN-70ºN), Tropical Pacific (20ºS-20ºN), and Southern Ocean (40ºS -90ºS).

Figure 4.4 shows the spatial patterns and regional contribution to the global flux of APO and heat due to anthropogenic warming, illustrated by decadal differences in anomalies in APO, O_2, CO_2 and heat fluxes between the beginning and the end of the 21st century in the CESM LE mean. Greenhouse gas radiative forcing drives heat uptake and APO outgassing primarily at higher latitude basins, with prominent roles for the Southern Ocean, north Atlantic, and to a smaller extent the north Pacific (Figure 4.4e). The spatial patterns of APO outgassing are dominated by O_2 outgassing (Figure 4.4c), which is in turn driven by reduced O_2 ventilation due to enhanced stratification during winter months and thermal outgassing due to warming effects on

gas solubility. CO_2 is also outgassed globally though at a smaller rate and with less pronounced spatial anomalies (Figure 4.4d). Thus, a major reason for the tight negative relation between heat and APO fluxes due to long-term warming is the dominance of high latitudes processes on the global flux (Figure 4.4e), where O_2 ventilation and thermal effects reinforce each other.

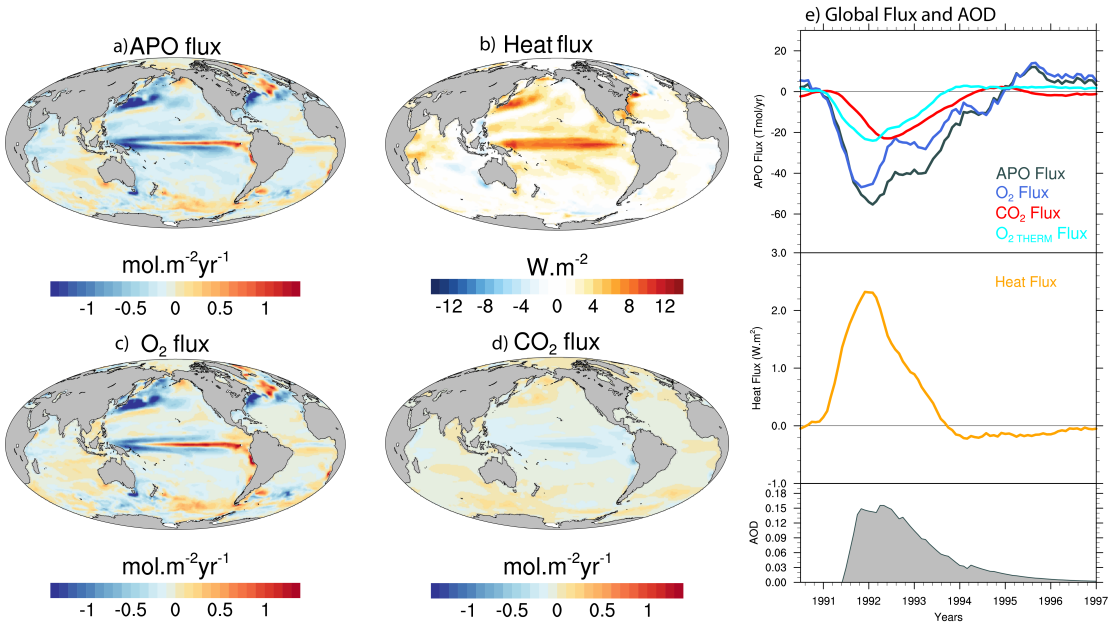

Figure 4.5. Air-sea flux anomalies of APO, O_2, CO_2 and heat due to volcanic forcing, shown as anomalies in the CESM LE mean in a) APO, b) Heat, e) O_2, and f) CO_2 flux following the Pinatubo eruption of June 1991. Panel e) shows globally integrated APO (black), O_2 (blue), thermal O_2 (cyan), and CO_2 (red) flux, global mean heat (orange) flux anomalies in the CESM LE mean and Aerosol Optical depth (AOD, grey shading). Spatial anomalies are calculated as the average difference between the 2-year period following Pinatubo and the 5-yr period prior to eruption.

Figure 4.5 highlights anomalies in APO and heat fluxes during the Pinatubo period (1991-1997) in the LE mean, noting similar responses and spatial patterns emerge in other tropical eruptions (see Figure 3.5). Following eruption, the oceanic

loss of heat primarily due to reduced shortwave fluxes via aerosol scattering leads to uptake of APO globally (Figure 4.5e). This uptake is driven by increased O_2 solubility due to thermal effects, intensified O_2 ventilation at high latitudes due to enhanced convection, and reduced natural outgassing of CO_2 in the tropical Pacific due to an El Niño-like ocean response. The reinforcing effects of net global O_2 and CO_2 uptake (Figure 4.5e) despite their negative correlation in space (Figure 4.5c-d) lead to strong negative coupling globally between heat and APO under volcanic forcing.

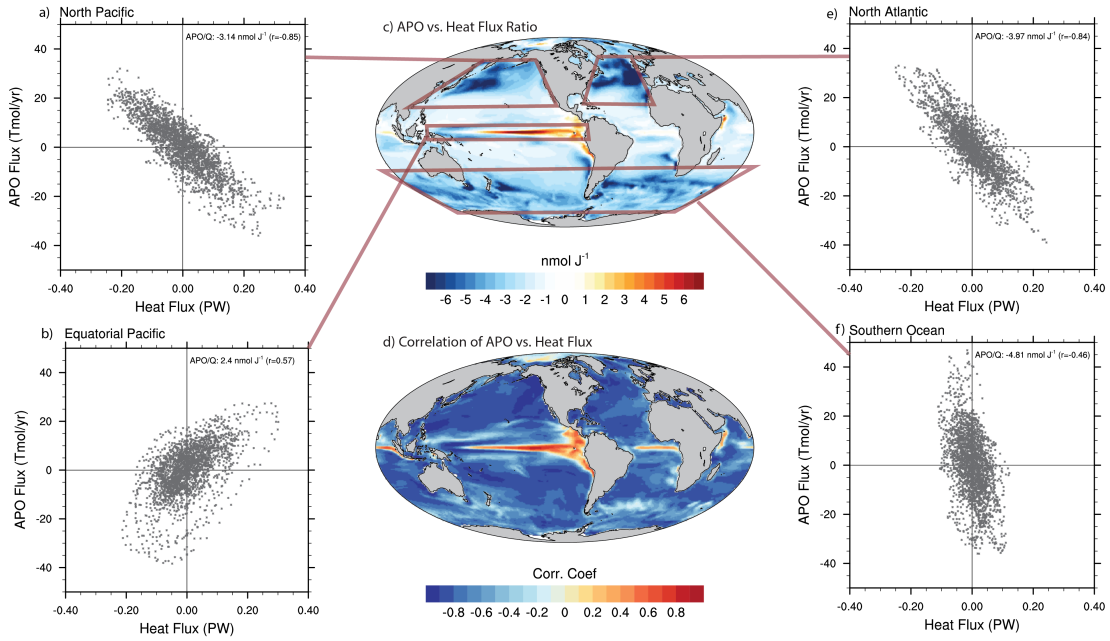

Figure 4.6. Coupling between air-sea APO and heat exchange due to natural variability in the CESM control simulation. Scatter of APO and heat flux anomalies in basins of high variability are shown for a) the north Pacific, b) the equatorial Pacific, e) the north Atlantic, and f) the Southern Ocean. APO-to-heat flux ratio (slope of linear regression) and correlation coefficients are also shown in c) and d) respectively. All series have been smoothed with a 1.5-20 year band-pass filter to highlight interannual-to-decadal variability.

We have already noted that the global relationship between APO and heat due to natural variability is weak on interannual-to-decadal time scales, as shown in Figure 4.3c-d. This coupling is resolved spatially in Figure 4.6 for time-scales between 1.5 and 20 years. The results show that the weak global relationship arises because of distinct, but still strong APO-heat coupling in different regions. Whereas a strongly negative relationship emerges at higher latitude basins (e.g., the North Pacific and North Atlantic), the coupling between heat and APO is strongly positive along the equatorial Pacific (Figure 4.6c-d). The Southern Ocean also shows a negative relationship with a high APO-to-heat exchange ratio, albeit with a weaker correlation than found at northern high latitudes (Figure 4.6c-d).

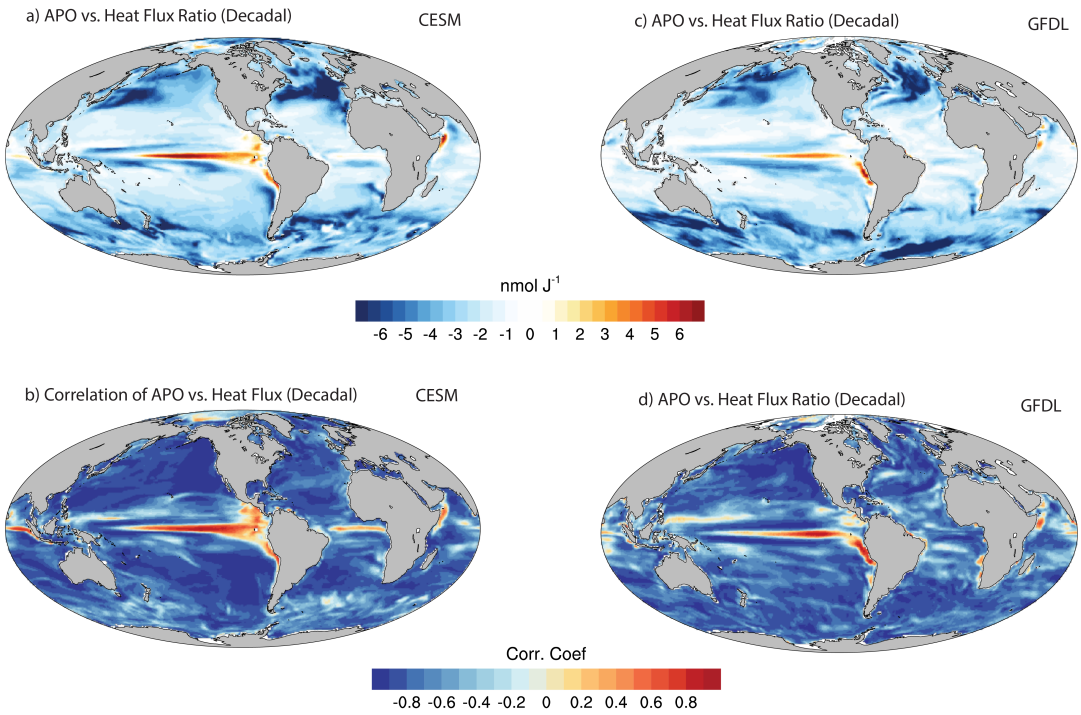

Figure 4.7. Same as Figure 4.6c-d but for decadal timescales (band pass filtered at 7-20 years) in a-b) CESM and c-d) GFDL control simulations.

On decadal timescales, we find a spatially variable response that is similar to the patterns found on interannual timescales (Figure 4.7a-b and Figure 4.6c-d, respectively). These distinct relationships in space are also found in the GFDL control simulation (Figure 4.7c-d), suggesting robust and distinct mechanisms driving heat and APO exchange in these different regions. Clearly, the complex relation between heat and APO that emerges under natural variability complicates the use of APO as a tracer for global OHC change on interannual to decadal timescales.

Still, these distinct relationships may provide useful constraints on the location of ocean heat uptake proposed by different studies. The slowdown in $APO_{Climate}$ increase, for instance, is inconsistent with a dominant role for enhanced ocean heat uptake at higher latitudes, as suggested by Drijfhout et al. (2014). Such a scenario, whereby enhanced ocean heat uptake occurs primarily over the North Atlantic (Chen and Tung, 2014), would induce an acceleration in the upward trend of $APO_{Climate}$ of about 0.56 permeg.yr^{-1} for the CORE2 forced estimate of 0.6 W.m^{-2} over the 2001-2009 period, based on the APO-heat flux ratio averaged over this region (~ -3.97 nmol.J^{-1}). The observed slowdown in $APO_{Climate}$ increase during the hiatus, however, does not preclude a dominant role for enhanced heat uptake over the tropical Pacific (Meehl et al., 2011; 2013; England et al., 2014, Liu et al., 2016), as heat and APO fluxes are modulated in the same direction in this region. Using the positive APO-to-heat flux ratio averaged over this region (+2.40 nmol.J^{-1}) from the CESM control simulation for the CORE2 decadal ocean heat uptake change, assuming 100% uptake

in the equatorial Pacific (5ºN-5ºS), yields a change in $APO_{Climate}$ of about -0.43 permeg.yr^{-1}, a value that is close to the observed slowdown of -0.49 permeg.yr^{-1}. Providing a clear constraint on net ocean heat uptake using $APO_{Climate}$ on interannual-to-decadal timescales, however, remain challenged by the simultaneous contributions of different basins to global heat and APO exchange. We thus evaluate the APO response to changes in ocean heat uptake rates reported by Drijfhout et al. (2014) in the CORE2 forcing product using a hindcast CORE2-forced simulation of the ocean component (POP2) of CESM.

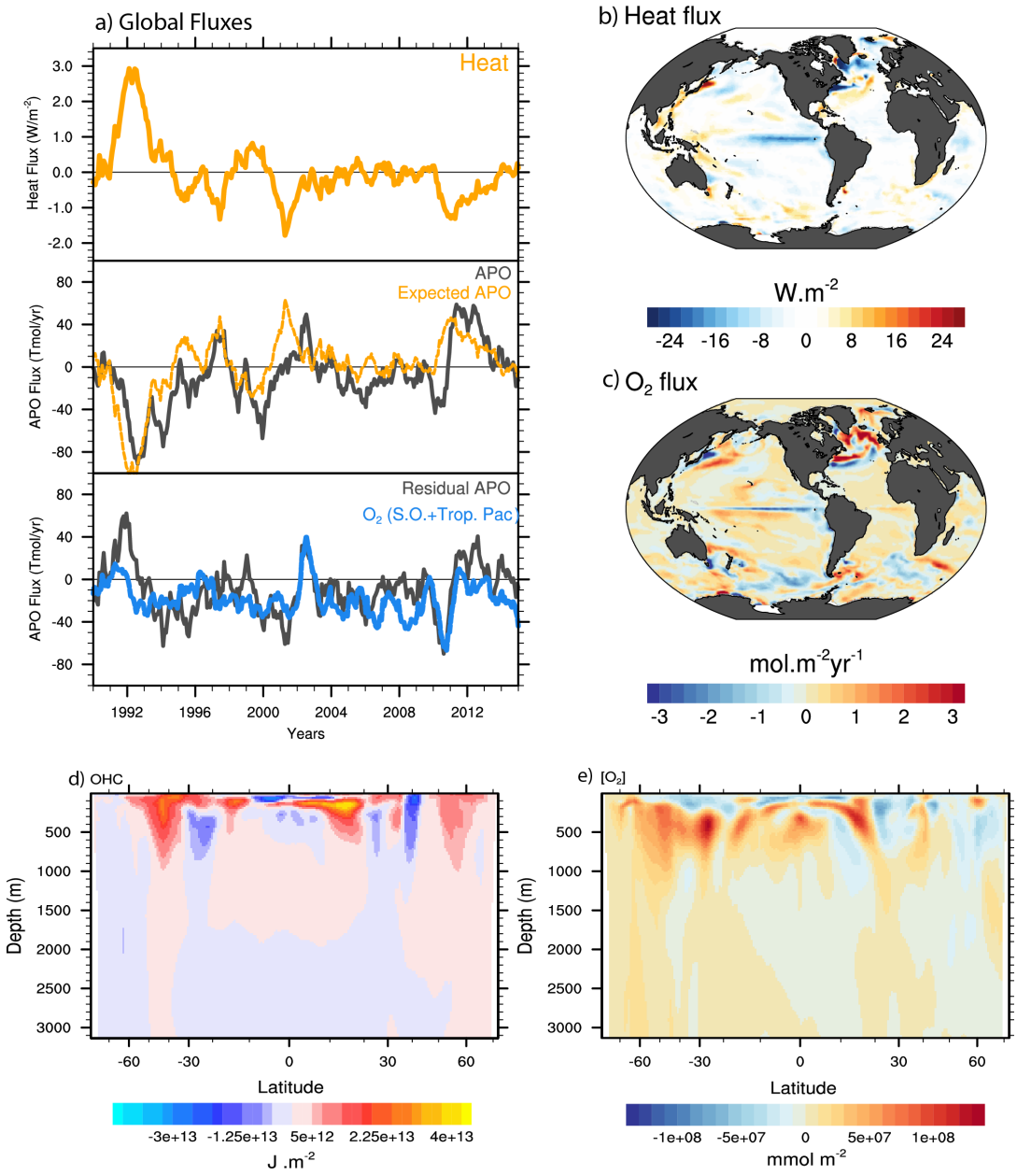

Figure 4.8. Anomalies from a hindcast CESM simulation of a) globally integrated fluxes of heat (orange; top panel), b) APO flux (black) and heat-derived APO flux (orange) calculated using -3.14 nmol.J^{-1} (global APO-to-heat ratio from the control simulation of CESM), c) residual flux (black) calculated as difference between simulated APO flux and the expected APO flux, alongside the O_2 flux integrated over the equatorial Pacific (5ºN-5ºS) and the Southern Ocean (south of 40ºS). Differences in b) heat and c) O_2 flux and zonally integrated d) ocean heat content and e) [O_2] between the hiatus decade (2001-2009) and pre-hiatus decade (1992-2000) are also shown. Anomalies are seasonally detrended and smoothed with a 12-month running mean, with Jan-Dec 1990 as a reference period. No linear detrending has been applied.

c) Hindcast Ocean Simulation of the Hiatus

Figure 4.8a show the heat and APO fluxes simulated in the CORE2-forced hindcast simulation of the ocean component of CESM. In this model run, the ocean is forced by atmospheric conditions that are constrained by observations (see methods section 2.2 in chapter 2), and thus simulate the coupling between heat and APO exchange due to anthropogenic forcing as well as natural variability. Throughout the CORE2-forced ("hindcast") simulation, APO and heat exchanges are negatively related (r=-0.73) due to a combination of volcanic forcing, anthropogenic forcing, and natural variability. We show an "expected" APO, calculated based on the global negative APO-to-heat relation (-3.14 $nmol.J^{-1}$) found in CESM, and find that the simulated APO flux deviates during the hiatus from a tightly negative relation with heat as expected from anthropogenic and volcanic forcing. The residual or deviation from this negative coupling arise mainly from O_2 fluxes over the equatorial Pacific and Southern Ocean (blue line; Figure 4.8c), which show large uptake of O_2 in these regions over the hiatus period.

Figure 4.8b-c shows that simultaneous uptake of O_2 and heat indeed occurs during this period, leading to an increase in the ocean heat content and $[O_2]$ below the mixed layer in these regions during the hiatus (Figure 4.8d-e). Over the tropical Pacific, heat and $[O_2]$ are simultaneously sequestered into the tropical Pacific thermocline and are accompanied by significant cooling and reduced $[O_2]$ in the upper 100 m, suggesting enhanced ventilation during this period, whereby intensified upwelling brings up cold waters that are also depleted in $[O_2]$, driving vigorous uptake

of heat and APO. We also note large changes in the ocean heat content and [O_2] over the Southern Ocean, although these anomalies are not spatially coherent. The hindcast simulation, therefore, suggests that enhanced heat uptake over the tropical Pacific is not inconsistent with the observed slowdown in the $APO_{Climate}$ increase during the hiatus. The deviation of the APO flux from a tight negative relationship with heat during the hiatus is also relevant to studies of ocean deoxygenation (Keeling et al., 2010), which suggest that as ocean warming drives a loss of [O_2]. This anomalous increase in oceanic O_2 uptake during the hiatus in the CESM hindcast simulation in the equatorial Pacific is in agreement with a recent study that suggests a pause in ocean deoxygenation in recent decades due to intensified ventilation of the Pacific thermocline by easterly-induced acceleration of the shallow overturning circulation (Duteil et al., 2014).

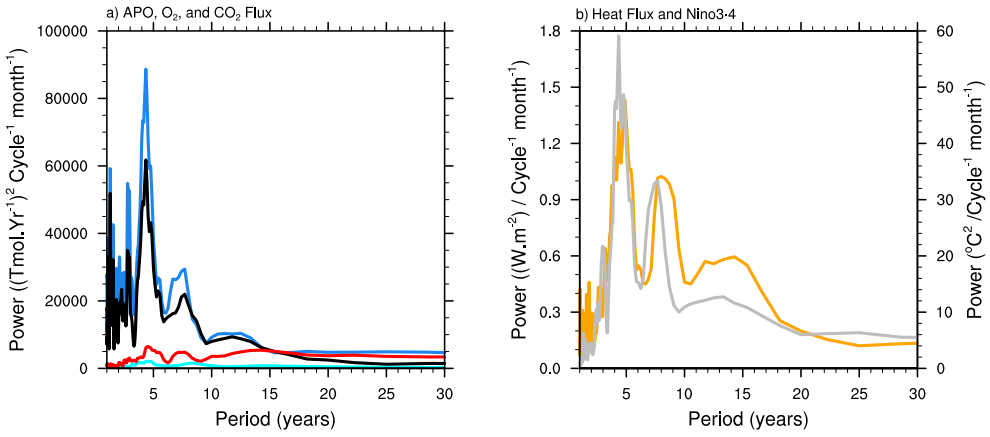

Figure 4.9. Power spectrum of seasonally detrended anomalies in a) APO (black), O_2 (blue), O_{2therm} (cyan), and CO_2 (red) flux, and b) heat flux (orange) and Nino3.4 index (grey) in the CESM control simulation.

d) Mechanisms of Positive Coupling Between Heat and APO

The counterintuitive positive coupling between heat and APO on interannual-to-decadal time scales (Figure 4.6 and 4.7) in the equatorial Pacific is intriguing. Warming of the upper ocean is expected to reduce gas solubility and increase stratification, leading to O_2 outgassing. The unique relationship shown in the equatorial Pacific indicates different processes dominate in this region. We thus evaluate driving mechanisms of this coupling on interannual to decadal timescales over the equatorial Pacific. Global and equatorial APO variability is largely driven by O_2 flux on these timescales, while CO_2 becomes relevant on longer timescales (>15 years Figure 4.9). We thus focus our mechanistic analysis on O_2.

Figure 4.10a-d shows anomalies in SST, heat, O_2, and CO_2 flux, mixed layer depth, and zonal wind during an El Niño event followed by La Niña in a control unforced coupled simulation of the CESM LE. During the El Niño event, surface warming is accompanied by anomalous ocean heat loss, O_2 loss, and small CO_2 uptake. This El Niño event is followed by a La Niña event, which shows cool SST, anomalous heat uptake, O_2 ingassing, and weak CO_2 outgassing. Eddebbar et al. (2017) find that the change in O_2 flux is driven primarily by a reduction in transport of low [O_2] waters to the surface due to deepening of the thermocline and weakening of upwelling during El Niño. This effect dominates the APO response to ENSO, as also shown in Figure 4.10e-f, and leads to lagged (~3 months APO lead) positive coupling between heat and APO anomalies on interannual timescales.

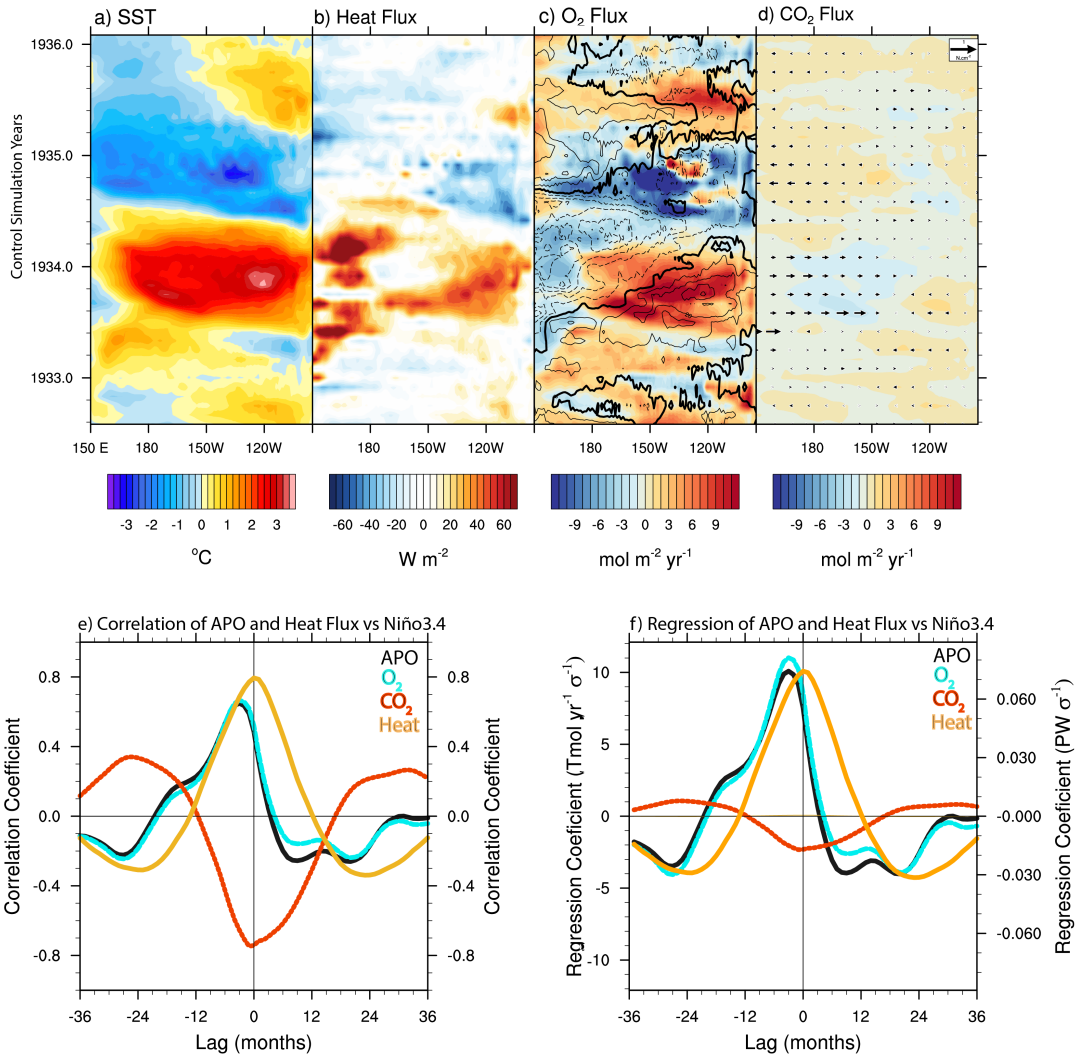

Figure 4.10. Response of air-sea heat, O_2 and CO_2 exchange due to ENSO in the equatorial Pacific (2ºN-2ºS). a) Hovmollar of SST, heat flux, F_{O2} superimposed by mixed layer depths in contours, and F_{CO2} and surface wind stress (dyne/cm^2); e) and f) show lagged correlation and regression of equatorial Pacific F_{APO} (including F_{O2} and F_{CO2} components), and heat flux vs. Niño3.4 index from an unforced control simulation of CESM.

On decadal timescales, the IPO operates essentially in a similar fashion, with intensified upwelling leading to uptake of heat and O_2, while a positive phase is associated with heat and O_2 loss. Figure 4.11 shows that the IPO modulates [O_2] and

heat in the same direction in the upper eastern tropical Pacific Ocean. During a positive phase of the IPO, the deepening of the thermocline in the eastern Pacific leads to upwelling of warmer waters with higher [O_2] content, weakening the climatological intense uptake of O_2 and heat along the equatorial cold tongue. Inversely, a negative phase of the IPO leads to an intensification of O_2 and heat uptake along the equatorial Pacific. This positive coupling between equatorial Pacific heat and O_2 exchange, along with the suggested dominance of the tropical Pacific in driving global flux variability from atmospheric inversions (Rödenbeck et al., 2008) and ocean models (Eddebbar et al., 2017), might help explain the hindcast simulation behavior of APO and observed slowdown in $APO_{Climate}$ during the hiatus, when a negative phase of ENSO and IPO dominate.

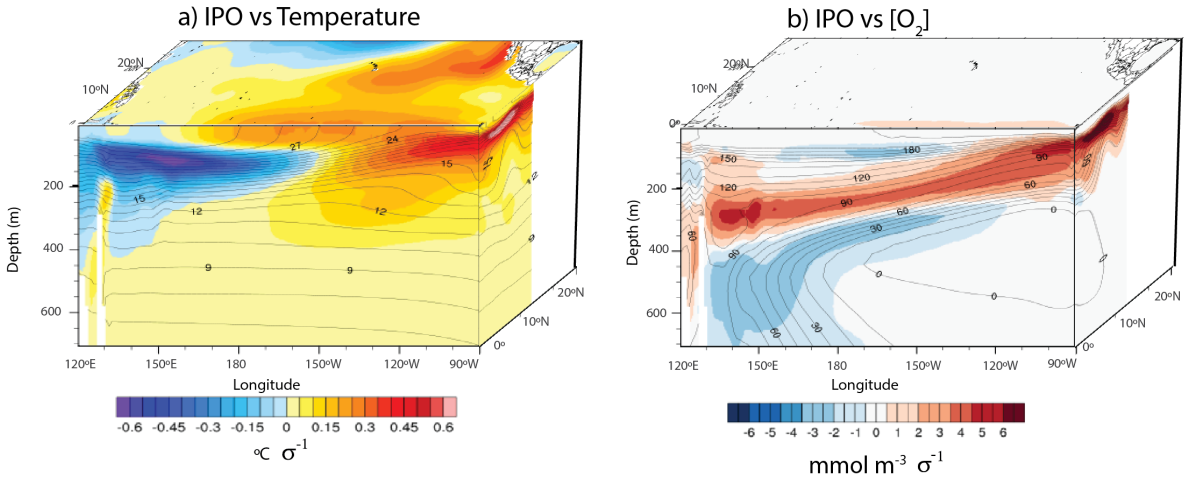

Figure 4.11. Regression of the IPO index vs. anomalies in a) temperature and b) [O_2] over the equatorial Pacific in a 200 year control simulation of CESM. Contours indicate climatological means while color shading show regression coefficients.

Conclusions

In this study, we evaluate decadal trends in atmospheric O_2 and CO_2, using APO as a potential tracer of decadal changes in ocean heat uptake rates. An anomalous decadal downward shift in the long-term $APO_{Climate}$ outgassing trend initially seems to suggest that ocean heat uptake has weakened during the hiatus. However, upon closer examination of the relationship between heat and APO exchange on interannual-to-decadal timescales, we find a distinct coupling that emerges due to natural variability. This coupling is characterized by a positive relationship between heat and APO fluxes in the equatorial Pacific and negative relation at higher latitudes; the APO fluxes on these timescales are dominated by O_2 and the distinct regional relationships lead to a weakening of the global relation between heat and APO.

This regional complexity complicates the interpretation of decadal trends in $APO_{Climate}$ but still provides important constraints on the location of ocean heat uptake. The slowdown in the upward increase in $APO_{Climate}$, for instance, is inconsistent with a dominant role of enhanced heat uptake over the North Atlantic as suggested by Chen and Tung (2014), since this region displays strong negative heat-APO coupling and would thus be associated with intensified APO outgassing. On the other hand, the $APO_{Climate}$ trends do not preclude enhanced ocean heat uptake over the tropical Pacific (Meehl et al. 2011; 2013; England et al., 2014) where natural variability modulates oceanic O_2 and heat fluxes and budgets in the same direction. Additionally, due to regionally distinct APO-heat ratios and their potential cancellation effects in the global mean, large anomalies of APO flux may occur in the absence of major anomalies in

heat flux, and thus $APO_{Climate}$ trends do not rule out a scenario in which no change in the rate of ocean heat uptake have taken place during the hiatus.

Still, these emerging relationships between heat and APO and the observed $APO_{Climate}$ trends suggest that the tropical Pacific may have become more ventilated during the hiatus. This is in general agreement with the findings of Duteil et al. (2014) which suggest that the intensification of the easterlies in recent years may have lead to increased ventilation of the tropical thermocline and a pause in deoxygenation in this region. Mechanisms driving changes in interior $[O_2]$ in the tropical Pacific, however, remain ambiguous in the absence of well-resolved observations and in the presence of large model biases. The $APO_{Climate}$ trends and the counterintuitive relationship described herein motivate the need for improved observations and a closer look at the coupling between climate variability and $[O_2]$ in this region.

Acknowledgements

Chapter 4, in part, is currently being prepared for submission for publication of the material. Eddebbar, Y. A., Keeling R.F., Resplandy, L., Xie, S-P., Rodgers, K., Long, M.C. The dissertation author was the primary investigator and author of this material.

References

Abraham, J. P., M. Baringer, N. L. Bindoff, T. Boyer, L. J. Cheng, J. A. Church, J. L. Conroy, C. M. Domingues, J. T. Fasullo, J. Gilson, and G. Goni, 2013: A review of global ocean temperature observations: Implications for ocean heat content estimates and climate change. Reviews of Geophysics, 51 (3), 450–483.

Ammann, C. M., G. A. Meehl, W. M. Washington, and C. S. Zender, 2003: A monthly and latitudinally varying volcanic forcing dataset in simulations of 20th century climate. Geophysical Research Letters, 30 (12).

Anderson, J. L., V. Balaji, A. J. Broccoli, W. F. Cooke, T. L. Delworth, K. W. Dixon, L. J. Donner, K. A. Dunne, S. M. Freidenreich, and S. T. Garner, 2004: The new gfdl global atmosphere and land model am2–lm2: Evaluation with prescribed sst simulations. Journal of Climate, 17 (24), 4641–4673.

Balmaseda, M. A., K. E. Trenberth, and E. Kallen, 2013: Distinctive climate signals in reanalysis of global ocean heat content. Geophysical Research Letters, 40 (9), 1754–1759.

Boden, T., G. Marland, and B. Andres, 2009: Global co2 emissions from fossil-fuel burning, cement manufacture, and gas flaring: 1751–2006. Carbon Dioxide Information Analysis Center (CDIAC) Laboratory, Oak Ridge National Laboratory, Oak Ridge, Tenn., USA http://cdiac. ornl. gov/ftp/ndp030/global. 1751 2006. ems.

Chen, X., and K.-K. Tung, 2014: Varying planetary heat sink led to global-warming slowdown and acceleration. Science, 345 (6199), 897–903.

Danabasoglu, G., S. C. Bates, B. P. Briegleb, S. R. Jayne, M. Jochum, W. G. Large, S. Peacock, and S. G. Yeager, 2012: The ccsm4 ocean component. Journal of Climate, 25 (5), 1361–1389.

Deser, C., A. Phillips, V. Bourdette, and H. Teng, 2012: Uncertainty in climate change projections: the role of internal variability. Clim. Dyn., 38, 527–546, doi:10.1007/s00382-010-0977-x.

DeVries, T., 2014: The oceanic anthropogenic co2 sink: Storage, air-sea fluxes, and transports over the industrial era. Global Biogeochemical Cycles, 28 (7), 631–647.

Drijfhout, S., A. Blaker, S. Josey, A. Nurser, B. Sinha, and M. Balmaseda, 2014: Surface warming hiatus caused by increased heat uptake across multiple ocean basins. Geophysical Research Letters, 41 (22), 7868–7874.

Dunne, J. P., A. Gnanadesikan, J. L. Sarmiento, and R. D. Slater, 2010: Technical description of the prototype version (v0) of tracers of phytoplankton with allometric zooplankton (topaz) ocean biogeochemical model as used in the princeton ifmip model. Biogeosciences, 7 (Supplement).

Dunne, J. P., J. G. John, A. J. Adcroft, S. M. Griffies, R. W. Hallberg, E. Shevliakova, R. J. Stouffer, W. Cooke, K. A. Dunne, M. J. Harrison, and J. P. Krasting, 2012:

Gfdls esm2 global coupled climate–carbon earth system models. part i: Physical formulation and baseline simulation characteristics. Journal of Climate, 25 (19), 6646– 6665.

Dunne, J. P., J. G. John, E. Shevliakova, R. J. Stouffer, J. P. Krasting, S. L. Malyshev, P. C. Milly, L. T. Sentman, A. J. Adcroft, W. Cooke, and K. A. Dunne, 2013: Gfdls esm2 global coupled climate– carbon earth system models. part ii: carbon system formulation and baseline simulation characteristics. Journal of Climate, 26 (7), 2247– 2267.

Duteil, O., C. W. Böning, and A. Oschlies, 2014: Variability in subtropical-tropical cells drives oxygen levels in the tropical pacific ocean. Geophysical Research Letters, 41 (24), 8926–8934.

Eddebbar, Y. A., M. C. Long, L. Resplandy, C. Rödenbeck, K. B. Rodgers, M. Manizza, and R. F. Keeling, 2017: Impacts of enso on air-sea oxygen exchange: observations and mechanisms. Global Biogeochem. Cycles, doi:10.1002/2017gb005630.

England, M. H., S. McGregor, P. Spence, G. A. Meehl, A. Timmermann, W. Cai, A. S. Gupta, M. J. McPhaden, A. Purich, and A. Santoso, 2014: Recent intensification of wind-driven circulation in the pacific and the ongoing warming hiatus. Nature Climate Change, 4 (3), 222.

Feely, R. A., J. Boutin, C. E. Cosca, Y. Dandonneau, J. Etcheto, H. Y. Inoue, M. Ishii, C. Le Quéré, D. J. Mackey, M. McPhaden, and N. Metzl, 2002: Seasonal and interannual variability of CO_2 in the equatorial pacific. Deep Sea Research Part II: Topical Studies in Oceanography, 49 (13), 2443–2469.

Frölicher, T. L., F. Joos, G.-K. Plattner, M. Steinacher, and S. C. Doney, 2009: Natural variability and anthropogenic trends in oceanic oxygen in a coupled carbon cycleclimate model ensemble. Global Biogeochemical Cycles, 23 (1), n/a–n/a, doi:10.1029/2008GB003316, URL http://dx. doi.org/10.1029/2008GB003316, gB1003.

Frölicher, T. L., F. Joos, and C. C. Raible, 2011: Sensitivity of atmospheric co2 and climate to explosive volcanic eruptions. Biogeosciences, 8 (8), 2317, copyright - Copyright Copernicus GmbH 2011; Last updated - 2011-10-05.

Griffies, S., A. Biastoch, C. Böning, F. Bryan, G. Danabasoglu, E. P. Chassignet, M. H. England, R. Gerdes, H. Haak, R. W. Hallberg, and W. Hazeleger, 2009: Coordinated Ocean-Ice Reference Experiments (COREs), *Ocean Modell.,* 26, 1–46, doi:10.1016/j.ocemod.2008.08.007.

Hunke, E., W. Lipscomb, A. Turner, N. Jeffery, and S. Elliott, 2008: Cice: the los alamos sea ice model, documentation and software, version 4.0. los alamos national laboratory tech. rep. Tech. rep., LA- CC-06-012.

Hurrell, J. W., M. M. Holland, P. R. Gent, S. Ghan, J. E. Kay, P. J. Kushner, J. F. Lamarque, W. G. Large, D. Lawrence, K. Lindsay, and W. H. Lipscomb, 2013: The community earth system model: a framework for collaborative research. Bulletin of the American Meteorological Society, 94 (9), 1339–1360.

Joos, F., M. Bruno, R. Fink, U. Siegenthaler, T. F. Stocker, C. Le Quere, and J. L. Sarmiento, 1996: An efficient and accurate representation of complex oceanic and biospheric models of anthropogenic carbon uptake. Tellus B: Chemical and Physical Meteorology, 48 (3), 394–417.

Kanel, L., T. L. Frölicher, and N. Gruber, 2017: Hiatus-like decades in the absence of equatorial pacific cooling and accelerated global ocean heat uptake. Geophysical Research Letters.

Kay, J. E., C. Deser, A. Phillips, A. Mai, C. Hannay, G. Strand, J. M. Arblaster, S. C. Bates, G. Danabasoglu, J. Edwards, and M. Holland, 2014: The Community Earth System Model (CESM) Large Ensemble Project: A Community Resource for Studying Climate Change in the Presence of Internal Climate Variability. Bull. Amer. Meteor. Soc., doi:10.1175/BAMS-D-13-00255.1.

Keeling, R., and A. Manning, 2014: Studies of recent changes in atmospheric o2 content. Treatise on Geochemistry, 385–404, doi:10.1016/b978-0-08-095975-7.00420-4.

Keeling, R. F., 1988: Development of an interferometric oxygen analyzer for precise measurement of the atmospheric o 2 mole fraction. Ph. D. thesis, Harvard University.

Keeling, R. F., T. Blaine, B. Paplawsky, L. Katz, C. Atwood, and T. Brockwell, 2004: Measurement of changes in atmospheric ar/n2 ratio using a rapid-switching, single-capillary mass spectrometer system. Tellus B, 56 (4), 322–338.

Keeling, R. F., A. Körtzinger, and N. Gruber, 2010: Ocean deoxygenation in a warming world, Annu. Rev. Marin. Sci., 2, 199–229, doi:10.1146/annurev.marine.010908.163855.

Keeling, R. F., R. P. Najjar, M. L. Bender, and P. P. Tans, 1993: What atmospheric oxygen measurements can tell us about the global carbon cycle. Global Biogeochemical Cycles, 7 (1), 37–67.

Keeling, R. F., and J. Severinghaus, 2000: Atmospheric oxygen measurements and the carbon cycle. The carbon cycle, 6, 134.

Kosaka, Y., and S.-P. Xie, 2013: Recent global-warming hiatus tied to equatorial pacific surface cooling. Nature, 501 (7467), 403.

Landschützer, P., N. Gruber, F.A. Haumann, C. Rödenbeck, D.C. Bakker, S. Van Heuven, M. Hoppema, N. Metzl, C. Sweeney, T. Takahashi, and B. Tilbrook, 2015: The reinvigoration of the southern ocean carbon sink. Science, 349 (6253), 1221–1224.

Le Quéré, C., and Coauthors, 2016: Global carbon budget 2016. Earth System Science Data, 8 (2), 605–649.

Levitus, S., J. I. Antonov, T. P. Boyer, O. K. Baranova, H. E. Garcia, H.E., R. A. Locarnini, A. V. Mishonov, J. R. Reagan, D. Seidov, E. S. Yarosh, and M. M. Zweng, 2012: World ocean heat content and thermosteric sea level change (0–2000 m), 1955–2010. Geophysical Research Letters, 39 (10).

Liu, W., S.-P. Xie, and J. Lu, 2016: Tracking ocean heat uptake during the surface warming hiatus. Nature communications, 7, 10 926.

Long, M. C., K. Lindsay, S. Peacock, J. K. Moore, and S. C. Doney, 2013: Twentieth-century oceanic carbon uptake and storage in cesm1 (bgc). Journal of Climate, 26 (18), 6775–6800.

Lovenduski, N. S., N. Gruber, S. C. Doney, and I. D. Lima, 2007: Enhanced co2 outgassing in the southern ocean from a positive phase of the southern annular mode. Global Biogeochemical Cycles, 21 (2).

McKinley, G. A., M. J. Follows, and J. Marshall, 2004: Mechanisms of air-sea co2 flux variability in the equatorial pacific and the north atlantic. Global Biogeochemical Cycles, 18 (2).

McKinley, G. A., M. J. Follows, J. Marshall, and S.-M. Fan, 2003: Interannual variability of air-sea o2 fluxes and the determination of co2 sinks using atmospheric o2/n2. Geophysical Research Letters, 30 (3).

Meehl, G. A., J. M. Arblaster, J. T. Fasullo, A. Hu, and K. E. Trenberth, 2011: Model-based evidence of deep-ocean heat uptake during surface temperature hiatus periods, Nat. Clim. Change, 1(7), 360–364, doi:10.1038/nclimate1229.

Meehl, G. A., A. Hu, J. M. Arblaster, J. Fasullo, and K. E. Trenberth, 2013: Externally forced and internally generated decadal climate variability associated with the interdecadal pacific oscillation. Journal of Climate, 26 (18), 7298–7310.

Moore, J. K., K. Lindsay, S. C. Doney, M. C. Long, and K. Misumi, 2013: Marine ecosystem dynamics and biogeochemical cycling in the community earth system model [cesm1 (bgc)]: Comparison of the 1990s with the 2090s under the rcp4. 5 and rcp8. 5 scenarios. Journal of Climate, 26 (23), 9291–9312.

Morice, C. P., J. J. Kennedy, N. A. Rayner, and P. D. Jones, 2012: Quantifying uncertainties in global and regional temperature change using an ensemble of observational estimates: The HadCRUT4 dataset, J. Geophys. Res., 117, D08101, doi:10.1029/2011JD017187.

Nieves, V., J. K. Willis, and W. C. Patzert, 2015: Recent hiatus caused by decadal shift in indo- pacific heating. Science, 349 (6247), 532–535.

Rafelski, L. E., S. C. Piper, and R. F. Keeling, 2009: Climate effects on atmospheric carbon dioxide over the last century. Tellus B, 61 (5), 718–731.

Resplandy, L., R. Keeling, Y. Eddebbar, M. Brooks, R. Wang, L. Bopp, M. C. Long, J. P. Dunne, W. Koeve, A. Oschlies. Quantification of ocean heat uptake from changes in atmospheric O_2 and CO_2 composition (Submitted to *Nature*).

Resplandy, L., R. Keeling, B. Stephens, J. Bent, A. Jacobson, C. Roedenbeck, and S. Khatiwala, 2016: Constraints on oceanic meridional heat transport from combined measurements of oxygen and carbon. Climate dynamics, 47 (9-10), 3335–3357.

Rödenbeck, C., C. LeQuéré, M. Heimann, and R.F. Keeling, 2008: Interannual variability in oceanic biogeochemical processes inferred by inversion of atmospheric O2/N2 and CO2 data, *Tellus B,* 60, 685–705, doi:10.1111/j.1600-0889.2008.00375.x.

Rodgers, K., J. Lin, and T. Frölicher, 2015: Emergence of multiple ocean ecosystem drivers in a large ensemble suite with an earth system model. Biogeosciences, 12 (11), 3301.

Sabine, C. L., R. A. Feely, N. Gruber, R. M. Key, K. Lee, J. L. Bullister, R. Wanninkhof, C. S. Wong, D. W. Wallace, B. Tilbrook, and F. J. Millero, 2004: The oceanic sink for anthropogenic co2. science, 305 (5682), 367–371.

Severinghaus, J. P., 1995: Studies of the terrestrial o 2 and carbon cycles in sand dune gases and in biosphere 2. Ph. D. thesis, Columbia University.

Stephens, B. B., R. F. Keeling, M. Heimann, K. D. Six, R. Murnane, and K. Caldeira, 1998: Testing global ocean carbon cycle models using measurements of atmospheric o2 and co2 concentration. Global Biogeochem. Cycles, 12 (2), 213–230, doi:10.1029/97gb03500.

Trenberth, K. E., and J. T. Fasullo, 2010: Tracking earth's energy. Science, 328 (5976), 316–317. Trenberth, K. E., and J. T. Fasullo, 2013: An apparent hiatus in global warming? Earth's Future, 1 (1), 19–32.

Trenberth, K. E., J. T. Fasullo, and M. A. Balmaseda, 2014: Earths energy imbalance. Journal of Climate, 27 (9), 3129–3144.

Watanabe, M., Y. Kamae, M. Yoshimori, A. Oka, M. Sato, M. Ishii, T. Mochizuki, and M. Kimoto, 2013: Strengthening of ocean heat uptake efficiency associated with the recent climate hiatus. Geophysical Research Letters, 40 (12), 3175–3179.

Xie, S.-P., Y. Kosaka, and Y. M. Okumura, 2016: Distinct energy budgets for anthropogenic and natural changes during global warming hiatus. Nature Geoscience, 9 (1), 29–33.

Yan, X.-H., T. Boyer, K. Trenberth, T. R. Karl, S.-P. Xie, V. Nieves, K.-K. Tung, and D. Roemmich, 2016: The global warming hiatus: Slowdown or redistribution? Earth's Future, 4 (11), 472– 482.

Zuo, H., M. A. Balmaseda, and K. Mogensen, 2017: The new eddy-permitting ORAP5 ocean reanalysis: Description, evaluation and uncertainties in climate signals. Climate Dynamics, 49(3), pp.791-811.